Volume: 7 : 2024 ISSN: 2220-7643

Ethiopian Journal of Water Science and Technology (EJWST)

Ethiopian Journal of Water Science and Technology (EJWST) Volume: 7 : 2024 ISSN: 2220-7643

Ethiopian Journal of Water Science and Technology (EJWST)

Volume: 7 : 2024 ISSN: 2220-7643

Authors	Pages	Title
Tilaye Worku Bekele, Ephrem Derso Negash , Wegayehu Asfaw, Alemseged Tamiru Haile	01	Remote sensing approach to evaluate the effect of short-term land cover change on flood inundation and impact, Lower Awash Basin, Ethiopia.
Markos Habtewold, Zerihun Achiso	20	Effectiveness of alternative furrow irrigation methods on cabbage yield and water productivity in Angacha District, Central Ethiopia Region
Tesfay Mekonnen Weldegerima	33	Analysis of Precipitation Variability in the Kulfo River Watershed: Insights from Wavelet Analysis and Back-Trajectory Approaches
Aschalew Cherie Workneh, Shumye Hailemariam Yirsaw, Chekole Tamalew Asnik, Sufian Abdulmenan Ousman	54	Assessment and Upgrading of Scour Depth Estimation Equation for Bridge Piers in Kombolcha-Weldia Highway, Ethiopia
Aklilu Alemayehu Kassaye, Mesele Markos Forsidoa	77	Morphodynamic alterations around the bridge opening and the process of scouring under the influence of hydraulic flow parameters on selected bridges in the south Ethiopia regional state, Sodo to Konso highway

Ethiopian Journal of Water Science and Technology (EJWST)

AIM & SCOPE: The Ethiopian Journal of Water Science and Technology (EJWST) is an open-access journal hosted by Arba Minch University, Water Technology Institute. EJWST is a multidisciplinary double-blind peer-reviewed journal that publishes original research papers, critical reviews, and technical notes which are of regional and international significance on all aspects of the water science, technology, policy, regulation, social, economic aspects, management and applications of sustainable use of water resources to cope-up with water scarcity. The journal includes, but is not limited to, the following topics:

Hydrology & integrated water resources management

- Water resources Potential Assessment; Integrated Watershed Management; Optimal Allocation of Water Resources;
- Hydraulic modeling; Eco-hydrology and River Basin Governance and water Institutions

Irrigation and Drainage

- Irrigation Potential Assessment;
- Irrigation Scheme Performance Improvements;
- Agriculture Water Management;
- Conjunctive Use of Surface and Groundwater Irrigation;
- Rain water Harvesting and spate Irrigation.

Water Supply and Sanitation

- Rural and Rural Water Supply and Sanitation;
- Water Quality Modeling;
- Wastewater Treatment and Re-use; Solid Waste Management;
- Ecological Sanitation and Sustainability of Water supply Services.

Renewable Energy

- Assessment of hydropower Potential and development;
- Small scale Hydropower and alternative energy sources;
- Dam and Reservoirs; Wind Energy for Water Pumping and;

Solar Energy for Water pumping

Climate Variability, change, and impacts

- Impacts of climate change on water resources
- Climate Changes Impacts, Vulnerability,
- Adaptation options; Climate Forcing & Dynamics and Predictability of weather and climate extremes.

Emerging Challenges

- Hydro politics and conflict Resolution; Equitable Resources and Benefit-sharing; Gender and Water Resources Management and Cross-cutting Issues

Editorial Board:

The journal editorial board is comprised of multiple disciplines in the areas of Water Resources Engineering, development, and management. The editorial board welcomes all interested authors to join the review and advisory board of EJWST.

Dr. Tadesse Tujuba, Associate Professor, Water Technology Institute, Arba Minch University, Ethiopia.
Dr. Dagnachew Daniel, Associate Professor, Water Technology Institute, Arba Minch University, Ethiopia.
Dr. Yoseph Arba, Assistant Professor, Water Technology Institute, Arba Minch University, Ethiopia.
Dr. Abebe Kebede, Associate Professor, Water Technology Institute, Arba Minch University, Ethiopia.
Dr. Tesfay Mekonnen, Assistant Professor, Water Technology Institute, Arba Minch University, Ethiopia.
Dr. Tamiru Taseme; Associate Professor, Water Technology Institute, Arba Minch University, Ethiopia
Dr. Bisrat Elias, Associate Professor, Water Technology Institute, Arba Minch University, Ethiopia.
Dr. Sirak Tekelab, Associate Professor, Addis Ababa University, Ethiopia.
Dr. Tilahun Derib, Associate Professor, Addis Ababa University, Ethiopia.
Dr. Zeleke Agide, Associate Professor, Addis Ababa University, Ethiopia.
Dr. Kassa Tadele, Director, Ethiopian Engineering Corporation, Ethiopia.
Dr. Yemane Gebremeskel, Assistant Professor, Addis Ababa University, Ethiopia.
Dr. Girma Yimer Ibrahim, Researcher, International water management Institute, Ethiopia.
Dr. Meron Teferi; Researcher, International water management Institute, Ethiopia.
Dr. Abel Tadesse, Director, Ethiopian Engineering Corporation, Ethiopia.
Mr. Ermiyas Alemu, Executive Officer, Ethiopian Engineering Corporation, Ethiopia.
Dr. Abebe Sine, Project Manager, Houston, Texas, USA.
Dr. Abebe Chukula, Senior Lecturer/Researcher, IHE Delft, Netherlands.
Mr. Gezmu Gelu, Lecturer, Water Technology Institute, Arba Minch University, Ethiopia.
Mr. Tegegn Takele, Lecturer, Water Technology Institute, Arba Minch University, Ethiopia.
Dr. Sumit Sane, Indian Institute of Technology Roorkee, Roorkee, Uttarakhand, India
Dr. Seid Ahmed, Associate Professor, Addis Ababa University, Ethiopia.
Dr. Zenebe Mekonnen, Associate Professor, Arba Minch University, Ethiopia.
Dr. Guchie Gulie, , Associate Professor, Wolaita Sodo University, Ethiopia.
Dr. Yechale Kebede, Associate Professor, Arba Minch University, Ethiopia.
Dr. Abdellla Kemal, Associate Professor, Water Technology Institute, Arba Minch University, Ethiopia.
Mr. Berhanu Wogayehu, Lecturer, Water Technology Institute, Arba Minch University, Ethiopia.
Mr. Muluneh Legesse Edamo, Lecturer, Water Technology Institute, Arba Minch University, Ethiopia.
Mr. Aklilu Alemayheu, Lecturer, Water Technology Institute, Arba Minch University, Ethiopia.
Mr. Yohannes Mehari, Lecturer, Water Technology Institute, Arba Minch University, Ethiopia.
Dr. MURALITHARAN JOTHIMANI; Associate Professor, Arba Minch University, Ethiopia
Dr. Kibru Gedam;Asistant Professor, University of Gonder, Ethiopia
Professor, Dr. Mathias Rotach, Profeesor, University of Innsbruck, Asutria
Dr. Geremew Sahilu; Associate Professor; Addis Ababa University, Ethiopia
Dr. Andinet Kebede; Associate Professor, AASTU, Ethiopia
Dr. Moltot Zewdie; Associate Professor, Hawassa University, Ethiopia
Dr. Dr Asaminew Teshome ; Depty Director, Ethiopian Meterologuical Inistitute
Mr. Yehenew Wubu,Lecturer, Arba Minch University, Ethiopia
Mr. Mekuanent Muluneh; Associate Researcher, Charles University, Prague
Mr. Aklilu Alemayheu, Lecturer, Arba Minch Water Technology Institute, Arba Minch University, Ethiopia.
Dr. Fisseha S. Unduche; Mantioba County Chief Flood Forcaster, Canada
Dr. Habtamu Kassa; Director, Mantoba County Flood Forcast, Canada
Dr. Kassawu Bishaw; Wolaita Soddo University, Ethiopia

Ethiopian Journal of Water Science and Technology (EJWST)

DOI: https://doi.org/10.59122/17519t6

Vol. 7 , 2024, pages: 1~19 ISSN(Print): 2220-7643

Remote Sensing Approach for Detection and Attribution of Flood Inundation, Lower Awash Basin, Ethiopia

Tilaye Worku Bekele [b*], Ephrem Derso Negash [b], Wegayehu Asfaw[b,c], Alemseged Tamiru Haile[a]

[a]*International Water Management Institute (IWMI), P.O.Box, 5689, Addis Ababa, Ethiopia.;* [b]*Water Technology Institute, Arba Minch University, P.O. Box 21, Arba Minch, Ethiopia;* [c]*Department of Water Resources, Faculty of Geo-Information Science and Earth Observation (ITC), University of Twente, 7522 NH, Enschede, the Netherlands*.

[*]Corresponding author: Email: tworkcon@gmail.com, P.O. Box: 21, Arba Minch University, Arba Minch, Ethiopia.

Abstract

Flood risk management has been severely constrained by limited information on the causes and impacts of flooding. In this study, we evaluated the effect of short-term land cover change of Logiya Catchment on flood inundation to impact Dubti town and its surroundings in the Lower Awash Basin, Ethiopia. We used Sentinel-1 Synthetic Aperture Radar (S-1 SAR) data to detect flood but Sentinel-2 (S-2) optical satellite data to classify land cover by applying a machine learning algorithm. We also used land cover and soil data to generate the Curve Number (CN) map of the study area from 2017 to 2023. The flood maps showed that roads and irrigation canals were washed away by the 2020 extreme flood, which led to the inundation and abandonment of the Tendaho Irrigation Scheme. The runoff generation potential (CN) was above 27% at the Logiya Catchment from 2017 to 2023, contributing to severe flooding. The remote sensing analysis showed that overflow of the Logiya River in 2020 was intercepted and conveyed by the main irrigation canal of the Tendaho Scheme resulting in inundation of the Dubti and its surroundings. The flood extent at Dubti and its surroundings was 59.22 km^2 in 2020. It increased by 26% from 2017 to 2019. Frequent (6-days), high resolution (10m) and time-series 7 years Sentinel-1 data helped to get a detailed characterization of the cause, dynamics, and impacts of the historical flood events. The approach and results of this study can guide flood risk management in the study area and serve as a reference for future studies in other flood affected areas.

Keywords: Sentine-1 SAR, flood mapping, land cover, attribution, Awash-Basin, Logiya catchment, Dubti town.

Date received: 7 Oct. 2024; Received in the revised form : 22 Feb 2024; Accepted: 30 November . 2024;
Published: December , 2024

1. INTRODUCTION

In Ethiopia, flooding is a major natural hazard that hinders economic development and causes loss of human life (Tamiru & Dinka 2021; Bibi et al. 2023). In 2016, flood damaged households (6249 USD) and farmland (5326 USD) in central rift-valley basin (Edamo et al. 2022). Major cities of the country such as Addis Ababa, Adama, and Dire Dawa are under flood risk. Specifically, 25 % of Adama city is vulnerable to flooding (Leta & Adugna 2023) and 44,544 and 77,320 buildings in Addis Ababa are exposed to floods of 1-in-5 and 1-in-100 years return, respectively (Carr et al. 2024; Asfaw et al. 2025). The flood risk of these cities can be associated with low coping capacity (Erena & Worku 2019) and bio-physical factors. Hence, flood studies are essential to enhance the coping and adaptation capacities of the cities and towns of Ethiopia (Haile et al. 2024).

Stream-flow monitoring in Ethiopia is hampered by the decline of ground-based monitoring stations that often do not cover flood prone areas (Haile et al 2022). As a result, flood risk management is commonly based on limited data and knowledge about past floods. Earth observation satellite can fill such data gap by monitoring during both day and night as well as in all weather conditions (Li et al. 2018). Optical remote sensing satellites incapable monitor floods during cloudy seasons (Munasinghe et al. 2023; Matheswaran et al. 2019). The S-1 SAR provides images at 10 meter horizontal spatial resolution every 12 or 6-day intervals subject to geographic locations (Mohammadi et al. 2020). However, the S-1 data requires pre-processing to minimize the effects of buildings, vegetation (Nuthammachot et al. 2017), and topography (Zeng et al. 2020) on the imagery.

Low signal backscatter intensity of S-1 SAR indicates flooded surface. This can be distinguished from non-flooded surface by histogram thresholding (Cao et al. 2019) and/or change detection (Clement et al. 2017). The accuracy of these methods can be enhanced using ground based reference data (e.g. Bekele et al. 2022). Obtaining such data may not be easy owing to the limitation of existing ground-based measurement equipment. As a result, proxy data is often used to calibrate or validate flood maps while some researchers use secondary data as ground-based reference data. Using the flood data from the S-2 optical imagery as a reference, Kianfar (2019) reported 68% accuracy in the flood map generated using the S-1 SAR data. Using field surveyed

data and flood maps generated by the community as a reference, Haile et al (2023) reported 95% accuracy of the flood map detected from S-1 SAR data.

Flood can be intensified owing to changes in the runoff generation potential (Curve Number) of the upstream catchments. The Curve Number (CN) can serve as a proxy to estimate the surface runoff generating potential based on the land use and soil characteristics of the catchment (Prabhu et al. 2020). Changes in CN can be caused by urbanization (Miller et al. 2014), deforestation, agricultural practices and ecological transformations (Fang et al. 2022). Hence, time series land cover classification enables monitoring of changes in CN across a catchment. Machine learning (ML) algorithms are receiving popular applications for land cover classifications (Dash et al. 2023). However, these algorithms remain confusing while classifying the built-up and sandy areas, and irrigated and shrub land cover classes (Thakkar et al. 2017). However, classification accuracy of shrub and pasture land can be improved using remote sensing indices (e.g. Normalized Difference Vegetation Index, NDVI) to train Machine Learning (ML) algorithm. Manandhar et al (2009) applying a rule (knowledge based logic) to differentiate built-up area from vegetation land increased the land cover accuracy from 70 to 90%. Dash et al (2023) detected the water body using Normalized Difference Water Index (NDWI) and manually digitized the sandy area following the drainage network of the catchment. Thus, sandy area was excluded from training the ML algorithm to reduce the commission error in built-up and overlaid to enhance the overall accuracy of land cover from 67 to 82 %. These studies indicated that post-classification can enhance the accuracy of land cover classification using ML methods.

This study examines the interaction between flood and land cover in the flood-prone area of Lower Awash Basin, Dubti, Ethiopia. It uses the CN difference between 2017 and 2023 to assess the effect of temporal variability of land cover on the flood generation potential of the Logiya Catchment. The study also examines the inter-annual variability of flood extent and impact in the surrounding of Dubti town.

2. Description of the Study Area

Logiya is an upland catchment that drains from the northern upstream parts of the Awash Basin in Ethiopia. Geographically, the catchment is located between 39.5^{o} to 41.0^{o} E and 12.1^{o} to 11.6^{o} N. The Logiya River joins the Awash River just downstream of the Logiya Bridge. The catchment

covers an area of 4687 km^2 and has a high potential to generate significant flooding because of steep terrain slope and sparse vegetation cover while the flood affects the Ethio-Djibouti road between Logiya and Semera town.

The terrain elevation of the catchment varies from a maximum of 3602 m to 376 m a.m.s.l. Moderate slopes (5 to 10 %) cover 24 % of the catchment. The steep and extremely steep slopes (> 15 %) that generate rapid surface runoff cover 14 % of the catchment.

The Logiya Catchment is dominantly covered with farmland, mixed forest, shrub, and bare-land. The eastern upstream part of the catchment is dominantly farmland, while the middle to downstream parts are dominantly bare-land and shrubs. Based on the runoff generation potential, the soil of the catchment is categorized into three hydrological soil groups: A, B, and D. Hydrological soil group D, with high runoff potential covers 76% of the catchment while hydrological soil group A and B cover 5 and 19 %, respectively.

Dubti, situated at the downstream part of Awash Basin, has a population density of 20.6/km^2 [1]. The main irrigation canal of the Tendaho Irrigation Development Project conveys water through the town to irrigate the surrounding agricultural lands. (Figure 1 (d).

The climate of the lower Awash Basin is divided into three seasons: dry season (Bega) from October to February, short rainy season (Belg) from March to June, and wet season (Kiremt) from July to September (Malede et al. 2024; Taye et al. 2018 and Haile et al. 2023).

[1] https://www.citypopulation.de/en/ethiopia/admin/afar/ET020101__dubti/

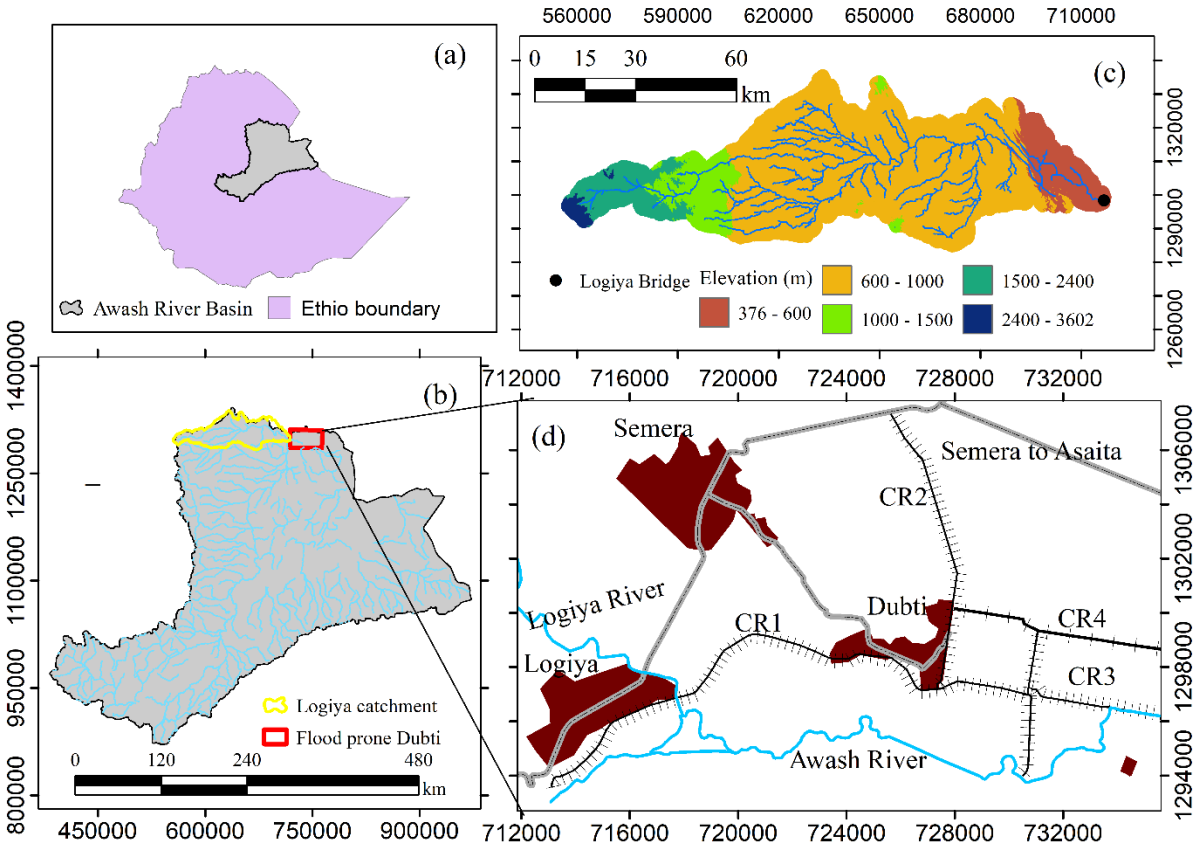

Figure 1. Location map of the study area, (a) location of Awash Basin in the Ethiopia, (b) the Logiya Catchment (yellow polygon) and flood prone area of Dubti (red rectangle), (c) the elevation map of Logiya Catchment and (d) Dubti and other nearby towns. CR represents main canal with access road stretching along the canal and numbers indicate the various canals

3. Materials and Methods

3.1. Materials

The data inputs of this study were Ground Control Points (GCPs) collected from the field and Google Earth images; community consultation (to select the study site of Logiya Catchment and historical flood extent delineation) (Haile et al. 2023); satellite images (S-1 SAR and Sentinel-2); and global datasets (250m resolution soil data and elevation data)[2]. As there was no registered flood parameter data, the researchers consulted with the community to identify the maximum flood extent that occurred in 2020. Thus, the flood extent map generated by the community was used to train and validate the remote sensing index used for flood monitoring.

[2] https://www.isric.org/explore/isric-soil-data-hub

The Digital Elevation Model (DEM) of 30m horizontal spatial resolution from Shuttle Radar Topography Mission (STRM) was used to reduce the shadow effect in flood mapping using S-1 SAR. S-2 was used to detect the land use and land cover.

The land cover map was detected using a Classification and Regression Tree (CART) machine learning algorithm. It performed better than other machine learning algorithms existed in Google Earth Engine (GEE) cloud computing platform for land cover classification in upper Awash Basin (Negash et al. 2023; Bekele et al. 2022). We used a Root of Normalized Image Difference method selected by Haile et al (2023) for flood detection using S-1 SAR images at the Awash Basin from 2017 to 2022. However, in this study, flood map was extended to 2023 so as to identify new flood-affected area and associated impact.

3.2. Methods

Pre-processed S-2 and S-1 satellite imageries were used to generate multi-temporal land cover and flood maps respectively in the GEE platform (Gorelick et al. 2017). The S-2 dataset was filtered using cloud probability pixels and Air Quality band (Q60) to obtain cloud-free images. The Ground Range Detection format of the S-1 SAR, with VH polarization undergoing radiometric and geometric correction, was employed for flood monitoring. However, the speckle noise of S-1 imageries was filtered using a 3x3 median filtering approach widely used for flood monitoring (Kianfar 2019; Anusha & Bharathi 2020) . To reduce the shadow effect, the S-1 SAR images were laid to mask the terrain with a slope above 2%. In this study, the start of the analysis period was 2017 considering the joint availability of S-1 SAR and S2 satellite images.

3.3. Land Cover mapping

GCPs were collected from Google Earth images while field survey was done to train and validate the ML algorithm of land cover mapping. During the field survey (14 to 18 July 2023) at Dubti flood-prone area, six major land cover classes were identified: agricultural land, bare-land, built-up, mixed forest, shrub land, and water body. Thus, 121 GCPs from both homogeneous and mixed land cover classes with land size of at least three-pixel sizes of S-2 (30x30m) image were collected. Then, additional 193 GCPs were collected from Google Earth Satellite image based on knowledge of the study site, and were used to train the ML algorithm. Based on previous research experiences, at least 30 GCPs per each land cover classes should be used to train the ML algorithm during LC

classification. These, ground truth data collected during filed visit in 2023 was used to validate the ML algorithm performance in land cover classification by using confusion matrix.

At Logiya Catchment, 214 GCPs were collected from Google earth images guided by Normalized Difference Water Index (NDWI) to distinguish the water body and Normalized Difference Vegetation Index (NDVI) to identify shrub land from bareland in 2023. Similarly, 153 GCPs were collected to classify the 2017 land cover. Then, the 2017 and 2023 land cover maps were used to examine the land cover change effect in the runoff generation potential of the catchment.

3.4. Accuracy assessment

In this study, the confusion matrix that contained (n x n) row and column size was constructed. In this case, 'n' referred to the number of land cover classes. The matrix showed (number of GCPs collected from different land cover classes during actual field observation) laid under different land cover classes detected from remote sensing. The diagonal element of the matrix indicated the number of correctly classified land cover classes compared with actual field observation. Then, the overall accuracy was determined by the percent of accurately classified land cover (the sum of diagonal elements of the matrix) compared with the total GCPs (Rwanga & Ndambuki 2017).

To determine producer's accuracy, the number of correctly classified reference GCPs of each land cover class was divided by the total number of reference GCPs laid in a particular land cover class. On the other hand, user's accuracy was determined when the number of correctly classified reference GCPs was divided by the total number of classified pixels in that class. The omission and/or commission errors are calculated by subtracting the producer's and user's accuracy from 100%, respectively.

In post land cover classification, the built-up and irrigated land were masked in re-classifying the land cover map of flood prone area. Thus, used to reduce the commission and omission error reported between built-up and sandy area, and shrub land and irrigated (Manandhar et al. 2009). Therefore, the accuracy of land cover map of 2023 Dubti flood prone area before and after post-processing was determined by reference GCP collected from the field.

3.5. Land cover effect on flood generation

The change in runoff generating potential of Logiya Catchment was examined by using the land cover map of 2017 and 2023, and soil data collected from global dataset. The soil data was reclassified with the hydrological soil group of A, B, and D. The reclassified soil data and land cover map were jointly used to estimate the CN, a proxy for runoff generation potential (Prabhu et al. 2020). In this study, the difference in the CN maps of 2017 and 2023 was reclassified into five classes (less than -20, -5 to -20, -5 to 5, 5 to 20, and greater than 20). Negative CN differences represented reduction in runoff generation potential, while differences between -5 and 5 indicated no change in runoff generation. However, pixels with values greater than 5 showed increased potential to generate runoff and contributed to flood generation over the downstream flood-prone sites.

The Root of Normalized Image Difference method was used to extend flood maps from 2017 to 2022, as reported by Haile et al (2023) to 2023. The method performed better in accuracy when validated through flood map generated by participatory mapping involving the community members. Reference is made to Bekele et al (2022) for detail about the RNID flood detection method. This study examined new flood-affected areas and their interaction with local environment, examining floods detected from 2017 to 2019, 2020. Figure 2 showed the workflow diagram of this study.

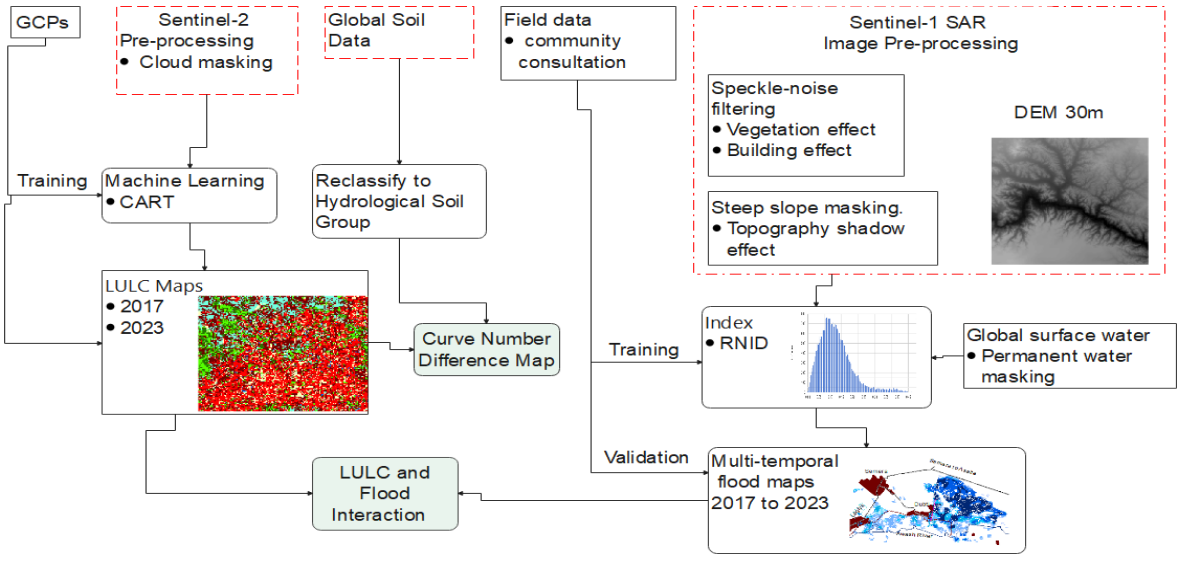

Figure 2. Workflow diagram synthesizing the methods of this study

4. Results and Discussion

4.1. Land Use classification

In this section, the land use maps of Logiya Catchment, Dubti flood-prone area, classification accuracy, CN difference, and flood maps were presented and interpreted. The 2017 and 2023 land cover maps of Logiya Catchment and Dubti flood-prone area were compared.

In 2017, the middle and lower parts of the Logiya Catchment were dominated by bareland and shrub lands, while disconnected agricultural land dominated the upper part of the catchment (Figure 3a). In 2023, agricultural land concentration increased in the western (upstream) part and expanded in small pockets to the other parts of the catchment, reducing shrub and bareland (Figure 3b). Some disconnected agricultural land were connected, while mixed forest areas increased in the western upstream part.

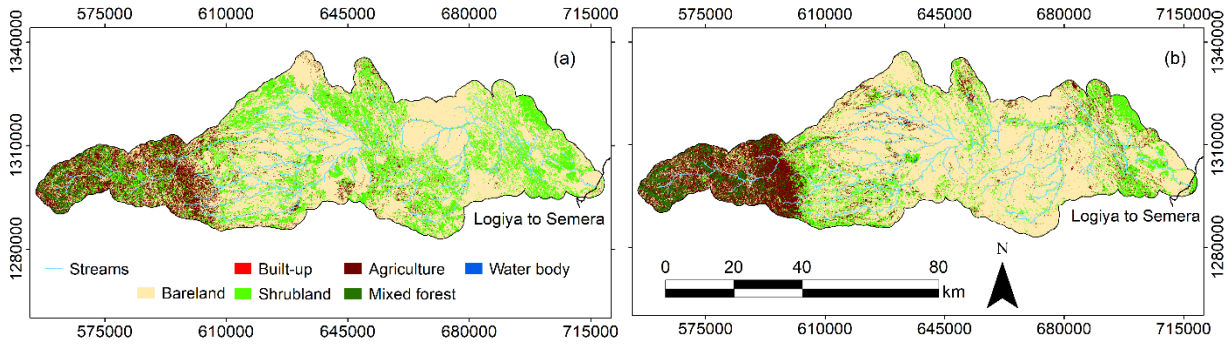

Figure 3. (a) the 2017 LULC map, and (b) the 2023 LULC map of Logiya Catchment

Table 1 showed the percentage of each land cover class of Logiya Catchment in 2017 and 2023. All land cover classes experienced a change within these years. From the perspective of runoff generation, the major changes were expansion of the bareland, farmland and built-up area and reduction of the shrub land. The land cover classes that experienced expansion enhanced runoff generation in the catchment to affect the downstream area. However, the increasing of mixed forest reduced runoff though it increased by more than two-folds in Logiya Catchment.

Table 1. Percentage of each land cover class of Logiya Catchment in 2017 and 2023

	Percentage of area coverage	
Land Cover type	2017	2023
Bare land	59.83	66.32
Built-up	0.02	0.22
Shrubland	27.76	16.36
Farmland	10.89	13.24
Mixed forest	1.47	3.81

4.2. Curve Number Difference and Flood Interaction

Figure 4 showed positive CN differences between 2017 and 2023, slightly surpassing the negative differences suggesting most parts of the catchment experienced increased runoff generation potential. Positive CN differences reported near the catchment outlet had a potential to generate flash floods during intense rainfall conditions. This was in agreement with the opinion of some of the residents in Logiya. They believed that flash floods were common in the area. The positive differences over the upstream part could also be concerning as these areas were characterized by steep slopes that enhanced flood generation potential of the catchment. Most of the middle part of the catchment did not experience a significant change in potential runoff generation between 2017 and 2023.

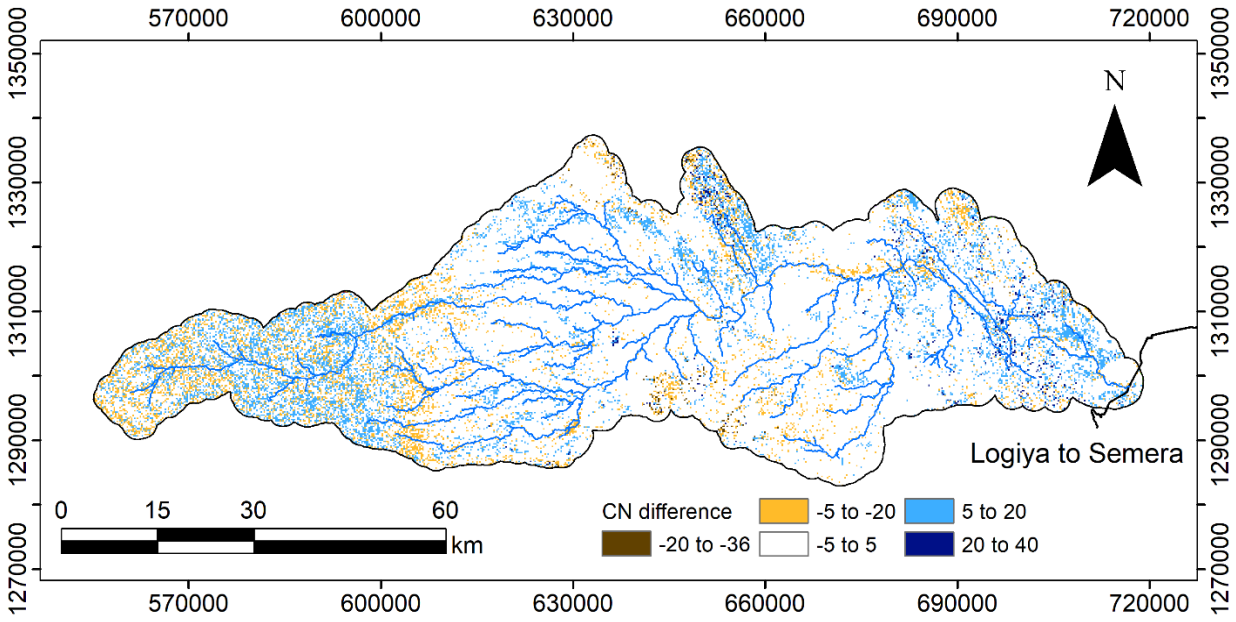

Figure 4. The difference in CN of the Logiya Catchment between 2017 and 2023

Most parts (81.22 %) of the catchment had insignificant CN differences (-5 to 5), from 2017 to 2023 (Table 2). The CN differences were positive only for about 10% of the catchment. However, these positive differences occurred near the catchment outlet and over steep topography that led to increased runoff-generating potential of the Logiya Catchment. This was in agreement with observations of the community in Logiya and Dubti towns.

Table 2. Area coverage of the Logiya Catchment under different categories of CN difference between 2017 and 2023

Curve number difference	Percent of coverage (%)
-20 to -36	0.28
-20 to -5	7.34
-5 to 5	81.22
5 to 20	10.55
20 to 36	0.60

4.3. Flood Interaction with Infrastructure in Dubti

From 2017 to 2019, the flood caused by Logiya River was not hydraulically connected to the flood caused by Awash River, Box 1 Figure (5a). This matches with what the locals told us during the field visit. From 2017 to 2019, the flood did not affect Dubti town which was protected by the road that was constructed parallel to the main irrigation canal (CR1) (Box 2). Boxes 3 and 4 showed areas not affected by flood. The irrigated land and road (solid red dot) were not damaged by floods from 2017 to 2019.

Extreme flood in Awash Basin, particularly in Dubti, was reported in 2020. The flood washed away and damaged the roads and canals constructed for the Tendaho Irrigation Development project figure (5b). The Awash River and the flood-prone areas were connected during the 2020 extreme event, Box 1. The irrigation canal conveyed flood water (Box 1) toward Dubti town but then breached and washed away the roads and canals (CR3 and CR4). This created a new flood-prone area to increase the flood impact toward Box 4.

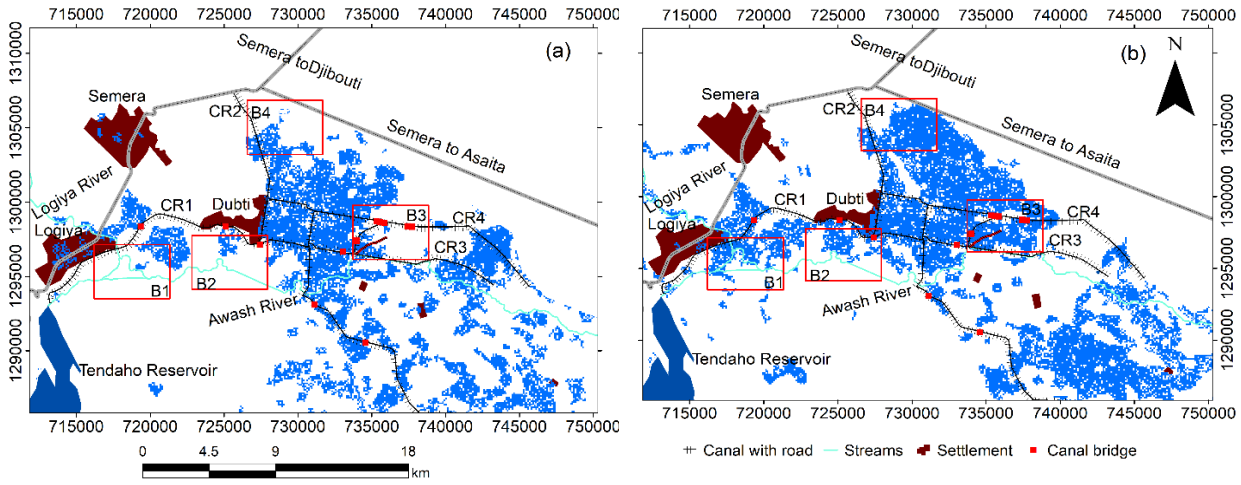

Figure 5. The flood map detected from 2017 to 2019 (a) and 2020 (b), at the flood-prone area of Dubti site and its surrounding sites

4.4. Flood Impact on Land Use and Land Cover Change

Table 3 showed the land cover classification accuracy of flood-prone area before post-processing. The accuracy was 73 % which was smaller than the minimum accuracy requirement, 85% (Rwanga & Ndambuki 2017). The user's and producer's accuracy were also low and varied from 62 to 76 % and 60 to 90%, respectively. The lowest accuracy was obtained for bare land, shrub, and irrigated lands. Some of the irrigated lands were correctly classified as shrub land and bare land which were, however, misclassified as irrigated land.

Table 3. The Confusion Matrix of the 2023 Land Cover Map, before Post-processing

	Reference data					
LC type	Shrubland	Irrigate	Built-up	Bareland	Total	User's accuracy
Shrub	15	5	0	4	24	62.5
Irrigate	5	25	0	5	35	71.4
Built-up	2	1	26	3	32	76.5
Bareland	3	1	3	23	30	71.9
Total	25	32	29	35		
Producer's accuracy	60.0	78.1	89.7	65.7		Overall accuracy 73.6

The overall accuracy of the 2023 land cover map after post processing showed increment of 85.12 % by reducing the omission errors reported in the built-up and shrub lands (Table 4). The user's and producer's accuracy enhanced from 79 to 87.5 % and from 76 to 93.33 % respectively. The

bare land with gravel introduced a commission error in the irrigated and shrub lands, while the sand was detected as a built-up to reduce the user's and producer's accuracy. The overall accuracy reported in this study substantially improved after post-processing and indicated that the land cover map could be used for evaluating the impact of floods and vice versa.

Table 4. The Confusion Matrix of the 2023 Land Cover Map, after Post-processing

	Reference data					
LC type	Shrub land	Irrigate	Built-up	Bare land	Total	Users accuracy
Shrub	19	3	0	2	24	79.2
Irrigate	3	30	0	2	35	85.7
Built-up	1	1	28	2	32	87.5
Bare land	2	0	2	26	30	86.7
Total	25	34	30	32		
Producer's accuracy	76.00	88.24	93.33	81.25		Overall accuracy 85.12

The flood impact was not limited to damaging irrigated canals and roads, but it also affected the irrigated land. Figure 6 (a) and (b) showed the 2017 and 2023 land cover at the flood-prone site of lower Awash Basin, Dubti. The irrigated land of the Tendaho Irrigation Development Project was abandoned and converted to shrub land in the 2023 LC map because of the 2020 flood impact. In 2023, the built-up area in the surroundings of Dubti, Logiya, and Semera towns expanded to alter the local flood characteristics (informal communication with the Dubti town community during field observation).

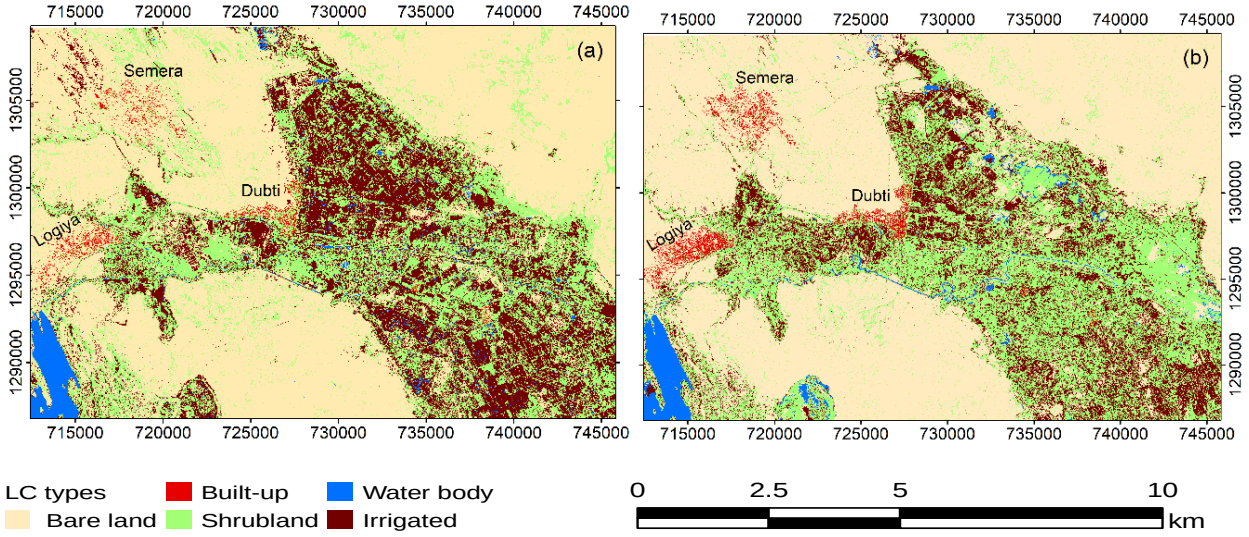

Figure 6. The 2017 and 2023 land cover maps of flood prone area shown in (a) and (b) respectively

The bare land and shrub land dominantly covered the surrounding of Dubti town. The shrub land expanded because of the 2020 flood at the expense of the bareland and irrigated land (Table 5).

Table 5. Land Cover Classes in 2017 and 2023, at Dubti town and its surroundings

	Area coverage percentage	
LULC type detected	2017 (%)	2023 (%)
Bare land	57.25	59.36
Built-up	0.56	0.85
Shrub land	21.49	24.65
Water body	2.08	2.02
Irrigated land	18.62	13.13

4.5. Discussion

The flooding in the lower Awash Basin was often associated with overtopping of the main Awash River with limited focus on the contribution of the tributaries. In this study, remote sensing data helped to study past floods and the contribution of the Logiya River. The remote sensing-based analysis was supported by field survey and community consultation from 2017 to 2023. Edamo et al (2022) emphasized that lack of community participation might limit flood risk management effectiveness.

Flooding was a major natural disaster that often displaced many people, but lack of ground-based data had hidden its historical characteristics and scientific evidence to manage and provide adaptation for future flood risk events. Satellites monitored the land surface at relatively short time interval to detect changes in the feature owing to flooding. The S-1 SAR operated over the land surface at day-night and any weather condition, while the S-2 optical image was suitable to assess the land cover and land use features.

Field observation and consultation with the local community allowed to fill the information gap that couldn't be provided by remote sensing images (e.g. the flood interaction with infrastructure) and identify factor contribution for flooding. However, flood index accuracy could be affected by how threshold values were determined, i.e., either globally or locally to detect flooded pixels. The S-1 SAR polarization affected the accuracy of the flood map (Bekele et al. 2022). Therefore, flood maps generated by VH and VV polarization were compared using ground truth data.

The findings of this study suggested that the positive CN region of Logiya Catchment could be treated by nature based solution e.g. tree planting to reduce the runoff generation potential and flood effects on Dubti. Negash et al (2023) demonstrated that expansion of built-up and agricultural area upstream of a catchment enhanced flood generation potential. The current study showed that enhanced changes in land cover were observed on steep slopes and near the catchment outlet and could have significant effects on flood generation to affect the downstream people and property.

So far, most previous studies focused on how floods impacted various land cover and land use classes (Zope et al., 2016). However, this study indicated that the infrastructure (roads and canals) influenced the spatial pattern of floods and associated impacts. Therefore, the planning, design, and construction of infrastructures should be based on water sensitivity and flood studies. For example, some infrastructures generated false sense of water security regarding flood protection (observed in field observation along the flood-plain of upper and lower Awash Basin). Around Dubti site, the main irrigation canal constructed by Tendaho Irrigation Development project conveyed the Logiya River overflows toward Dubti town and over the irrigated land during the extreme floods in 2020. This agreed with Njogu's (2021) research findings that the infrastructure development over flood-plains affected the flood characteristics. It suggested the need to consider the implications of infrastructures on flooding during the design and construction stages (Taye et al. 2024). Bekele et al (2022) showed that the Addis Ababa to Adama road and flood wall constructed by community intervened with the natural flow direction, contributing to the flooding in Akaki Catchment.

The findings of this study could be enhanced through additional ground control points and the use of rainfall-runoff models. However, modeling applications were constrained by stream-flow data availability. Citizen science provided an opportunity to engage the public in generation of stream-flow data and hydrological knowledge generation. However, there were only limited studies that applied citizen science for flood studies.

5. Conclusions and Recommendations

In this study, the Sentinel-1 SAR and Sentinel-2 optical satellite images were used for historical flood and land cover change monitoring, respectively. The following conclusions were drawn based on the results of this study:-

- The accuracy of land cover classification using CART could be enhanced using remote sensing indices for post-processing.
- The remote sensing approach enabled the examination of the infrastructure impact on flood characteristics. Considering the rapid development of infrastructures in Ethiopia, potential interactions between infrastructures and floods needed to be investigated prior to infrastructure development.
- High temporal revisit (6 days) of S-1 SAR images over the Dubti flood-prone area allowed reasonable representation of the spatial and temporal variability of flood characteristics.
- Community consultation provided actual ground truth data to evaluate historical flood and fill the remote sensing gap. In detecting the flood interaction with infrastructure (road and irrigation canal) constructed at the flood-prone area.
- Multi-causality of extreme flood events was identified in this study but it required further investigation across various flood prone areas.

Acknowledgement

This article was an output from the REACH Programme, funded by UK Aid from the UK Foreign, Commonwealth and Development Office (FCDO) for the benefit of developing countries (Programme Code 201880).

Data availability

Data will be available on request.

References

Alemu, A. N., Haile, A. T., Carr, A. B., Trigg, M. A., Mengistie, G. K., & Walsh, C. L. (2023). Filling data gaps using citizen science for flood modeling in urbanized catchment of akaki. Natural Hazard Research. https://doi.org/10.1016/j.nhres.2023.05.002

Anusha, N., & Bharathi, B. (2020). Flood detection and flood mapping using multi-temporal synthetic aperture radar and optical data. Egyptian Journal of Remote Sensing and Space Science, 23(2), 207–219. https://doi.org/10.1016/j.ejrs.2019.01.001

Asfaw, W., Rientjes, T., Bekele, T. W., & Haile, A. T. (2025). Estimating elements susceptible to urban flooding using multisource data and machine learning. International Journal of Disaster Risk Reduction, 116(December 2024), 105169. https://doi.org/10.1016/j.ijdrr.2024.105169

Bekele, T. W., Haile, A. T., Trigg, M. A., & Walsh, C. L. (2022). Evaluating a new method of remote sensing for flood mapping in the urban and peri-urban areas: Applied to Addis Ababa and the Akaki catchment in Ethiopia. Natural Hazards Research, February. https://doi.org/10.1016/j.nhres.2022.03.001

Bibi, T. S., Kara, K. G., Bedada, H. J., & Bededa, R. D. (2023). Application of PCSWMM for assessing the impacts of urbanization and climate changes on the efficiency of stormwater drainage systems in managing urban flooding in Robe town, Ethiopia. Journal of Hydrology: Regional Studies, 45(September 2022), 101291. https://doi.org/10.1016/j.ejrh.2022.101291

Cao, H., Zhang, H., Wang, C., & Zhang, B. (2019). Operational flood detection using Sentinel-1 SAR data over large areas. Water (Switzerland), 11(4). https://doi.org/10.3390/w11040786

Carr, A. B., Trigg, M. A., Haile, A. T., Bernhofen, M. V., Alemu, A. N., Bekele, T. W., & Walsh, C. L. (2024). Using global datasets to estimate flood exposure at the city scale: an evaluation in Addis Ababa. Frontiers in Environmental Science, 12(February), 1–14. https://doi.org/10.3389/fenvs.2024.1330295

Clement, M., Kilsby, C., & Moore, P. (2017). Multi-Temporal SAR Flood Mapping using Change Detection Multi-temporal synthetic aperture radar fl ood mapping using change detection. April. https://doi.org/10.1111/jfr3.12303

Dash, P., Sanders, S. L., Parajuli, P., & Ouyang, Y. (2023). Improving the Accuracy of Land Use and Land Cover Classification of Landsat Data in an Agricultural Watershed. Remote Sensing, 15(16), 1–24. https://doi.org/10.3390/rs15164020

Edamo, M. L., Ukumo, T. Y., Lohani, T. K., Ayana, M. T., Ayele, M. A., Mada, Z. M., & Abdi, D. M. (2022). A comparative assessment of multi-criteria decision-making analysis and machine learning methods for flood susceptibility mapping and socio-economic impacts on flood risk in Abela-Abaya floodplain of Ethiopia. Environmental Challenges, 9(July). https://doi.org/10.1016/j.envc.2022.100629

Erena, S. H., & Worku, H. (2019). Urban flood vulnerability assessments: the case of Dire Dawa city, Ethiopia. Natural Hazards, 97(2), 495–516. https://doi.org/10.1007/s11069-019-03654-9

Fang, R., Hon, J., Zhou, M., & Lu, Y. (2022). An Empirical Energy Landscape Reveals

Mechanism of Proteasome in Polypeptide Translocation. ELife, 11, 1–28. https://doi.org/10.7554/eLife.71911

Gorelick, N., Hancher, M., Dixon, M., Ilyushchenko, S., Thau, D., & Moore, R. (2017). Google Earth Engine: Planetary-scale geospatial analysis for everyone. Remote Sensing of Environment, 202, 18–27. https://doi.org/10.1016/j.rse.2017.06.031

Haile, A. T., Asfaw, W., Rientjes, T., & Worako, A. W. (2022). Deterioration of streamflow monitoring in Omo-Gibe basin in Ethiopia. Hydrological Sciences Journal, 67(7), 1040–1053. https://doi.org/10.1080/02626667.2022.2060110

Haile, A. T., Bekele, T. W., Derso, E., Mekuria, W., & Ruckstuhl, S. (2024). Urgent flood hazard assessment using multi-sensor data in refugee hosting community settings : Implications for immediate planning and design of anticipatory actions. Colombo, Sri Lanka: International Water Management Institute (IWMI). CGIAR Initiative on Fragility, Conflict, and Migration. 10p.

Haile, A. T., Bekele, T. W., & Rientjes, T. (2023). Interannual comparison of historical floods through flood detection using multi-temporal Sentinel-1 SAR images, Awash River Basin, Ethiopia. International Journal of Applied Earth Observation and Geoinformation, 124(June), 103505. https://doi.org/10.1016/j.jag.2023.103505

Kianfar, N. (2019). The applicability of dual polarized sentinel-1 sar data for detection of flooded areas in pol-e dokhtar , lorestan , iran. Xlii(october), 12–14. https://doi.org/10.5194/isprs-archives-XLII-4-W18-655-2019

Leta, B. M., & Adugna, D. (2023). Characterizing the level of urban Flood vulnerability using the social-ecological-technological systems framework, the case of Adama city, Ethiopia. Heliyon, 9(10), e20723. https://doi.org/10.1016/j.heliyon.2023.e20723

Li, Y., Martinis, S., Plank, S., & Ludwig, R. (2018). An automatic change detection approach for rapid fl ood mapping in Sentinel-1 SAR data. Int J Appl Earth Obs Geoinformation. 73(March), 123–135. https://doi.org/10.1016/j.jag.2018.05.023

Malede, D. A., Andualem, T. G., Yibeltal, M., Alamirew, T., kassie, A. E., Demeke, G. G., & Mekonnen, Y. G. (2024). Climate change impacts on hydroclimatic variables over Awash basin, Ethiopia: a systematic review. Discover Applied Sciences, 6(1). https://doi.org/10.1007/s42452-024-05640-8

Manandhar, R., Odehi, I. O. A., & Ancevt, T. (2009). Improving the accuracy of land use and land cover classification of landsat data using post-classification enhancement. Remote Sensing, 1(3), 330–344. https://doi.org/10.3390/rs1030330

Matheswaran, K., Alahacoon, N., Pandey, R., & Amarnath, G. (2019). Flood risk assessment in South Asia to prioritize flood index insurance applications in Bihar, India. Geomatics, Natural Hazards and Risk, 10(1), 26–48. https://doi.org/10.1080/19475705.2018.1500495

Miller, J. D., Kim, H., Kjeldsen, T. R., Packman, J., Grebby, S., & Dearden, R. (2014). Assessing the impact of urbanization on storm runoff in a peri-urban catchment using historical change in impervious cover. Journal of Hydrology, 515, 59–70. https://doi.org/10.1016/j.jhydrol.2014.04.011

Mohammadi, A., Khalil Valizadeh Kamran, Sadra Karimzadeh, Shahabi, H., & Nadhir Al-Ansari 6. (2020). Complexity - 2020 - Mohammadi - Flood Detection and Susceptibility Mapping Using Sentinel-1 Time Series Alternating. https://doi.org/10.1155/2020/4271376

Munasinghe, D., Frasson, R. P. de M., David, C. H., Bonnema, M., Schumann, G., & Brakenridge, G. R. (2023). A multi-sensor approach for increased measurements of floods and their societal impacts from space. Communications Earth and Environment, 4(1), 1–10. https://doi.org/10.1038/s43247-023-01129-1

Negash, E. D., Asfaw, W., Walsh, C. L., Mengistie, G. K., & Haile, A. T. (2023). Effects of land use land cover change on streamflow of Akaki. Sustainable Water Resources Management, 4. https://doi.org/10.1007/s40899-023-00831-4

Njogu, H. W. (2021). Effects of floods on infrastructure users in Kenya. Journal of Flood Risk Management, 14(4), 1–10. https://doi.org/10.1111/jfr3.12746

Nuthammachot, N., Phairuang, W., & Stratoulias, D. (2017). Removing speckle noise in Sentinel-1A radar satellite imagery using filtering techniques. February, 0–14. https://www.researchgate.net/publication/313845253

Prabhu, N., Mohan Kumar, T. M., & Inayathulla, M. (2020). Runoff estimation for Arkavathi valley, hebbala valley, KC Valley, South Pennar valley, Vrishabhavathi valley by using soil conservation services curve number method (Scs-cn). Water and Energy International, 63r(2), 57–66. https://www.researchgate.net/publication/341941141

Rwanga, S. S., & Ndambuki, J. M. (2017). Accuracy Assessment of Land Use/Land Cover Classification Using Remote Sensing and GIS. International Journal of Geosciences, 08(04), 611–622. https://doi.org/10.4236/ijg.2017.84033

Tamiru, H., & Dinka, M. O. (2021). Application of ANN and HEC-RAS model for flood inundation mapping in lower Baro Akobo River Basin, Ethiopia. Journal of Hydrology: Regional Studies, 36, 100855. https://doi.org/10.1016/j.ejrh.2021.100855

Taye, M. T., Dyer, E., Hirpa, F. A., & Charles, K. (2018). Climate change impact on water resources in the Awash basin, Ethiopia. Water (Switzerland), 10(11), 1–16. https://doi.org/10.3390/w10111560

Taye, M. T., Nicol, A., & Dyer, E. (2024). Policy and practice recommendations on flood risk management in the Awash basin. REACH Discussion brief.

Thakkar, A. K., Desai, V. R., Patel, A., & Potdar, M. B. (2017). Post-classification corrections in improving the classification of Land Use/Land Cover of arid region using RS and GIS: The case of Arjuni watershed, Gujarat, India. Egyptian Journal of Remote Sensing and Space Science, 20(1), 79–89. https://doi.org/10.1016/j.ejrs.2016.11.006

Zeng, Z., Gan, Y., Kettner, A. J., Yang, Q., Zeng, C., Brakenridge, G. R., & Hong, Y. (2020). Towards high resolution flood monitoring: An integrated methodology using passive microwave brightness temperatures and Sentinel synthetic aperture radar imagery. Journal of Hydrology, 582, 124377. https://doi.org/10.1016/j.jhydrol.2019.124377

Ethiopian Journal of Water Science and Technology (EJWST)

DOI: https://doi.org/10.59122/18519t6

Vol. 7 , 2024, pages: 20~32 ISSN(Print): 2220-7643

Effectiveness of alternative furrow irrigation methods on cabbage yield and water productivity in Angacha District, Central Ethiopia Region

Markos Habtewold* and Zerihun Achiso.

Southern Agricultural Research Institute, Areka Agricultural Research Center
Natural Resource Management Directorate, Small Scale Irrigation Water Management Research Program
Corresponding Author Email: -markokam@yahoo.com, Tel: -+251931318341, P.O.Box-79 Areka, Ethiopia

Abstract

This study aimed at investigating the effectiveness of alternative furrow irrigation methods on the head yield of cabbage and water productivity at Guder Irrigation Scheme in Angacha district Kembata Zone Centeral Ethiopia Region. Three levels of treatment were replicated five times, in Randomized Complete Block Design (RCBD). Farmers were used as replication from farmers' research extension groups. The maximum head yield (52.8t/ha) was obtained from conventional furrow, following the second maximum head yield (49.07t/ha) at alternate furrow irrigation method. The minimum yield (38.112t/ha) was obtained from farmers' practice of irrigation method. Their yield advantages (26.8%) and (22.3%) were recorded from conventional furrow, and alternate furrow irrigation, respectively. The highest water productivity (22.23kg/m^3) was obtained from alternate furrow irrigation, following the second maximum water productivity form conventional furrow irrigation (11.96kg/m^3) and minimum water productivity (8.15kg/m^3). Farmers obtained a net income of (1,278,300 ETB/ha), (1,190,730 ETB/ha) and (909,903.3ETB/ha) from conventional furrow, alternate furrow, and farmers' practices, respectively. Highest benefit cost ratio (18.63) was recorded form alternative furrow irrigation method :(17.83) from every furrow and (14.15) from farmers' practice. This implies that alternative furrow irrigation saves half of irrigation water when assimilated with conventional furrow and doubles net income on the farm gate. Therefore alternative furrow irrigation method should be recommended as a best agricultural water management technology without limiting fresh head yield of cabbage, and water productivity. The technology should be scaled up in to other irrigation schemes with the same agro ecology.

Keywords: - Alternate Furrow Irrigation, Head Cabbage, Yield, Water Productivity, Farmer Practice, Fertilizer, Guder

Date received: 24 Jan. 2024; Received in the revised form : 28 March 2024; Accepted: 01 October . 2024; Published: December, 2024

1. INTRODUCTION

The two most important critical factors affecting cabbage yield are water and fertilizer (Wang *et al*. 2014; Sui *et.al*. 2015; Mon *et.al*. 2016). Agricultural practice is traditionally dominated by small-scale farmers for centuries and its performance has long been adversely affected by shortage of rain and water that left many to sustain their lives on famine relief support (Abebe *et.al*, 2011). Of the total production, rain-fed agriculture accounts for about 97% of Ethiopia's food crops yield whereas irrigated agriculture explains the rest 3% (FAO, 2015). Ethiopia has an irrigation potential of 5.3 million ha (Mha) of which 3.7 Mha can be developed using surface water sources, whereas 1.6 Mha using groundwater and rainwater management (Shitu and Hymiro, 2022). The existing irrigation development in Ethiopia is not significant when compared to the potential of resources that the country has. In this case, the irrigation sub-sector is not contributing its fair share to the GDP. Wet soil conditions caused by over irrigation can damage crops, reduce yields, and contribute to ground water contamination. But adopting proper irrigation water management strategies can limit negative impacts of over irrigation (Nebraska, 2008).

Improving crop water productivity mainly depends upon choosing and adapting water-efficient crops, reducing unproductive water losses, and ensuring ideal agronomic conditions for crop production (Kijne *et.al*., 2003; Bouman, 2007). An important principle for crop water productivity is that water management should go hand in hand with nutrient management, soil management, and pest management (Bindraban *et.al.*, 1999). Conventional furrow irrigation method has a gap of water loss as compared to alternate furrow and fixed furrow irrigation methods. Conventional irrigation is 50 to 60% water efficient. That is to say, 50 to 40% of water released in a flood irrigation system is lost either by runoff or rapid soil infiltration. Efficiency of conventional furrow irrigation can be improved by converting it to alternate furrow irrigation (Jemal and Mukerem, 2017). Irrigation interval and number of irrigation frequency was not identified in the Guger irrigation scheme. As the need assessment result indicated there was a shortage of irrigation and high demand water in the scheme. Therefore, this study was conducted to evaluate and demonstrate alternative furrow irrigation method, refine the practices, and synthesize the lessons that increases water use efficiency.

2. MATERIALS AND METHODS

2.1 Description of study area

The study was conducted at Guder Irrigation Scheme in Adancho Ebala Kebele, Angacha District Kembata Tembaro Zone Southern Ethiopia. The scheme was constructed by Participatory Small Scale Irrigation Development Program (PASIDP-II), which covers 170.1 ha command area with a total beneficiaries of 300 HH. The study site was geographically located at latitude of 07.435°N, longitude of 037.908°E with elevation of 1903 m. a. m. s. l. The vegetable crop head cabbage was selected for the demonstration according to farmers' preference and possible suitability and practices. It was potentially cultivated in the area and used as the main income source for Angacha district.

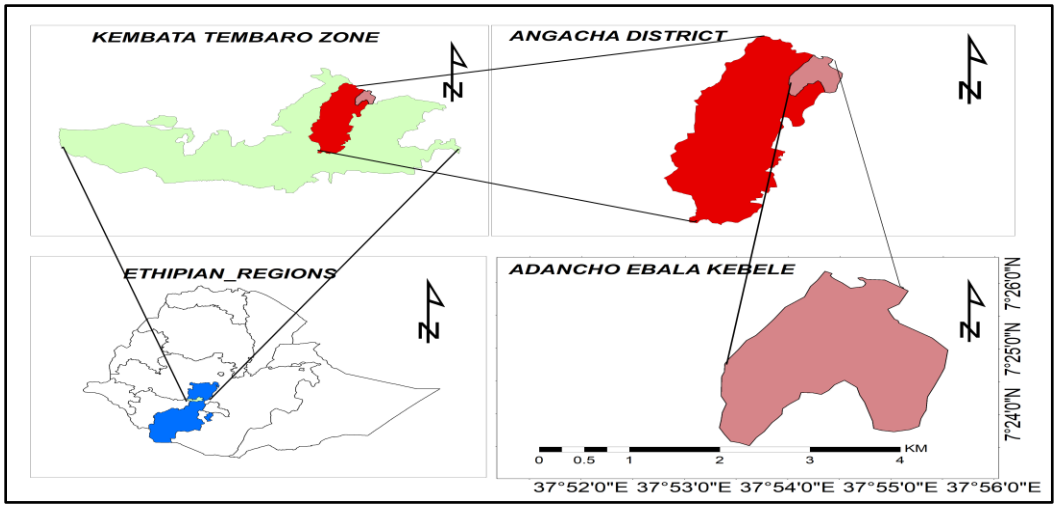

Figure 1. Location map of study area

2.2 Experimental design

The experiment was laid out in randomized complete block design with five replications across farmers. The treatments were conventional furrow irrigation (CFI), alternate furrow irrigation (AFI) and farmer practice (FP) with recommended fertilizer. In conventional furrow and farmer practice irrigation methods, all furrows obtain irrigation water at the same time on their assigned schedules. But in alternate furrow irrigation, odd furrows (1, 3, 5…) received water at first irrigation event and even furrows (2, 4, 6…..) at the next irrigation throughout the growing season with determined irrigation interval. Farmer practice was similar to conventional furrow irrigation method but furrows were made by farmer, not end closed. Furrow dimensions like furrow width, depth and ridge height were not properly constructed and was irrigated with

community irrigation interval not crop water requirement based. The plot size was 10m*10m. The space between plants was 40cm while the rows were spaced 60cm apart. There were 25 plants in a single row and total of 400 plants per 100 square meters plot and 40,000 plants per hectare. The study used head cabbage Copenhagen market variety, ERO brand. The recommended fertilizer rate used was NPS (250 kg/ha) and Urea (330 kg/ha) with seed rate of 0.4kg/ha. Urea was applied in two splits at 30 days after transplanting and head initiation was applied for head cabbage production.

2.3 Data collection and analysis

Climate data, soil, water data, and crop data like scattered canopy, head length, head diameter, head weight and head weight were collected from secondary sources and fields. Some of the data collected were analyzed using an analysis of variance (ANOVA) to determine differences between treatments. Statistix 10.0 was used to run ANOVA and find out differences among the mean values and least significance differences (LSD) at 5% level of significance.

2.4 Climate data

The climatic data were collected from the nearby meteorological station situated at Angacha District. The mean annual rainfall of the area was 1,656 mm with a bimodal pattern that extended from February to September. The mean annual maximum temperature was 24 °C and monthly values ranged between 23°C and 24°C. The mean annual minimum temperature was 14 ^{0}C and monthly values ranged between 13°C and 14°C (Ayalew and Beyene, 2011).

2.5 Soil data

The textural class of the soil type was clay loam. That is to say, the soil has tiny particles with excellent water retention and high fertility as indicated in table 1 below. The maximum water holding capacity of the soil with one meter depth was (36.7%) which was below the threshold values of (40%) for clay soil (Datta *et.al.* 2017). The bulk density that restricts the root growth was (1.45g/cm^3) which was below the maximum limit of the value 1.58g/cm^3 for clay loam soil. 3.62% organic matter was obtained by multiplying organic carbon values with 1.724, conversion factor($OM\% = 1.724 * OC\%$). The pH value of the soil was 6.9 which was within the range of 5.5 - 7.5. This may not hinder the growth of most vegetables (Penas and Lindgen, 1990). The soil salinity was 1.24 d*S*/m which was below the salinity threshold values ≤2.5dS/m (Snapp *et.al*., 1991) for the majority of vegetable crops.

Table 1: Physical and chemical property of the soil

Soil particle distribution				Bd (g/cm^3)	FC (%)	PWP (%)	SM (%)	OC (%)	pH	ECe (dS/m)
Sand	Silt	Clay	Textural class							
31	31	38	Clay Loam	1.45	36.7	23.3	19.86	2.10	6.9	1.24

where: - Bd-Bulk density, FC-Field capacity, PWP-Permanent wilting point, SM- Soil moisture, OC-Organic carbon, pH-Soil acidity, ECe-Electric conductivity of soil.

2.6 Crop water determination

Crop water requirement refers to the amount of water that needs to be supplied while crop evapotranspiration refers to the amount of water that is lost through evapotranspiration (Allen *et.al*., 1998). The crop coefficient values varied at different stages: at initial stage 0.45 (28days), development stage 0.75(35days), mid stage 1.03(25days) and late stage 0.95(15days) with maximum allowable depletion (MAD) of 35% (Doorenbos and Kassam, 1986).The crop was transplanted in March 17/2021 and harvested in June 28/2021 within a total growing period of 103 days. CROPWAT 8.0 software was used to generate the climate data to determine irrigation schedule and seasonal crop water requirement. .

$$ETc = ETo \times Kc \quad (1)$$

Where-ETc stands for crop evapotranspiration; Kc -crop coefficient; and ETo -reference evapotranspiration.

Seasonal amount of crop water requirement for head cabbage (SCWR) determined by CWR 8.0 was 441.14 mm/ month.

Table 2: Seasonal crop water requirement for head cabbage

Months	Dev.t Stages	No. of days	Kc-Values	ETo (mm/day)	ETc (mm/day)	ETc (mm/Period)	ETc (mm/Month)
March	Initial	14	0.45	5.2	2.34	32.76	32.76
April		16	0.45	4.5	2.03	32.4	
April	Dev.t	14	0.75	4.5	3.38	47.25	79.65
May		31	0.75	4.4	3.3	102.3	102.3
June	Mid	30	1.03	4.3	4.43	132.87	
July		10	1.03	3.3	3.399	33.99	166.86
July	Late	19	0.95	3.3	3.135	59.57	59.57
Seasonal ETc(mm)							**441.14**

Irrigation water management: The total available water (TAW), stored in a unit volume of soil, was determined by the expression:

$$\mathrm{TAW} = \frac{(\mathrm{FC} - \mathrm{PWP}) * \mathrm{Bd} * \mathrm{Dz}}{100} \quad (2)$$

The irrigation schedule should be fixed based on the readily available soil water (RAW) for maximum crop production and was computed by the expression:

$$\mathrm{RAW} = (\mathrm{TAW} * \mathrm{p}) \quad (3)$$

Where RAW was in mm, and P (35%) was permissible soil moisture depletion

The depth of irrigation supplied at any time could be obtained by the equation: -

$$\mathrm{Inet(mm)} = (\mathrm{ETc_{mm}} - \mathrm{Peff_{mm}}) \quad (4)$$

Where Inet-Net irrigation, ETc-Crop evapotranspiration, P_{eff}- Effective rain fall, but effective rain fall could be calculated using dependable rain (FAO/AGLW) formulae: -

$Peff_{mm}$= 0.6*P_{mon}-10 for P_{mon} <70mm

$Peff_{mm}$= 0.8*P_{mon}-24 for P_{mon} >70mm

The gross irrigation requirement was obtained by the expression:

$$\mathrm{GI} = \frac{\mathrm{NI}}{\mathrm{Ea}} \quad (5)$$

Ea=application efficiency of the furrow for irrigation (60%)

The time required to deliver the desired depth of water into each furrow was calculated by the equation:

$$\mathrm{t} = \frac{\mathrm{l} * \mathrm{w} * \mathrm{dg}}{6\mathrm{Q}} \quad (6)$$

Where l was furrow length (m); w, stood for furrow spacing (m); dg, gross depth of water applied (cm); t, Application time (min); and Q, flow rate (discharge) (l/s). The amount of irrigation water applied at each irrigation application was measured using three-inch calibrated Parshall flume.

2.7 Water productivity

Water productivity plays a crucial role in modern agriculture as it increases yield production per unit of water used under rain fed and irrigated conditions. Water productivity with dimensions of kg/m^3 is defined as the ratio of mass of marketable yield (Y) to the volume of water consumed

by the crop (Wa). Mathematically water productivity can be represented as follow in equation (Ali and Talukder, 2008).

$$WP = \frac{Y}{Wa} \quad (7)$$

WP stands for water productivity (Kg/m^3); Y, economic yield (kg); and Wa, total water applied (m^3).

2.8 Economic analysis

Analysis was carried out to compare the effects furrow irrigation methods, other inputs costs, and return to the producers among different treatments. Economic analysis was employed as suggested by CIMMTY (1988) to determine water application methods based on cost and benefits for head cabbage production.

3. Result and Discussion

3.1 Fresh head cabbage yield response for different furrow irrigation methods

The total head yield of cabbage was significantly affected by application of water through different furrow methods. The maximum total head yield recorded from conventional furrow irrigation was (52.8 t/ha) following the second maximum head yield from alternative furrow irrigation (49.072 t/ha). Yields obtained from furrow and alternate furrow irrigation methods were higher than those from conventional furrow (48.41 t/ha) and alternate furrow (43.84 t/ha) (Aregash *et.al*. 2023) and (42 t/ha) of head cabbage (Gurmu and Mano, 2016). Statistically the minimum total head cabbage yield obtained from farmers' practices was (38.11 t/ha). The yield obtained from all the treatments was better than other previous studies of head cabbage yield; (16.6 t/ha) from full irrigations 100%ETc (Zelalem *et.al*., 2022) and (40t/ha) (JICA and MoA, 2019).

Head diameter (cm)

The highest head diameter (40cm) was recorded at a conventional furrow treatment with application water level of (441.14mm). The next highest second head diameter of (37.37cm) was recoded at alternate furrow treatment method with seasonal amount of water (220.57mm). The lowest head diameter (32.28cm) was recorded at farmer practice with seasonal amount of irrigation water (467.61mm). In comparison to other studies, head diameter obtained from the

three treatment levels (11.83cm) was greatest (Asfaw, 2023). Head diameter and head weight were strongly related with each other; hence, head diameter has a direct contribution to the weight of head yield.

Head length (cm)

Statistically the highest head length (22.72cm) and 21.36cm) were recorded at conventional and alternate furrow irrigation method respectively and the lowest head length (19.28cm) was recorded at farmer practices as shown in table 3 and its data collection process figure 2 below. Other agronomic parameters like scattered canopy, and unmarketable head yield were statistically not significant with each other in all treatments.

Table 3: Intermediate results of analyzed head cabbage yield data

Treatments	HL(cm)	SC	HD(cm)	MHY(t/ha)	UMHY(t/ha)	THY(t/ha)
CFI	22.720a	12.480	40.00a	44.56a	8.24	52.800a
AFI	21.360a	11.800	37.36a	42.32ab	6.75	49.07ab
FP	19.280 b	12.280	32.28b	32.16 b	5.95	38.11b
Mean	21.12	12.187	36.55	39.68	6.98	46.66
LSD(0.05)	0.72	NS	2.00	5.22	NS	5.94
CV	5.36	9.64	8.62	20.79	27.09	20.11

Where: - HL-Head Length, SC- Scattered Canopy, HD-Head Diameter, MHY- Marketable Head Yield, UMHY-Un Marketable Head Yield, THY-Total Head Yield

Figure 2. Field irrigating, its performance and data collections

Water productivity

The maximum water productivity values (22.23 kg/m^3) was obtained at the treatment level of alternate furrow irrigation following the second maximum values of (11.96 kg/m^3) at

conventional furrow method as shown in table 4 below. The maximum value obtained was greater than other previous studies (17.1kg/m^3) on head cabbage productivity through alternate furrow (Aregash *et.al*. 2023). This indicates that alternate furrow irrigation method improves water productivity and yield of head cabbage in the area. The minimum water productivity value (8.15 kg/m^3) was obtained at farmers practices that implies huge amount of irrigation water applied for production of lower yield. Advantages of water productivity (63.34%) and (31.91%) was acquired from alternate and every furrow irrigation methods, respectively.

Table 4. Water productivity values of furrow irrigation methods

Treatments	WP(kg/m^3)
CFI	11.96b
AFI	22.23a
FP	8.15c
Mean	13.09
LSD(0.05)	1.58
CV	8.58

Different amount of water depth and advantages from farmers' practices

Amount of water depths applied were 441.14mm, 220.57mm and 467.61mm in conventional furrow, alternate furrow, and farmers practice, respectively. 26.8% and 22. 3% yield advantage was recorded from conventional and alternate furrow irrigation, respectively. Amount of irrigation water saved; (52.83%) acquired at alternate furrow and minimum values (11.43%) was obtained in conventional furrows over farmer practices. Managing field irrigation water loss through the technology was one of the main goals of the study in water scarce areas.

Table 5. Advantages alternate furrow over conventional furrow and farmers' practices

Treatments	Water depth (mm)	Advantages of water applied (%)	Yield (t/ha)	Advantages of yield (%)	WP (kg/m^3)	Advantages of Water Productivity (%)
CFI	441.14	11.43	52.8	27.8	11.97	31.91
AFI	220.57	52.83	49.07	22.3	22.25	63.34
FP	467.61	-	38.11	-	8.15	-

Economically farmers benefited from the seasonal market price in head cabbage production. Seasonal market price was (35-40ETB) per a single fresh head cabbage and weighs on average (1.32kg), with a price of (37.5ETB) per a single head. Partial budget analysis study indicates that the seasonal market price was (1,278,300 ETB/ha), (1,190,730.7 ETB/ha) and (909,904.4 ETB/ha) from the treatments of every furrow, alternate furrow, and farmers practices respectively as shown in table 6 below. The maximum benefit cost ratio (18.63) was incurred by alternate furrow irrigation method rather than every furrow (17.83) and formers' practice (14.15). The benefit cost ratio values obtained from all treatments were greater than 1.0, which means benefits outweigh the costs of production.

Table 6. Partial budget analysis of head cabbage on hectare base

Variables	Cost (ETB) Items	CFI	AFI	FP
	Seed	12800	12,800	12,800
	Land preparation	4800	4800	4800
	Fertilizer	9900	9900	9900
	Pesticide chemicals	5000	5000	2000
	Watering	15600	7800	15600
	Harvesting	3600	3600	3600
	Transporting	20000	20000	20000
Total Cost (ETB)		71,700	63,900	64,500
Yield(kg/ha)		52,800	49,070	38,110
10% Adjusted yield(kg/ha)		47,520	44,163	34,299
Gross revenue (ETB/ha)		1,350,000	1,254,630.7	974,403.4
Net Benefit (ETB/ha)		**1,278,300**	**1,190,730.7**	**909,903.4**
Benefit Cost Ratio(BCR)		17.83	18.63	14.15

Conclusion and Recommendations

The Ethiopian people live in areas of high-water stress that threaten the country's sustainable development goal. Regular watering through irrigation scheduling technology ensures uniform head formation, prevents head scattering, and increases the diameter of the head. Alternate furrow irrigation is considered to be one of the most effective tools to minimize applied water

irrigation costs and produce a higher head yield. It is a way to save irrigation water and time, improve water productivity, increase cabbage yield and economic income benefits as compared to conventional furrow and farmer practice irrigation methods with recommended fertilizers. The saved irrigation water through alternate furrow method doubles the irrigable land, yield, and income of famers as compared to conventional furrow method. The district farmers under the scheme learned the lesson through field trainings and practiced the technology as a best water saving practice. Therefore, the technology should be scaled up to the other irrigation schemes with the same agro-ecology for transferring knowledge, and skill on irrigation water management technologies.

Acknowledgements

The authors would like to extend sincere thanks to International Water Management Institute for financial support and Areka Agricultural Research Center for logistic facilitations. Our deepest gratitude goes to Angacha District of Agricultural Offices for giving all necessary data and valid information with their continuous supervision starting from site selection to harvesting.

References

Abay Ayalew, Sheleme Beyene, (2011). The influence of Potassium Fertilizer on the Production of Potato (*Solanum tuberosu* l.) at Kembata in Southern Ethiopia.

Abebe E, Bihon K, Gebremedhin Y., (2011). Determinants of land allocation to irrigation and its wealth effect: Evidence from northern Ethiopia. Journal of the Dry lands 4(2):310-319.

Ali, M. H. and Talukder, M. S. U., (2008). Increasing water productivity in crop production-Synthesis. DOI: 10.1016/j.agwat.2008.06.008 · Source: RePEc.

Allen, .R. Pereira, L.A. Raes, .D. Smith, M., (1998). Crop Evapotranspiration Guidelines for Computing Crop Water Requirement. FAO Irrigation and Drainage Paper Number 56, FAO, Rome, and Sons. Inc. Toronto. Canada.

Asfaw Shaka Gosa, Bikila Olika Fufa, (2023). Growth and Yield of Cabbage (*Brassica oleracea* L.) as Influenced by Different Rates of Nitrogen Fertilizer at Guder, West Shoa, Ethiopia. *World Journal of Applied Chemistry*. Vol. 8, No. 2, pp. 39-42. doi:10.11648/j.wjac.20230802.13.

Bindraban, P.S., Verhagen, A., Uithol, P.W.J. and Henstra, P., (1999). A Land Quality Indicator for Sustainable Land Management: The Yield Gap. Report 106, Research Institute for Agrobiology and Soil Fertility (AB-DLO), Wageningen, the Netherlands.

Bouman, B., (2007). A conceptual framework for the improvement of crop water productivity at different spatial scales. Agricultural Systems 93, 43–60.

CIMMYT (International Maize and Wheat Improvement Center), 1988. From agronomic data to farmer recommendations: An economics training manual. Completely Revised Edition. CIMMYT, D.F, Mexico.

Deboch, A., Nigusie, W., Kifle, T., (2023). Evaluation of Furrow Irrigation System on Head Cabbage Yield and Water Use Efficiency in Arbegona Woreda, Ethiopia. *J Water Res, 1*(2), 78-81.

Doorenbos J. and Kassam A. H., (1986). Food and Agricultural Organization of United Nations. Rome. Effects of nitrogen fertilization and irrigation on grain yield, canopy temperature, and nitrogen use efficiency in overhead sprinkler-irrigated durum wheat. Field Crops Research, 191, 54–65.

Food and Agricultural Organization (FAO), (2015). Ethiopia Country Highlights on Irrigation Market Brief. UNFAO, Rome, Itally. Prepared under Food and Agricultural Organization of United Nations (UNFAO)/International Finance Corporation (IFC) cooperation. www.fao.org/3/a-i5196e.pdf.

Gurmu L. and Mano Y., (2016).Training Manual on Agronomic Practice of Selected Vegetable for Development Agents and Farmers at Kenbata Tembaro Zone (Kacha Birra and Angacha Woreda). MENDEL UNIVERSITY PROJECT IN ETHIOPIA *"Effective* irrigation for sustainable agricultural production".

Jemal Nur Hassene, Mukerem Taha Seid, (2017). Comparative Performance Evaluation of Alternate and Convectional Furrow Irrigation under Different Water Application Level on Cabbage Water Use Efficiency and Economic Analysis. *American Journal of* Environmental and Resource Economics. Vol. 2, No. 3, 2017, pp. 123-131. doi: 10.11648/j. ajere. 0203.15.

JICA and MoA., 2019. Project for smallholder horticulture farmer empowerment through promotion of market-oriented agriculture on head cabbage production.

Kijne, J.W., Barker, R., and Molden, D. (eds), (2003) Water Productivity in Agriculture: Limits and Opportunities for Improvement. Comprehensive Assessment of Water Management in Agriculture Series 1. CAB International, Wallingford, UK in association with International Water Management Institute (IWMI), Colombo.

Nebraska University, (2008). Plant growth and yield as affected by wet soil condition due to flooding or over irrigation.

Penas, E.J. and Lindgren, Dale T., (1990). "G90-945 A Gardener's Guide for Soil and Nutrient Management in Growing Vegetables". Historical Materials from University of Nebraska-Lincoln Extension. 1017. https://digitalcommons.unl.edu/extensionhist/1017.

Shitu K, Hymiro A., (2022) Outlook Water Resource Potential and Irrigation Agriculture Practice in Ethiopia. J Soil Water Sci 6(1):253-261

Snapp, S.S.; Shennan, C.; Bruggen, A.V., (1991). Effects of salinity on severity of infection by Phytophthora parasitica Dast, ion concentrations and growth of tomato, *Lycopersicon esculentum* Mill. New Phytol. 119, 275–284. [CrossRef].

Sui J, Wang J D, Gong S H, Xu D, Zhang Y Q., (2015). Effect of nitrogen and irrigation application on water movement and nitrogen transport for a wheat crop under drip irrigation in the North China Plain. Water, 7, 6651–6672.

Sumon Datta, Saleh Taghvaeian, Jacob Stivers, (2017). Understanding Soil Water Content and Thresholds for Irrigation Management.

Wang S J, Tian X H, Liu T, Lu X C, You D H, Li S., (2014). Irrigation, straw, and nitrogen management benefits wheat yield and soil properties in a dry land agro-ecosystem. Agronomy Journal, 106, 2193–2201.

Zelalem Shelemew, Anbese Ambomsa, Dulo Hussen, Ayub Jelde, (2022). Evaluation of the Effect Mulching Practice under Furrow Irrigation on Growth, Yield and Water Productivity of Head Cabbage at Adami Tulu Agricultural Research Center. Science Research. Vol. 10, No. 2, 2022, pp. 37-44. doi: 10.11648/j.sr.20221002.13.

Ethiopian Journal of Water Science and Technology (EJWST)

DOI: https://doi.org/10.59122/18519g6

Vol. 7 , 2024, Pages: 33~53 ISSN(Print): 2220-7643

Analysis of Precipitation Variability at Kulfo River Watershed: Insights from Wavelet Analysis and Back-Trajectory Approaches

Tesfay Mekonnen Weldegerima

Faculty of Meteorology and Hydrology, Water Technology Institute, Arba Minch University, Arba Minch, Ethiopia
Email: tesfaym270@gmail.com

Abstract

Understanding temporal variations and source of precipitations is essential for effective water management and flood risk mitigations, especially in regions prone to heavy precipitation events such as the Kulfo watershed. This study aims to investigate the heavy precipitation patterns at Kulfo River Watershed using wavelet analysis and an advanced atmospheric model to identify temporal precipitation characteristics and trace moisture source regions. Daily precipitation data from 1991-2020 were collected from Ethiopian Meteorology Institute. Meteorological fields on a three-dimensional grid at 1^o x 1^o spatial resolution and daily temporal resolution were also obtained from Global Data Assimilation System (GDAS). Wavelet analysis of the daily precipitation processed with the lag-1 coefficient revealed high power recurrence once every 38 to 60 days at greater than 95% confidence for red noise. The analysis also identified inter-annual periodicity in the periods_ 2002 - 2005 and 2017 - 2019. Back trajectory analysis for 3-day periods up to a heavy precipitation day during the main and short rain seasons indicated the Indian Ocean and Gulf of Eden sources. Trajectories crossed the southern and eastern African escarpment to arrive at the Kulfo watershed. Atmospheric flows associated with the Western Indian monsoon redirected by the low-level Somali winds and Arabian ridge were responsible for the moisture supply. The spatial distribution of relative humidity (RH) during heavy precipitation events ranged from 50% to 88%. The findings indicated that the time-localization of the wavelet power spectrum yielded valuable hydrological information and the back-trajectory approaches provided useful characterization of air mass sources and pathways.

Keywords: extreme precipitation events, HYSPLIT Model, moisture source, power spectrum, Kulfo Watershed

Received: 05 August, 2024; Accepted 10 September, 2024 Published: December, 2024

1. INTRODUCTION

Precipitation is a critical hydroclimatic variable whose spatial and temporal variability can significantly impact human health and livelihoods. Extremes in precipitation, such as droughts and floods, are directly linked to prolonged deficits or surpluses in precipitation. Heavy precipitation events can particularly cause extreme runoff that could damage the human and environmental systems (Knapp et al., 2008; Yisehak et al., 2020). Moreover, studies imply that the occurrence of heavy precipitations will likely increase under climate change. The Intergovernmental Panel on Climate Change Reinman, (2012) reports showed that there had been a more significant increase in the occurrences of heavy precipitations as compared to a significant decrease in many regions of the world. The report also stated that the frequency of heavy precipitation events would increase in many parts of the world in the 21st century.

Another study by Scoccimarro et al., (2013) projected increasing precipitation events over India, Southeast Asia, Indonesia, and central Africa during boreal summer, as well as over southern parts of Africa and South America during boreal winter. Some of the previous studies of extreme precipitation events in Africa indicated that climate change could bring long dry seasons and short rainy seasons. In the East African region, the results of precipitation events by different researchers were inconsistent. For example, Ogega et al., (2020) projected that the number of consecutive dry days would increase while that of wet days would decrease. However, the United Nations Office for Coordination of Humanitarian Affairs OCHA, (2019), reported around 280 people might have died owing to flooding caused by heavy precipitations in 2019 in the region. Similarly, Wainwright et al., (2021) stated that in East Africa the 2019 October –December (OND) heavy rains were registered as one of the wettest seasons in recent decades.

In Ethiopia, different patterns of precipitation have been observed at different spatiotemporal resolutions in recent decades. However, most of the studies were found to have inconsistent results. For example, studies on recent changes in precipitation amount and rainy days in Ethiopia by Seleshi & Zanke, (2004) found no significant trends. Similarly, Mekasha et al., (2014) found no significant trends of extreme precipitation from their study of 11 meteorological stations at three Ethiopian Eco environments. On the other hand, studies by Funk et al., (2012), reported a slightly increasing trend of heavy precipitations in southern and southeastern Ethiopia. Many studies were

conducted on the mean and extreme events of precipitation in and around Southern Ethiopia (Kebede & Bewket, 2009). These studies reveal mostly the trends in the past and upcoming recent decades. Hence, most of these studies were limited to assessing trends and changes in precipitation and variability, including extreme events. However, the analyses covers low spatial and temporal resolutions and consider only the main rainy seasons.

However, extreme precipitation events such as heavy precipitations occur at fine spatial and temporal resolutions from hours to a day and from a single station to small watershed levels. Moreover, the periodic nature of precipitation and the possible moisture source for heavy precipitations remained unrevealed by these studies. During July and August 2020, wide spread flooding affected several zones in Southern Ethiopia including Dawuro, Goffa, Gurage Hadya, Keffa, Silte, and South Omo zones, causing significant disruptions to livelihoods, infrastructure and agricultural activities in the region (OCHA, 2020). These recent occurrences have sparked worries and as a result of global climate change. Heavy precipitations will occur more frequently throughout the 21st century (Trenberth, 2011). Prolonged and intense precipitations have resulted in flooding and inundations in the Kulfo Watershed frequently, causing rivers to overflow and inundate areas along the river banks in lowland plains (Legese et al., 2020).

The main aim of this study is to analyze the temporal patterns of heavy precipitation events and identify their associated moisture sources in the Kulfo Watershed, using daily precipitation data from 1991 to 2020 obtained from ground based hydrometeorological stations within the study watershed. The analysis included statistical summaries, wavelet, and backward trajectory tracers. While the statistical descriptions showed the general patterns of temporal precipitations in the area, the wavelet analysis revealed the temporal characteristics of precipitation. The backward trajectory analysis allowed to track moisture sources back in time for a heavy precipitation event and thus provided information about the transport paths involved and the corresponding relative humidity during the event day. Analysis of heavy precipitation events also had important implications for understanding rates of runoff and management of downstream flood hazards. Understanding the moisture source responsible for heavy precipitation could serve as a warning for adaptations and mitigations of climate shocks.

2. MATERIALS AND METHODS

2.1 Description of the Study Area

Kulfo Watershed is located at the central part of Ethiopian Rift Valley lakes basin, between 37º18`E–37º38`E longitudes and 5º55`N–6º16`N latitudes (Figure 1). The watershed covers an area of about 500 km^2 (Wankie, 2015). Elevation of the catchment ranges from 1235 m to 3547 m above the mean sea level (Temesgen et al., 2023). Kulfo River is one of the dominant rivers in the Abaya–Chamo sub basin system (Mena et al., 2024). It originates from Guge Mountain, flowing towards the east into Lake Chamo. The river serves as a potential source of water supply to the urban and rural communities.

The climate of Kulfo Watershed is classified in the range between tropical to alpine because of its great difference in altitude and topographical elevation. The yearlong precipitation varies from 750 mm in the dry lowlands near Arba Minch town to 2342 mm in the mountainous regions of Gerese, with an average annual precipitation of 1049 mm, and mean annual temperature fluctuating between 23.05º C and 25.87ºC (Ayana et al, 2022). The precipitation distribution is bimodal with the main rainy season occurring from March to May and the second small rainy season from September to November (Mark, 2014). The watershed has an average slope of 16% and is covered dominantly by Cambisol and Regosol soil types. Besides, the soil type is characterized by shallow, moderate to deep, and very deep in depth and sandy clay to clay texture. As a result, severe land degradation resulting from soil erosion, flooding, sediment, and other materials are evident at Chamo Lake (Blumberg & Schütt, 2004). The major land use activity in the area is agriculture. However, agricultural productivity is limited owing to the frequent flood events associated with the heavy precipitations in the area

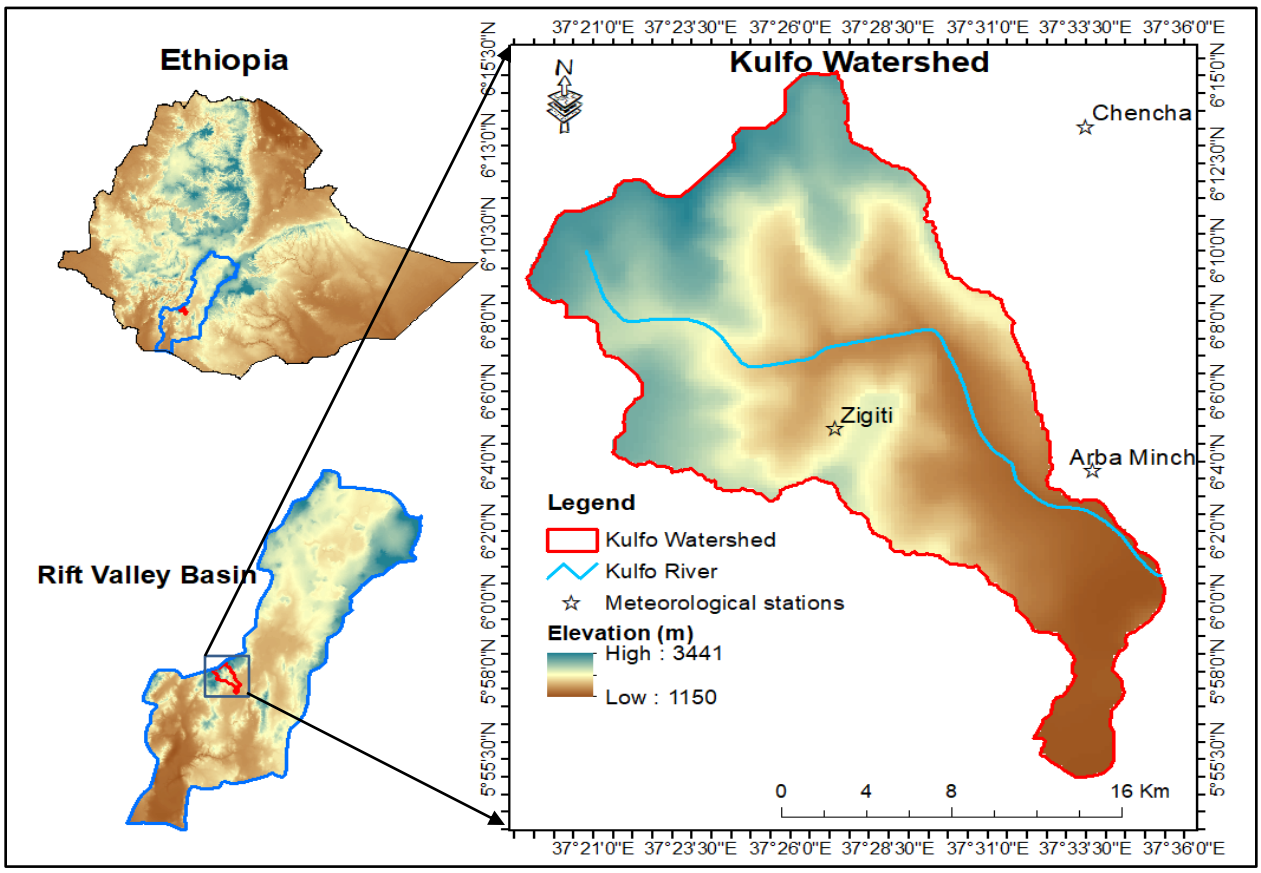

Figure 1. Geographical location of the Kulfo watershed

2.2 Data

Precipitation data of the Kulfo Watershed was collected from the Ethiopian Meteorological Institute (EMI) from 1991 to 2020 at a daily time step. The meteorological stations used for this study covers long-range records, less discontinuity, and are contributing stations to the precipitation of the study watershed. The normal ratio method was used to fill the missing values of the daily time series. The method is widely used to estimate missing values at a station by using data from nearby stations and weighted based on their long term means (Singh & Woolhiser, 2003). Before analyzing the wavelets and moisture source trajectory, the cumulative distribution function of daily precipitation was computed. The different cumulative frequency classes of the daily precipitation were calculated based on the World Meteorological Organization classifications (WMO, 2012). Table 1 illustrates the WMO standard precipitation intensity classifications. And, the precipitation days in the Kulfo Watershed from 1991-2020 are presented in Figure 2. Similarly, the very heavy precipitation days that occurred in the watershed are described in Table 2.

The other precipitation dataset was drawn from meteorological fields on a three-dimensional grid obtained from the Global Data Assimilation System (GDAS). These data sets were available at different spatial and temporal resolutions (Stein et al., 2015). The present study used the 1° × 1° spatial resolution and daily temporal resolution atmospheric fields. By utilizing the GDAS dataset with the specified spatial and temporal resolutions, the study aims to analyze and trace the trajectory of low-level atmospheric flow from a height of 10 meters above the ground at Kulfo Watershed. This information could be valuable in understanding the movement and behavior of precipitation patterns in the study area, shedding light on how meteorological conditions contribute to precipitation at Kulfo Watershed.

Table 1. Classification of precipitation intensity based on the World Meteorological Organization

Precipitation event	Precipitation (Rf) intensity in mm/day
Tiny rain	Rf < 1
Light rain	1 < Rf < 2
Low moderate rain	2 < Rf < 5
High moderate rain	5 < Rf < 10
Heavy rain	10 < Rf < 50
Violent rain	Rf > 50

Table 2. Very heavy precipitation days and amount of Precipitation (R) recorded in mm/day at Kulfo Watershed between 1991 and 2020

Precipitation date			R	Precipitation date			R	Precipitation date			R
Year	Month	Day		Precipitation date	Month	Day		Precipitation date	Month	Day	
1991	8	23	54	**2007**	9	11	67.9	**2015**	4	25	60.5
1992	6	24	71.2	**2008**	9	11	80.8		5	6	55.2
	9	23	50.1		9	24	58.7		10	19	53.7
1993	5	22	40	**2010**	5	9	71.5		11	7	60.7
1997	4	24	68.2	**2011**	5	19	64.5		12	6	54.4
1999	10	13	75.3	**2012**	4	23	59	**2016**	4	26	58
2000	5	5	54.3		4	26	50.8		6	17	56
2005	4	23	102.4		9	4	59.7		11	27	57.7
	5	14	60	**2013**	4	9	55.2	**2017**	4	27	61.3
2006	2	19	51.5		10	15	86.2	**2020**	8	31	68
	6	3	66								

2.3 Wavelet analysis

Wavelet analysis in the present study deals with the localization of the one-dimensional precipitation time series data into two-dimensional time and frequency signals. This helps to get information on both the amplitude of any periodic signals within the time series, and how this amplitude varies with time and depicts the evolution of scales and frequencies with time. The frequency analysis is more of identifying frequency domain of the time series than depicting some hydrological event occurrence for a particular return period. Wavelet analysis methods have functions capable of localizing time and frequency while decomposing several scales in the time series.

In the present study the wavelet analysis procedure is adapted from (Chan, 2000). Hence, a wavelet transform can be defined as an integral convolution of a signal S(t) with respect to the family of functions (daughters) which are derived by stretching or compressing the analyzing wavelet (mother wavelet).

$$\psi_{b,a}(t) = \frac{1}{a^{\frac{1}{2}}}\psi\left(\frac{t-b}{a}\right) \quad (1)$$

Where ψ, is the mother wavelet;

a is scale parameter;

b is position parameter

The scale or dilation parameter is always >0 however, the value is less <1 when the wavelet is dilated in the frequency direction and contracted in the time direction. The reverse condition happens when the scale value is >1. The translation and dilation process are done for each signal at every point throughout the time series.

The continuous wavelet transform is defined as the integral sum of the real signal and the scaled (compressed or dilated) signal. Continuous wavelet transform provides a smooth translation of wavelet power in terms of different wavelet coefficients from the analyzed signal of discrete time series (Torrence & Compo, 1998). In the present study, the continuous wavelet transform for the discrete precipitation time series is equated as,

$$W(b,a) = \frac{1}{(a)^{1/2}}\int \psi^{\star}\left(\frac{t-b}{a}\right)s(t)dt, \quad (2)$$

Where $\psi^{\star}$ is the complex conjugate of ψ

From equation 2, we can calculate different wavelet coefficients and scale averages at different scale values between the start and end dates of the time series. The choice of scales in orthogonal transform is limited to discrete numbers. However, in this study, a none orthogonal wavelet analysis which use a range of arbitrary scales for the Morlet wavelet is applied as suggested by (Torrence & Compo, 1998). The time series can be worked out from 1D precipitation time series into 2D data of wavelet amplitude and phase.

$$s_j = s_0 2^{j\delta j},\ j = 0,1,\dots,J \quad and, \quad J = \delta j^{-1}\log_2(N\delta t/s_0) \tag{3}$$

In this equation, s_o and J are the smallest and the largest possible scale values, respectively. The minimum scale parameter s_o is selected to approximate the equivalent Fourier period to form a time series of $2\delta t$, while Nδt is the total length of the time series. The number of sub-octaves in an octave δj is a positive value with a maximum of 0.5 sampling proportion in scale. Thus, the smaller the value of δj the finer would be the resolution of the wavelet spectrum. To minimize errors at the beginning and end of the wavelet power spectrum, the edges must be padded with sufficient zeros. This padded region, also called the cone of influence, is important in considering edge effects. On the other hand, the amplitude around the edges is discontinuous owing to the zeros filled and represented by the crosshatched regions.

A region that exceeds a 95% confidence interval is drawn for the null hypothesis of the wavelet power spectrum to show if a peak power spectrum of the time series is significantly above the background power spectrum which is the red noise spectrum.

The time averaged wavelet power over the period of the entire time series can be presented by the global power spectrum. This helps us to get information from the time-frequency distributions about how the power changes with time. The global wavelet power, $\bar{W}^2 s(b,a)$, over the entire time series s(t), can be estimated as:

$$\bar{W}^2 s(b,a) = \frac{1}{N}\sum_{b=0}^{N-1} |Ws(b,a)|^2 \tag{4}$$

2.4 Backward trajectories

The Backward trajectory analysis employed in this study is a method used to track the movement of air masses in reverse, starting from a particular location and tracing them back through time. To identify their origins and possible resources of atmospheric components such as moisture or pollutants. This study employed a three-dimensional back trajectory analysis using the Hybrid Single-Particle Lagrangian Integrated Trajectory (HYSPLIT) model version 4.8 developed by the Air Resources Laboratory (Draxler and Hess, 1998). The HYSPLIT model is a widely used atmospheric dispersion model that simulates the movement and dispersion of air parcels by integrating the equations of motion for individual particles. The model considers various atmospheric factors such as wind speed, wind direction, and atmospheric stability to calculate the trajectory of air masses.

This particular study calculated the back trajectories for three days at 10 meters above the ground level. This corresponded to a pressure level of approximately 1000 hPa above sea level. The study used a single source location and a three-dimensional velocity field to simulate the movement of the air masses backward in time. The starting time for the tracer release was set at 00 UTC. The trajectory ensemble option which starts multiple trajectories from the first selected starting location, was used in the present study form the three clustering methods.

The back-trajectory analysis allowed researchers to identify the regions from which air masses originated and tracked their movement over time (Hess et al., 1998; Stein et al., 2015). By analyzing the trajectories, the researchers determined the potential source regions for pollutants or other atmospheric constituents that cause impact on a specific location. This analysis helped to establish source-receptor relationships, which were important for understanding the transport of pollutants, assessing the impact of emissions, and studying atmospheric processes. The first position of wind advection at the start point $p(t)$ is given as:

$$p'(t + \Delta t) \tag{5}$$

Then the first and final guess positions of the trajectory can be estimated by equations (6) and (7) respectively by assuming the three-dimensional velocity vector.

$$p'(t + \Delta t) = p(t) + V(P, t)\Delta t \tag{6}$$

$$P(t + \Delta t) = P(t) + 0.5\,[V(P, t) + V(P', t + \Delta t)]\Delta t \tag{7}$$

3. RESULTS

3.1 Statistical summary of precipitation

Statistical description of the monthly seasonal and annual precipitation of the Kulfo Watershed for the period 1991-2020 is shown in Figures 2 & 3. Accordingly Figure 2 illustrates the cumulative probability distribution of the daily precipitation. Maximum precipitation was recorded in April, May, and October while minimum monthly precipitation was observed in January February, and December (Figure 3). Specifically, the highest monthly precipitation was recorded in May, but the least was observed in February. The standard deviation for the maximum precipitation was smaller than that of minimum precipitation, implying high variability during the dry months.

Similarly, the seasonal and annual precipitation patterns were analyzed (Figures not displayed). The seasonal precipitation of Kulfo Watershed showed two peaks, during the main rain season (MAM), and the second main rain season (SON). MAM received 240.4 to 575.6 mm while SON received 164.9 to 682.8 mm. The precipitation of MAM was less variable when compared to SON during the study period. On the other hand, the annual precipitation received by the area ranged from 855.1 to 1700.2 mm. However, the annual precipitation showed high annual variation of about 500 mm particularly in recent years. (Yisehak et al., 2020) described that the Kulfo Catchment received 620 to 1250 mm precipitation annually.

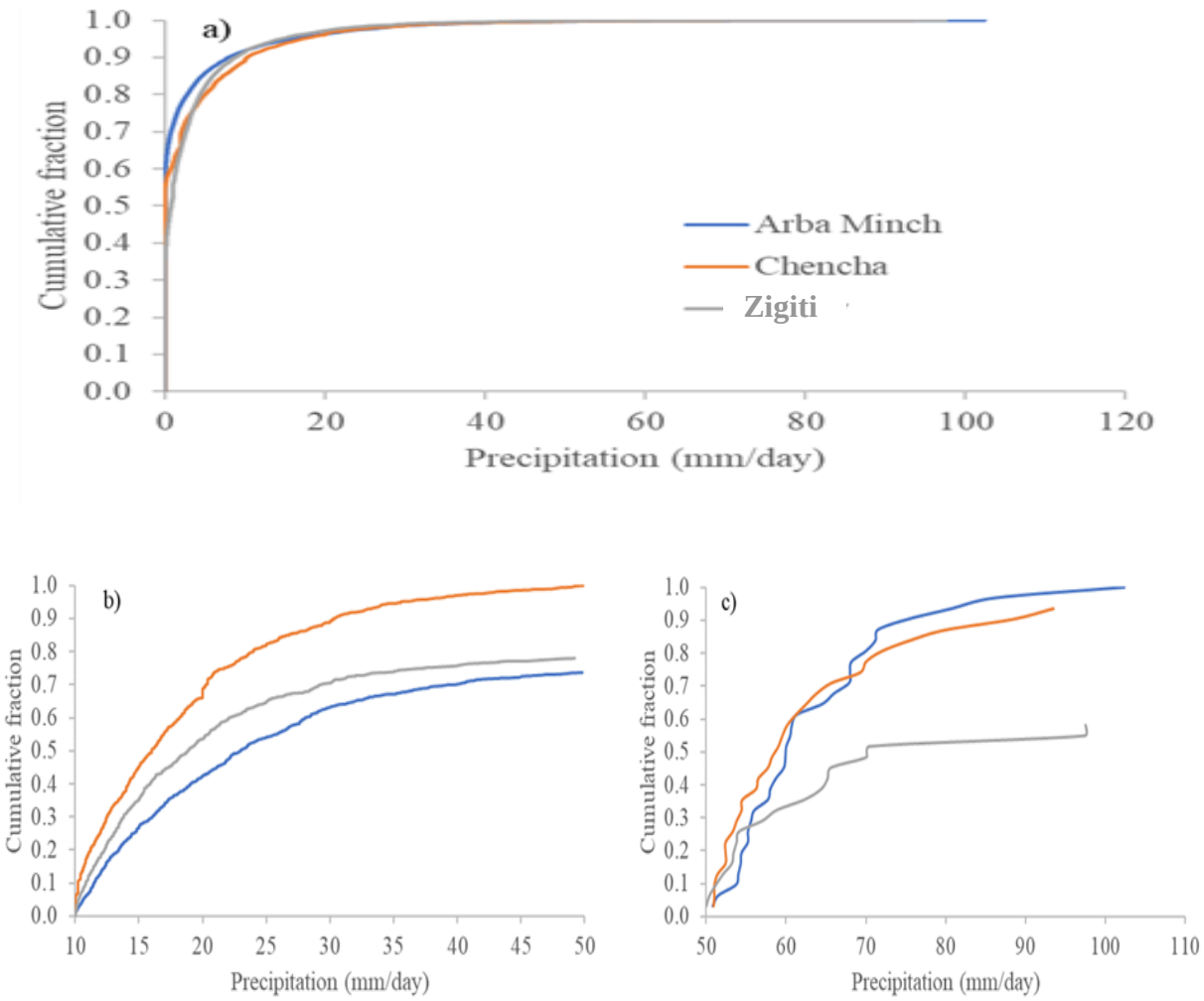

Figure 2. Cumulative distribution of daily precipitation over the Kulfo Watershed; a) All values b) Precipitations between 10 mm and 50 mm and c) Precipitations greater than 50 mm.

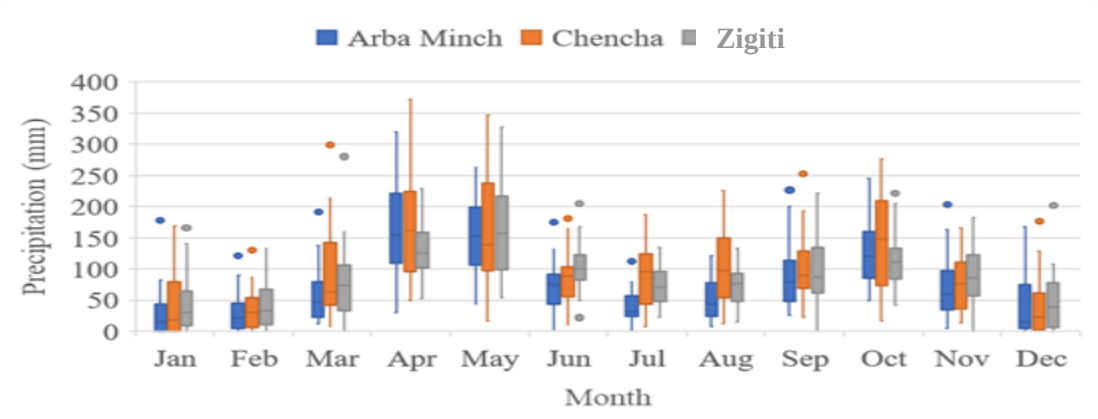

Figure 3. Box plot off Monthly precipitation over the Kulfo Watershed, 1991-2020

3.2 Wavelet Power Spectra

Figure 4 shows a plot of the daily precipitation time series for the Kulfo Watershed from 1991 to 2020 (a), the corresponding local wavelet power spectrum (b), the corresponding global wavelet spectrum (c) and its 95% confidence level for a red-noise process with a lag-1 coefficient. The concentration of power could be easily identified form the frequency or time domain in the figure.

Significant high wavelet power was observed over 32-64 months for the entire length of the record. This is illustrated by the yellow contour band located between the 32-64 months in figure 4(b). This is also illustrated by the major peak in the global wavelet spectrum figure 4(c). The other notable periods of wavelet power included 16-32, 64-128, and 128-256 months which was shown by light yellowish bands. The 16-32-month power showed high variable wavelet power for most of the record. The 64-128 months wavelet power showed oscillatory wavelet powers with high powers from 1992-1998 and 2004-2015 and lower wavelet power from 1999-2003 and 2005-2020. The scale interaction from 35-64 and 64-128 months indicated frequency modulations from early days in the year to every five year, particularly during 1992-1998 and 2004-2015. The scale-average wavelet power is a time series of the average variance in a certain band as presented in Figure 4(d). It illustrated the average of the wavelet power spectra over all scales and a measure of the average year variance over the entire time series. The semi-annual, annual, and biennial bands could be extracted by slicing the time series into corresponding scale averages; for example, 2–8 months for semiannual, 6–12 months for annual, and 16-32 months for biannual bands. A multi-year scale cyclic variance could be seen in 2006-2011 with increasing of variance in the later years. The scale-average wavelet power was used to examine modulation of one time series by another, or modulation of one frequency by another within the same time series.

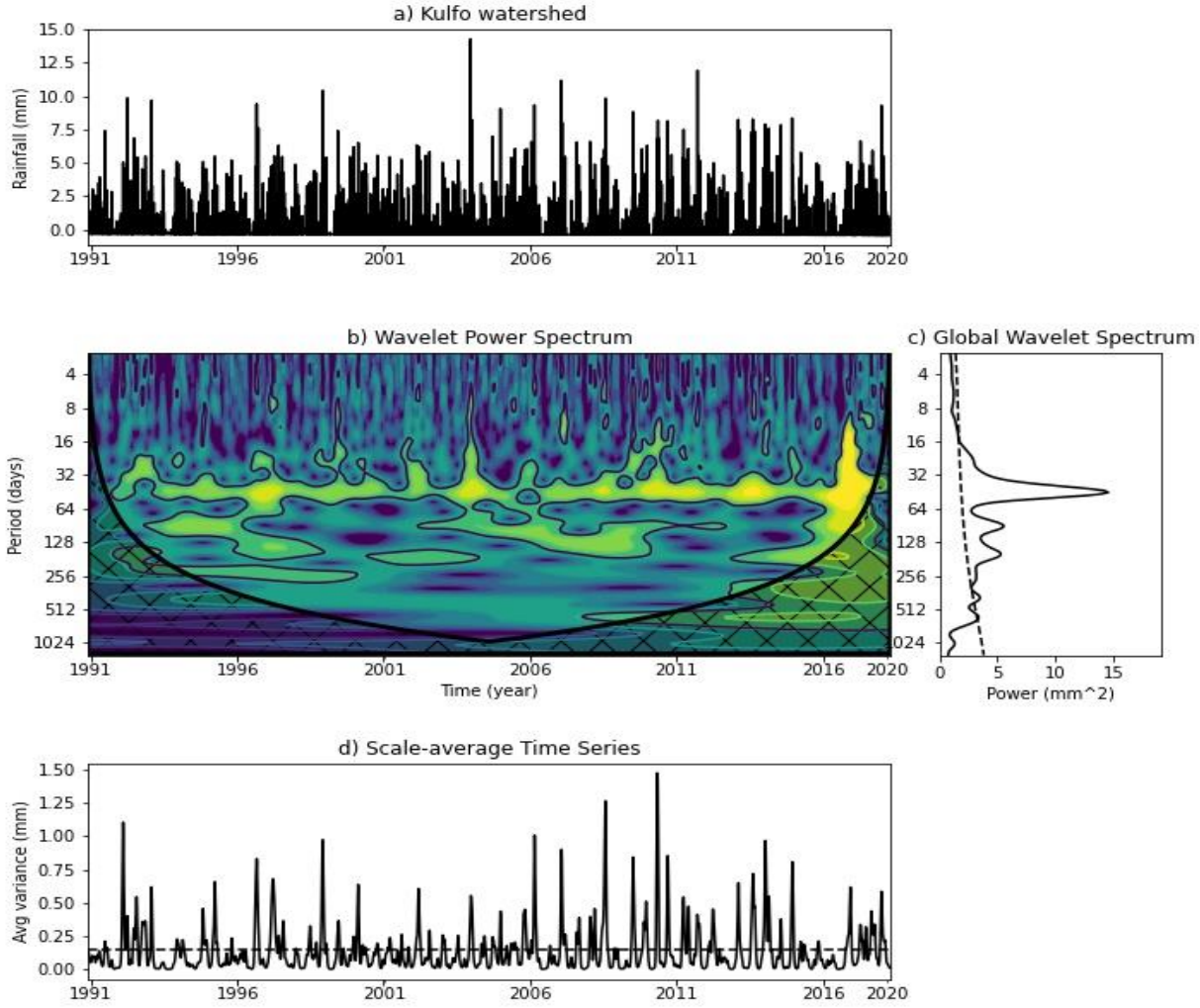

Figure 4. Wavelet spectral analysis of Kulfo Watershed for 1991-2020, (a) Normalized daily precipitation time series. (b) The wavelet power spectrum. The contour levels are chosen so that 75%, 50%, 25%, and 5% of the wavelet power is above each level, respectively. Cross-hatched region is the cone of influence, where zero padding has reduced the variance. Black contour is at 5% significance level, using a red-noise ($\alpha = 0.72$) background spectrum. (c) The global wavelet power spectrum (solid line), red noise assuming a lag-1 of a = 0.72(dashed line). (d) Scale-averaged wavelet power (solid line), 95% confidence level (dashed line).

3.3 Back-trajectories

The Backward Moisture Source Analysis is a valuable tool in atmospheric science to investigate the origins of moisture that contributes to precipitation events. The three days back-ward trajectory of moisture source paths, vertical profile, and corresponding relative humidity distribution of the

Kulfo Watershed for the two seasons is presented in this section. The analysis was performed for two extremely heavy days: one from the main rain season, 21st May 2011 and one from the short rain season, 31st October 2020. The selection of these two seasons was to assess the seasonal difference in moisture sources and paths at Kulfo Watershed. The prevailing atmospheric circulation patterns during the analysis period showed a dominant movement of moisture-laden air masses from local to regional sources.

The backward moisture source analysis for a three-day period back since 21st May 2011 was sourced from the southwest of the Indian Ocean near to Madagascar. The Indian Ocean source revealed significant insights into the moisture pathways and sources influencing precipitation in the study area. Moisture transport was dominated by distinct pathways which suggested a strong connection between the southeastern low-level flow and the moisture supply to the study area during the rainy season (Figure 5a). The relative humidity distribution showed a range of 3% to 87% across the region, indicating the presence of favorable conditions for moisture accumulation. Higher relative humidity values were observed in moisture source regions; for instance, the southwest Indian Ocean (80%) while comparatively lower values were found in areas farther away (<50%) (Figure 5b). Localized variations in relative humidity were evident because of orographic effects or the influence of local topography.

a) b)

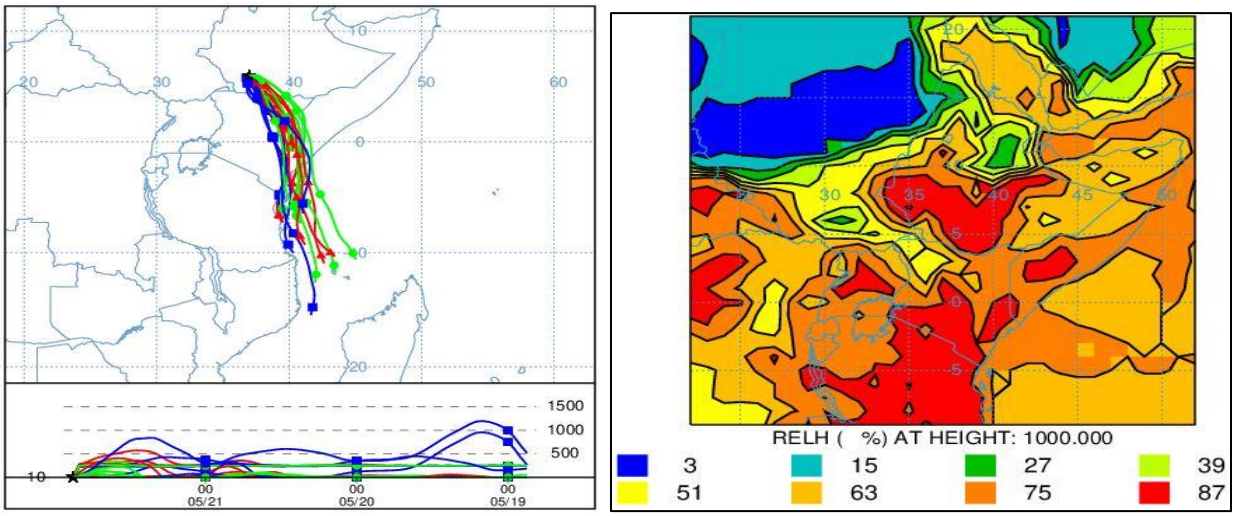

Figure 5. Back-trajectory plane view of moisture source (left) and the corresponding relative humidity (right) of the Kulfo Watershed for 21st May 2011.

The Kulfo Watershed exhibited a combination of local and remote moisture sources, each making a significant contribution to the observed precipitation. The moisture source and pathways analysis conducted for a three-day period since 31st October 2020 revealed different insights into the origins of moisture comared to 21st May 2011. The analysis indicated that the Gulf of Aden served as the primary moisture source, contributing to the moisture influx, while the southwest Indian Ocean also accounted for the moisture supply (Figure 6a). The moisture pathways exhibited a dominant flow from the Gulf of Aden towards the study region, with some local moisture-laden air masses following this trajectory. Additionally, moisture sources around the study area, such as nearby water bodies and local evapotranspiration, contributed to the overall moisture availability. These findings raised our awareness about moisture dynamics at Kulfo Watershed and provided valuable information for water resource management and forecasting in the region. Figure 6b illustrates the relative humidity distribution which ranges from 11% to 88%. This wide range indicated significant variability in moisture content across the area. The maritime influence from the Gulf of Aden caused increased humidity levels in regions closer to the coast, particularly those adjacent to the Gulf. As moist air travelledby prevailing winds, coastal and nearby areas experinced higher raltive humidity compared to locations farther away from the moisture source.

a) b)

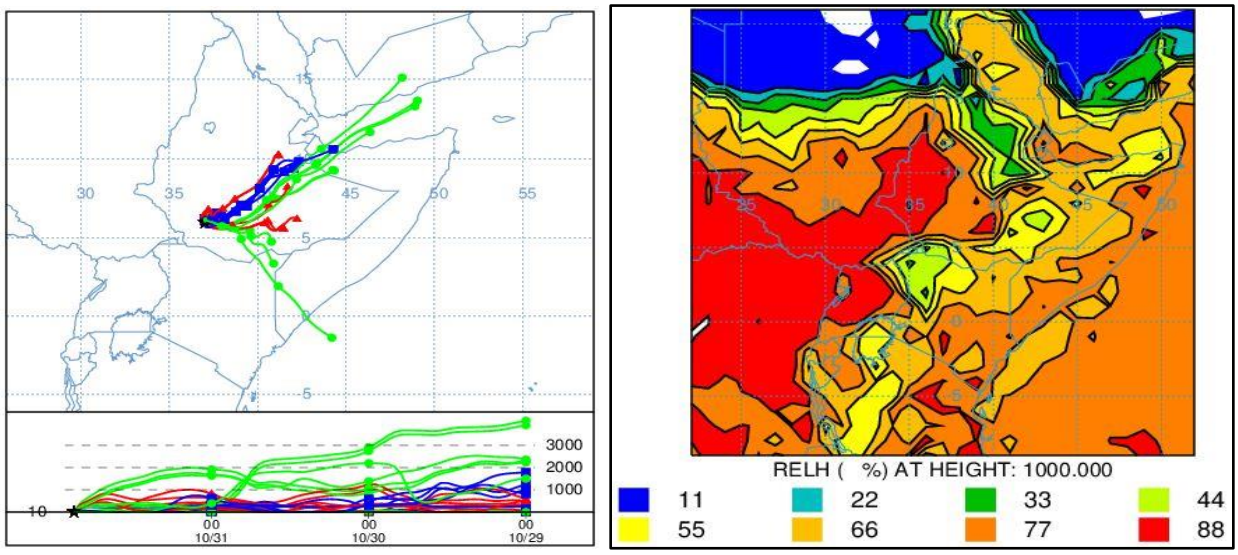

Figure 6. Back-trajectory plane view of moisture source (left) and the corresponding relative humidity (right) of the Kulfo Watershed on 31st October 2020.

4. DISCUSSIONS

The analysis of heavy precipitation events at Kulfo Watershed showed the occurrence of frequent extreme events in the watershed. The statistical summary of precipitation showed that precipitation at Kulfo Watershed was highly variable and inconsistent from month to month and from season to season. The variability was, however, relatively lower during the main rainy months (MAM) as compared to the short rain months (SON) and the other dry months. Similarly, the annual precipitation showed variability inter-annually, with the increase of wet years in the last years of the study period. (Kuma et al., 2021) reported a trend of increasing monthly precipitation in April and January at Bilate Watershed from 1981-2008. Similarly, Funk et al. (2012) found a trend of rising precipitation which was not significant in the lowlands of southern and southeastern Ethiopia.

The wavelet power spectra analysis revealed significant temporal variations in the intensity of heavy precipitation events. The results indicated dominant periodicities at multiple time scales, ranging from short-term oscillations to longer-term trends. For example, the analysis identified a significant increase in the intensity of heavy precipitation events at a decadal scale, indicating a possible influence of climate change on precipitation variability. The observed increase in heavy precipitation events aligns with previous studies conducted in southern Ethiopia. Gummadi et al., (2018), for example, indicated a statistically significant upward trend in the frequency and intensity of heavy precipitation events over the past three decades. Furthermore, (Belay et al., 2019) conducted a study on the interannual variability of precipitation in southern Ethiopia using satellite-derived datasets. The results showed the role of large-scale climate systems particularly El Niño-Southern Oscillation (ENSO) in shaping heavy precipitation patterns. Periods marked by El Niño events tended to correspond with heightened occurrences of intense precipitation across the study area.

Finally, at Kulfo Watershed the primary sources of atmospheric moisture were found to shift with the season's oceanic sources such as the Indian ocean and the Gulf of Aden. The moisture sources contributed more significantly during specific months, while continental moisture sources became more prominent during others. This seasonal variability suggested the need to account for broader regional meteorological dynamics analyzing heavy rainfall events in the area. (Dubache et al.,

2019) investigated the relationship between the Indian Ocean Dipole (IOD) and precipitation variability in southern Ethiopia. Their analysis revealed a significant correlation between positive IOD events and enhanced heavy precipitation in the study area. These results suggested that regional climate modes such as Gulf of Eden, and ENSO and IOD played a role in modulating interannual variations in heavy precipitation intensity. Moreover, the analysis of relative humidity distribution during heavy precipitation events revealed distinct spatial patterns. Regions with high relative humidity were found to be closely associated with areas exhibiting enhanced precipitation.

In addition to the seasonal and oceanic influences on moisture availability, topography, land use changes, and deforestation interacted with the atmospheric processes to shape local precipitation dynamics at Kulfo Watershed. The rugged terrain of the area enhanced orographic lifting, amplifying precipitation in elevated areas. This is particularly evident when moist air masses are funneled inland maritime sources like the Gulf of Aden. However, ongoing land use changes such as agricultural expansion, urbanization, and deforestation could significantly alter surface evapotranspiration rates, soil moisture retention, and local convective processes (Knapp et al., 2008). These landscape modifications might disrupt the local moisture recycling mechanism, potentially intensifying dry spells or exacerbating flooding events (Ayele et al., 2024). Therefore, integrating land surface characteristics with atmospheric moisture tracking approaches would be vital for designing adaptive water management strategies responsive not only to seasonal climate patterns but also to evolving land use dynamics in the region.

5. CONCLUSIONS

In this study the wavelet analysis examines the temporal variations of extreme precipitation and the backward trajectory identifies the moisture sources and pathways associated with these events. The wavelet analysis revealed significant temporal variations in the intensity of extreme precipitation events, with dominant periodicities observed at multiple time scales. The findings indicated an increase in the intensity of extreme precipitation events at a decadal scale, suggesting possible influences of long-term climate variability or climate change on precipitation patterns at Kulfo River Watershed. These results contributed to a better understanding of the dynamics and variability of extreme precipitation events in the region. The backward trajectory analysis provided insights into the moisture sources and pathways contributing to extreme precipitation events. The

analysis identified specific source regions, such as nearby oceanic or continental areas, from which moisture was transported to the study area. This information was crucial for understanding the spatio-temporal patterns of moisture transport and the associated factors driving extreme precipitation events at Kulfo River Watershed.

However, the methodologies employed in this study were not without limitations, which should be acknowledged for a balanced interpretation of the results. For example, the backward trajectory analysis helped trace moisture paths but had uncertainties due to course resolution and simplified assumptions of the GDAS model. Additionally, the complex typography of the Kulfo Watershed might introduce local atmospheric dynamics not fully captured by the trajectory model, potentially affecting the accuracy of moisture attribution. Similarly, the wavelet analysis, although effective in detecting periodicities in precipitation time series, relied on assumptions of stationarity within the segments of the signal, which might oversimplify the inherently nonlinear and chaotic nature of hydrometeorological systems.

Overall, the research highlighted the importance of investigating extreme precipitation events and their underlying mechanisms in the context of climate variability and change. The findings would contribute to the scientific understanding of extreme precipitation at Kulfo River Watershed, aiding in the development of strategies for managing and adapting to these events. Further research would be required to explore the linkages between extreme precipitation, climate drivers, and potential impacts on the local environment and society.

Acknowledgments: The author of this work is grateful to the Ethiopian Meteorological Institute (EMI) for providing the precipitation dataset.

Data availability: Data will be available up on request.

REFERENCES

Ayele, E. G., Buba, Z. M. & Garo, O. O. (2024). Evaluation of satellite rainfall products to estimate extreme flow events over the Kulfo watershed in Ethiopia. *Water Practice and Technology*, *19*(11), 4647–4666. https://doi.org/10.2166/wpt.2024.278

Belay, A. S., Fenta, A. A., Yenehun, A., Nigate, F., Tilahun, S. A., Moges, M. M., Dessie, M.,

Adgo, E., Nyssen, J. & Chen, M. (2019). Evaluation and application of multi-source satellite rainfall product CHIRPS to assess spatio-temporal rainfall variability on data-sparse western margins of Ethiopian highlands. *Remote Sensing*, *11*(22), 2688.

Blumberg, S. & Schütt, B. (2004). Character of lake floor sediments from central Lake Abaya, South Ethiopia. *Lake Abaya Research Symposium 2004-Proceedings*, *4*, 1–10.

Chan, A. (2000). Wavelet Techniques for the Analysis and Synthesis of Rainfall Data. *Journal of Water Management Modeling*, *6062*, 141–162. https://doi.org/10.14796/jwmm.r206-08

Draxler, R. R, and Hess, G. D. (1998). Description of the HYSPLIT_4 modeling system of trajectories, dispersion, and deposition. *Australian Meteorological Magazine*, *47*(1998), 295–308.

Dubache, G., Ogwang, B. A., Ongoma, V. & Towfiqul Islam, A. R. M. (2019). The effect of Indian Ocean on Ethiopian seasonal rainfall. *Meteorology and Atmospheric Physics*, *131*(6), 1753–1761.

Funk, C. C., Rowland, J., Eilerts, G., Kebebe, E., Biru, N., White, L. & Galu, G. (2012). A climate trend analysis of Ethiopia. In *Fact Sheet*. https://doi.org/10.3133/fs20123053

Gummadi, S., Rao, K. P. C., Seid, J., Legesse, G., Kadiyala, M. D. M., Takele, R., Amede, T. & Whitbread, A. (2018). Spatio-temporal variability and trends of precipitation and extreme rainfall events in Ethiopia in 1980–2010. *Theoretical and Applied Climatology*, *134*, 1315–1328.

Hess, M., Koepke, P. & Schult, I. (1998). Optical Properties of Aerosols and Clouds: The Software Package OPAC. *Bulletin of the American Meteorological Society*, *79*(5), 831–844. https://doi.org/10.1175/1520-0477(1998)079<0831:OPOAAC>2.0.CO;2

Kebede, G. & Bewket, W. (2009). Variations in rainfall and extreme event indices in the wettest part of Ethiopia. *SINET: Ethiopian Journal of Science*, *32*(2), 129–140.

Knapp, A. K., Beier, C., Briske, D. D., Classen, A. T., Luo, Y., Reichstein, M., Smith, M. D., Smith, S. D., Bell, J. E., Fay, P. A., Heisler, J. L., Leavitt, S. W., Sherry, R., Smith, B. & Weng, E. (2008). Consequences of More Extreme Precipitation Regimes for Terrestrial Ecosystems. *BioScience, 58*(9), 811–821. https://doi.org/10.1641/B580908

Kuma, H. G., Feyessa, F. F. & Demissie, T. A. (2021). Hydrologic responses to climate and land-use/land-cover changes in the Bilate catchment, southern Ethiopia. *Journal of Water*

and Climate Change, *12*(8), 3750–3769. https://doi.org/10.2166/wcc.2021.281

Legese, B., Gumi, B. & Bule Hora, E. (2020). Flooding in Ethiopia; causes, impact and coping mechanisms. A review. *International Journal of Research and Analytical Reviews*, *7*(3), 707–717.

Mark, R. J. (2014). Southern Ethiopia Rift Valley lake fluctuations and climate. *Scientific Research and Essays*, *9*(18), 794–805. https://doi.org/10.5897/sre2014.6062

Mekasha, A., Tesfaye, K. & Duncan, A. J. (2014). Trends in daily observed temperature and precipitation extremes over three Ethiopian eco-environments. *International Journal of Climatology*, *34*(6), 1990–1999. https://doi.org/https://doi.org/10.1002/joc.3816

Mena, N. B., Ayele, E. G., Chora, H. G. & Dada, T. T. (2024). Assessing the effect of rating curve uncertainty in streamflow simulation on Kulfo watershed, Southern Ethiopia. *Journal of Water and Climate Change*, *15*(9), 4199–4219. https://doi.org/10.2166/wcc.2024.645

OCHA. (2019). Ethiopia humanitarian needs overview 2019. *Relief Web*, *Feb 2019*, 8.

OCHA. (2020). *Ethiopia: 2020 kiremt weather outlook, Floods Update No.3 as Of 18 August 2020* . *3*, 1–5.

Ogega, O. M., Gyampoh, B. A. & Mistry, M. N. (2020). Intraseasonal precipitation variability over West Africa under 1.5 °c and 2.0 °c global warming scenarios: Results from cordex RCMS. *Climate*, *8*(12), 1–19. https://doi.org/10.3390/cli8120143

World Meteorological Organization, WMO (2012). Chapter 14. Observation of present and past weather; state of the ground. In *Guide to Meteorological Instruments and Methods of Observation* (pp. I–14). WMO Geneva, Switzerland.

Reinman, S. L. (2012). Intergovernmental Panel on Climate Change (IPCC). *Reference Reviews*, *26*(2), 41–42. https://doi.org/10.1108/09504121211205250

Scoccimarro, E., Gualdi, S., Bellucci, A., Zampieri, M. & Navarra, A. (2013). Heavy precipitation events in a warmer climate: Results from CMIP5 models. *Journal of Climate*, *26*(20), 7902–7911. https://doi.org/10.1175/JCLI-D-12-00850.1

Seleshi, Y. & Zanke, U. (2004). Recent changes in rainfall and rainy days in Ethiopia. *International Journal of Climatology: A Journal of the Royal Meteorological Society*, *24*(8), 973–983.

Singh, V. P. & Woolhiser, D. A. (2003). Mathematical Modeling of Watershed Hydrology.

Perspectives in Civil Engineering: Commemorating the 150th Anniversary of the American Society of Civil Engineers, 345–367. https://doi.org/10.1061/(asce)1084-0699(2002)7:4(270)

Stein, A. F., Draxler, R. R., Rolph, G. D., Stunder, B. J. B., Cohen, M. D. & Ngan, F. (2015). Noaa's hysplit atmospheric transport and dispersion modeling system. *Bulletin of the American Meteorological Society*, *96*(12), 2059–2077. https://doi.org/10.1175/BAMS-D-14-00110.1

Temesgen, E., Goshime, D. W. & Akili, D. (2023). Determination of groundwater potential distribution in Kulfo-Hare watershed through integration of GIS, remote sensing, and AHP in Southern Ethiopia. *Journal of Groundwater Science and Engineering*, *11*(3), 249–262. https://doi.org/10.26599/JGSE.2023.9280021

Torrence, C. & Compo, G. P. (1998). A Practical Guide to Wavelet Analysis. *Bulletin of the American Meteorological Society*, *79*(1), 61–78. https://doi.org/10.1175/1520-0477(1998)079<0061:APGTWA>2.0.CO;2

Trenberth, K. E. (2011). Changes in precipitation with climate change. *Climate Research*, *47*(1–2), 123–138. https://doi.org/10.3354/cr00953

Wainwright, C. M., Finney, D. L., Kilavi, M., Black, E. & Marsham, J. H. (2021). Extreme rainfall in East Africa, October 2019–January 2020 and context under future climate change. *Weather*, *76*(1), 26–31. https://doi.org/10.1002/wea.3824

Wankie, T. (2015). *Assessment of Hydrologic Impacts of Land-use Change in Kulfo River Watershed Using SWAT*.

Yisehak, B., Adhena, K., Shiferaw, H., Hagos, H., Abrha, H. & Bezabh, T. (2020). Characteristics of hydrological extremes in Kulfo River of Southern Ethiopian Rift Valley Basin. *SN Applied Sciences*, *2*(7), 1–12. https://doi.org/10.1007/s42452-020-3097-1

Ethiopian Journal of Water Science and Technology (EJWST)

DOI: https://doi.org/10.59122/19519g6

Vol. 7 , 2024, Pages: 54~76 ISSN(Print): 2220-7643

Assessment and Upgrading of Local Scour Depth Estimation Equation for Bridge Piers in Kombolcha-Weldia Highway, Ethiopia

Shumye HailemariamYirsaw[1], Aschalew Cherie Workneh[2*], Chekole Tamalew Asnik[2], Sufiyan Abdulmenan Ousman[3]

[1]Amhara Design and Supervisión Works Enterprise, Bahir Dar, Ethiopia
[2]Faculty of Water Resources and Irrigation Engineering, Arba Minch University, Ethiopia
[2*]Faculty of Water Resources and Irrigation Engineering, Arba Minch University, Ethiopia
[3] Faculty of Hydraulic and Water Resources Engineering, Arba Minch University,Ethiopia
*Corresponding Author: Email: aschalewc@gmail.com, P.O.Box 21, Arba Minch University, Arba Minch,Ethiopia

Abstract

Frequent erosion caused by turbulent river flow has significantly affected bridge stability along the Kombolcha-Weldia highway in Ethiopia's Amhara region. This has led to erosion of foundation over the years. To tackle this issue, six established scour depth estimation equations—Colorado State University (CSU), Bruisers, Jain and Fischer, Froehlich, HEC-18/Muller, and Laursen's empirical equation—were assessed for their accuracy in predicting bridge pier scour depths. A detailed field study was conducted. This included topographic surveys, evaluations of pier alignment and shape, riverbed material sampling, and direct measurements of scour depth at five selected bridges. Peak flood discharge was calculated using the Rational Method for catchments under 50 ha and the Soil Conservation Service (SCS) unit hydrograph method for larger catchments. Total scour depth was determined by examining three main components: long-term degradation, contraction scour, and local scour. Key variables such as pier width, shape, and flow alignment were found to significantly influence scour magnitude. The predicted scour depths from the selected formulas were compared with field-measured values. The analysis showed that the equations from Jain and Fischer, Laursen, and Froehlich provided more accurate estimates of scour depth than the others. Among these, the Jain and Fischer equation was recognized as the most suitable for predicting local scour in both sand-bed and gravel-bed rivers within the study area. Based on these findings, it is recommended to prioritize the Jain and Fischer equation for estimating scour depth in similar hydrological and geomorphic conditions. This approach will help improve the assessment and mitigation of bridge foundation risks in the region.

Keywords: Bridge Pier Scour; Design return period; Jain and Fischer equation; Kombolcha-Weldia; Scour depth estimation.

Received: 05 August, 2024; Accepted 10 September, 2024 Published: December, 2024

1. INTRODUCTION

Flowing water at high velocities increases the risk of bridge foundation scour, due to its erosive capacity to excavate and transport sediment from the stream bed and banks (Ebrahimi et al., 2018). Scouring rate varies from material to material. The erosion resistance of soil or rocks is a primary controlling factor in how quickly it is transported by flowing water (Annandale, 2000). Granular soils are rapidly eroded by flowing water due to their non-cohesive character whereas cohesive, cemented, and compacted soils are more resistant to scouring effect (Sheppard et al., 2014). Under constant flow conditions, scour reaches to its maximum depth (Wang, 2010); in sand and gravel bed materials in a short span of time; cohesive bed materials in some days; glacial tills, sand stones and shale in few months; limestone in years and dense granites extends to some centuries (Temesgen et al., 2015). Scour occurs due to high velocity of river flow (Sarlak and Tigrek, 2011) and becomes more aggravated by debris when rock boulders, gravel and silt are carried away by river current (Yanmaz and Çalamak, 2016, Ebtehaj et al., 2017). When scour becomes severe, foundation materials existing below the pier footing may become prone to erosion (Kothyari, 2007) leaving the structure unsupported leading to collapse (Ghazvinei et al., 2012; Zaid et al., 2019).

Research in Ethiopia has not been extensively conducted to find bridge failure due to scouring. In recent years, initiation has been taken up by bridge management systems in order to prevent such disasters. As a result, measures have been proposed to rehabilitate and redesign the damaged bridges (Girma, 2018). According to Ethiopian Road Authority (ERA) 2013, 445 road and highway bridges in northern, north-eastern and eastern parts of Amhara region and some parts of Afar region were inspected. Thus, it was found that 112 bridges were under bad to worse conditions due to scouring. A number of scour depth estimation equations have been in practice by technocrats (Vonkeman and Basson, 2018). Once flow velocity in the channel reaches the piers, sediments in the vicinity of the piers start moving followed by initialization of scouring (Shukri, 2017). Though several equations are developed and implemented for numerous bridge designs in the world, modifications to the existing equations are imminent and further improvement of the equations is anticipated. In this research, six scour equations using field data were selected for comparison for scour depth determination. Owing to the empirical nature of the equations (Kafi and Alam 1995; Ghani and Nalluri 1996; Yahaya and Ghani 1999; Yahaya et al., 2002, Ebtehaj et al., 2016)

unanimous decision cannot be taken up to find the superlative equation among the existing equations since rate and type of scouring varies from one to the other (Gilja and Mari, 2018).

A significant gap exists in the detailed performance evaluation of scour depth prediction equations in Ethiopia. This study aims to address this gap by comparing six key scour depth equations. To ensure strong validation, predicted scour depths from each equation were compared by field measurements collected from bridge sites throughout Ethiopia.

2. MATERIAL AND METHODS

2.1 Study Area

The study area encompasses the Kombolcha to Weldia roadway. This route crosses many rivers, depressions, and gullies (Figure 1). It moves through hilly and uneven land where rivers have high runoff rates and face scouring issues especially downstream at bridges and other structures. Land use and land cover (LULC) in the area mainly includes gently sloping farmland and thinly vegetated grasslands. The catchment has erosion-prone alluvial deposits which heighten the risk of scouring.

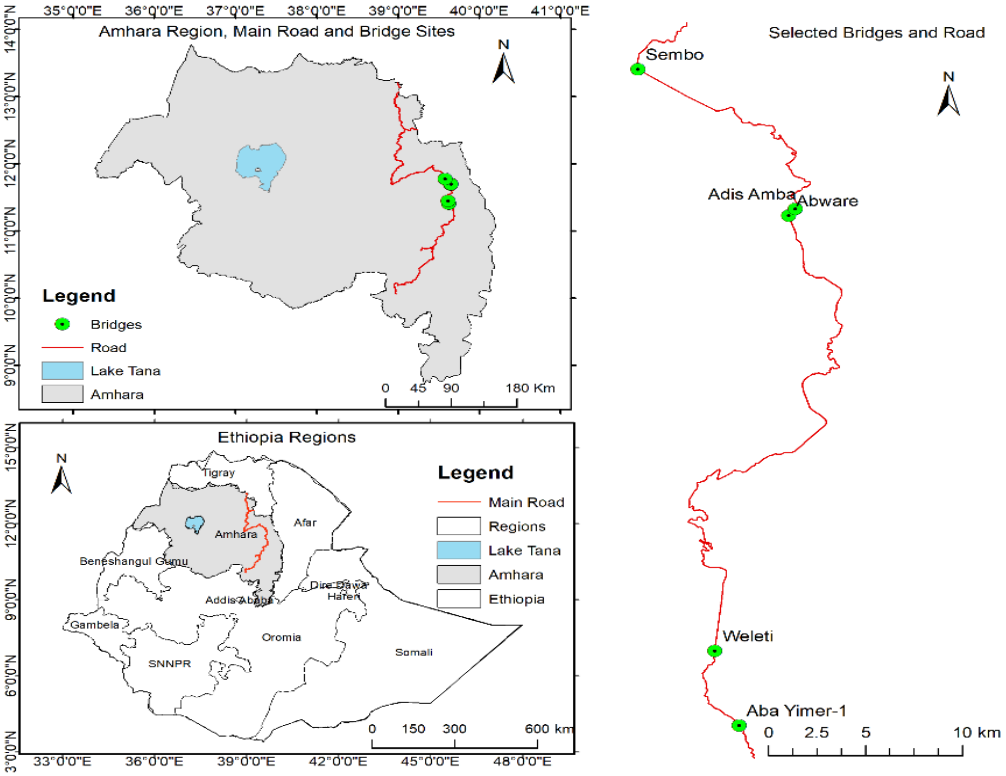

Figure 1. Location of scoured bridges in the study area

2.2 Salient Features of Selected Bridges

The main road runs from Kombolcha to Weldia, passing through mountainous and rolling land. For this reason, scouring problems have been common along this stretch of road. Five bridges from Haik to Weldia were chosen because these areas were prone to bridge scour failures. As shown in Figure 2, the catchment areas of these bridges had poorly vegetated grass and cultivated land with gentle slopes, such as at Adis Amba, and the stream beds were sandy. This contributed to high runoff and scouring issues at the downstream outlets of the bridges. In addition, social need, budget consideration and scour condition of the sites were the criteria to select road segment. . Field data were collected from the five existing bridges of this road segment. The construction history and design data were obtained from the regional Roads Authority and the Kombolcha District Road Construction Office. Table 1 presents the key features of the selected bridges and their scouring conditions, including information on location, bridge type, and length.

Figure 2. Photo of the selected five bridges under this study

Table 1: Location of selected bridges and some salient features of bridges

Sl. No.	Bridge Name	Northing	Easting	Altitude (m) a.m.s.l	Bridge Type	Bridge Length (m)	Bridge Condition
1	Aba Yimer-1	1260648	568497	1699.06	RC Slab Culvert	6	Under scouring
2	Weleti	1265266	567254	1548.17	RC Box Culvert	10	Under scouring
3	Abware	1292272	570938	1642.36	RC Deck Girder	16	Under scouring
4	Sembo	1301342	563305	1884.03	RC Slab Culvert	8	Under scouring
5	Adis Amba	1292697	571268	1637.77	RC Deck Girder	64	Under scouring

2.3 Morphology of the River

The morphology of the rivers primarily affected scouring at bridge foundations, influenced by the underlying geology, climate, and vegetation. Field analysis confirmed that all five rivers had alluvial bed and bank materials, making them very sensitive to erosion. The rivers had specific characteristics. The Aba Yimer River changed from a wide, shallow channel upstream to a narrow, deeper section downstream with mixed alluvial and rocky banks. The Weleti River carried coarse sediments along banks of alluvium and silt-clay. The Abware River, being a seasonal channel, had a sand bed prone to erosion and confined to deep gorges. The Adis Amba River flowed through an area with grass-covered alluvial banks. Lastly, the Sembo River had a gravel bed and moved boulders with banks supported by short bushes and no ongoing sand mining. The consistent presence of erodible alluvial materials indicated a high potential for scouring at any hydraulic structure built across these rivers.

Figure 3. Morphological characteristics of Rivers for selected bridges

2.4 Data Collection

2.4.1. Meteorological and Stream Flow Data

The primary data collected during fieldwork included scour depth, river cross section, stage-discharge measurements, riverbed and bank materials, and topographic surveys of the study area.. Secondary data such as hydrologic and design information for each selected bridge were gathered from various organizations. For instance, design cross section data were obtained from the Ethiopia Roads Authority Kombolcha District Office. This data was crucial for comparing with the current measured cross sections of the selected bridges. Maximum 24-hour rainfall data from 1954 to 1989 was collected from three rain gauge stations: Haik, Sirinka, and Weldia. These stations were chosen based on their proximity to the selected bridges, the quality of the recorded data, and data availability. Since the rivers had no gauging stations, peak discharge was estimated using the rainfall-runoff relationship.

2.4.2. Topographic maps

The topographic map of the study area was extracted from the Digital Elevation Model (DEM) of the Amhara region, having a resolution of 30m x 30m. The integration of regional raster, shapefile, and field survey data enabled the systematic classification of soil types, land use, land cover (LULC), and other catchment characteristics. The catchment parameters were estimated accurately with the Arc Hydro extension tool in Arc GIS environment. The LULC and soil map were obtained from the Ministry of Water and Energy. The physical characteristics of the watershed were extracted from the DEM (Figure 4).

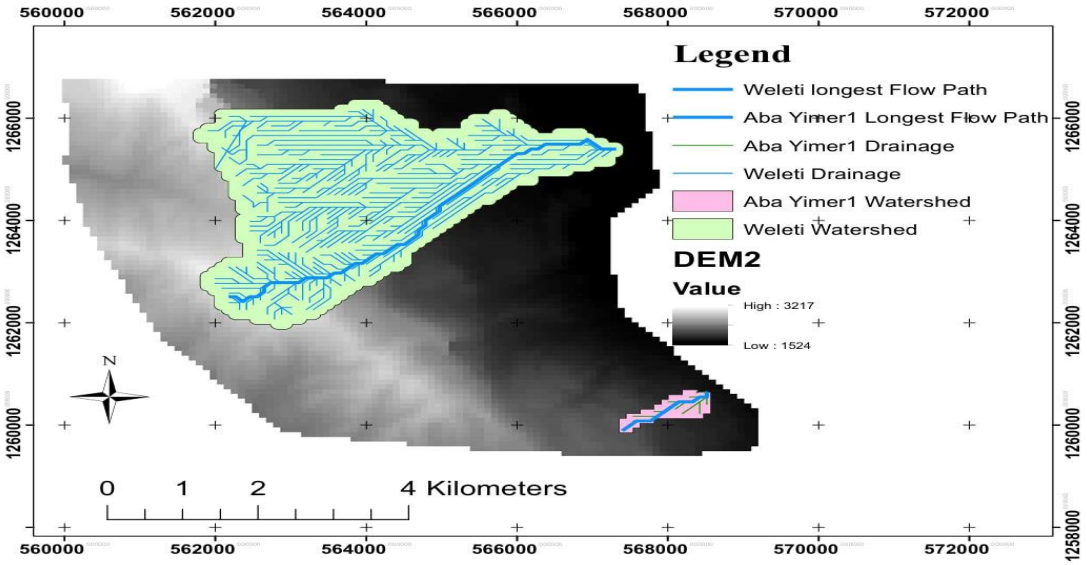

(a)

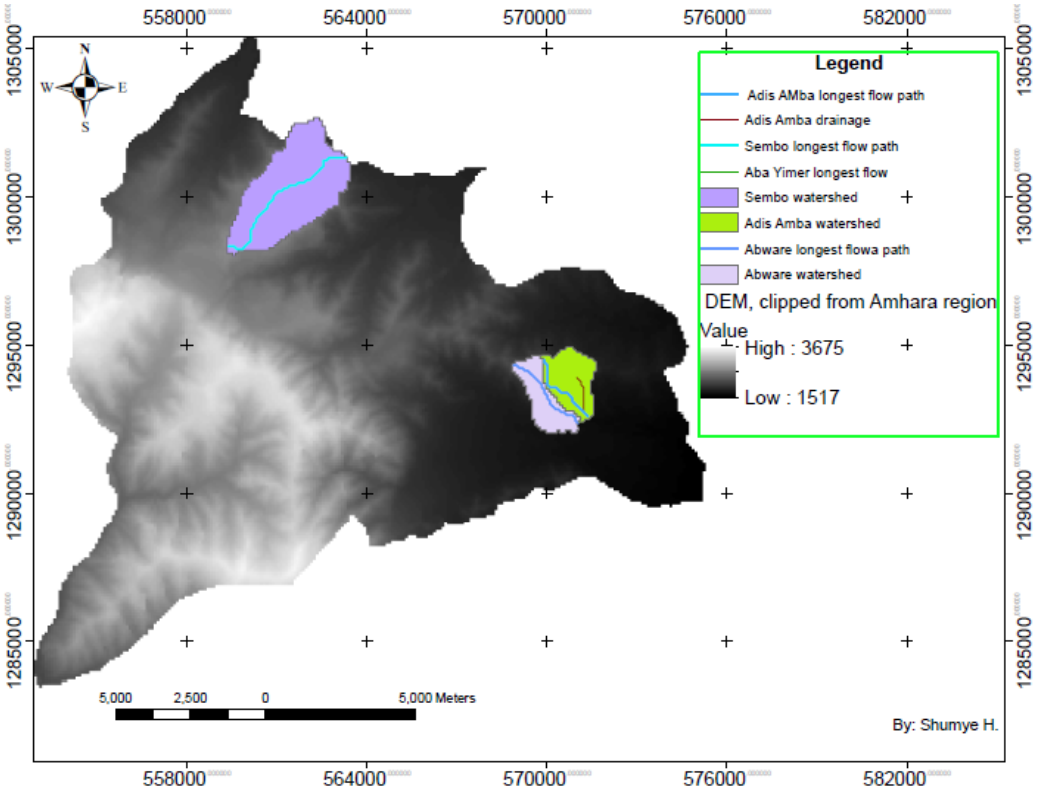

(b)

Figure 4: (a) Catchment boundary of Aba Yimer-1 and Weleti Bridges (b) Catchment boundary of Abware, Adis Amba and Sembo Bridges

2.4.3. Surveying Data

Detailed primary surveying data was collected for cross sections and slopes of rivers both downstream and upstream of the bridges and up to 130m-400m distance river center using total station. The slope of the riverbed (the riverbed profile) was generated using this data.

2.4.4. Riverbed Materials Data

Samples were collected from all five bridge locations, with two to three samples taken from the bed materials on the riverbed. This aimed to analyze the grain size distribution using sieve analysis after a physical inspection. Sample collections were done along the river course because this method provided a better grain size distribution in a uniform pattern. Based on the type and characteristics of the materials, samples were collected from a depth of 60 cm to 75 cm from the sandy riverbeds at Abware and Adis Amba. Samples were taken from the gravel river course at Aba Yimer-1 and Sembo at a depth of 75 cm to 100 cm. The collected materials were then mixed thoroughly and transported for laboratory analysis.

2.5 Methods

2.5.1 Scour Depth Estimation Equations

In this study, we selected six scour depth estimation equations for evaluation. These equations included: CSU, Bruisers, Jain and Fischer, Froehlich, HEC-18/Muller, and Laursen. We chose them because of their effectiveness in previous studies, current use in Ethiopia, and suitability for the selected stream characteristics.

Table 2: Summary of selected equations and their key features

Equations	Key features	Common use
CSU	Empirical, including correction factors	Standard in U.S design
Bruisers	Based on lab data for cylindrical piers	Experimental validation
Jain and Fischer	Includes sediment and flow intensity	Advanced modeling
Froehlich	Includes for pier shape and angle	Shape is sensitive design
HEC-18/Muller	Widely accepted	Regulatory compliance
Laursen	Oldest empirical model	Historical comparison

The selected equations are presented as follows.

1. Colorado State University (CSU) Equation (Richardson et al.,1975)

$$\frac{d_{se}}{b} = 2k_1k_2k_3\left(\frac{b}{y}\right)^{0.65} {F_r}^{0.43} \quad (1)$$

Where, d_{se} is the maximum scour depth in equilibrium condition, b is the pier width, y is flow depth, K_1 is a shape factor, K_2 is the alignment factor, K_3 is the correction factor for bed forms and F_r is Froude's number

2. Bruisers et al. (1977) Equation

$$\frac{d_{se}}{b} = 2\left(2\frac{U}{U_c} - 1\right) tanh\left(\frac{h}{b}\right) K_s k_\theta \quad (2)$$

$$U_c = 31.08\theta^{1/2}h^{1/6}{d_{50}}^{1/3} \quad (3)$$

Where d_{se} is the maximum scour depth in equilibrium condition, b is the pier width, U is the approaching flow velocity, U_c is the critical velocity for sediment motion in SI units, θ is the Shields mobility parameter, h is the approaching flow depth, K_s the pier shape factor and K_θ the pier alignment factor (Breusers et al., 1977).

3. Jain and Fischer (1979) Equation

$d_{se} = 1.84b\left(\frac{h}{b}\right)^{0.3} {F_{rc}}^{0.25}$, valid for F_r-F_{rc}<0. (4)

$d_{se} = 2.0b\left(\frac{h}{b}\right)^{0.5} (F_r - F_{rc})^{0.25}$, valid for F_r-F_{rc}> 0.2 in live-bed conditions (5)

Where, $Fr = \frac{U}{(gh)^{0.5}}$ and $F_{rc} = \frac{U_c}{(gh)^{0.5}}$ (6)

For this study, for 0<Fr-Frc<0.2, the largest value which was obtained from the above two equations has been taken.

4. Froehlich (1988) Equation (Landers and Mueller,1996)

$$d_{se} = 0.32\varphi Fr^{0.2}\left(\frac{b_e}{b}\right)^{0.62}\left(\frac{h}{b}\right)^{0.46}\left(\frac{b}{d_{50}}\right)^{0.08} + b \quad (7)$$

Where be(feet) is the width of the bridge pier projected orthogonally to the approach flow, φ (dimensionless coefficient based on the shape of the pier nose), d50 the median grain size (feet), b (feet) is pier width and Fr (Dimensionless) is the Froude Number directly upstream from the pier. The value of ϕ is different for different pier shape, ϕ = 1.3 for square nosed-piers, ϕ = 1.0 for round-nosed piers, ϕ = 0.7 for sharp-nosed piers.

5. HEC-18/ Mueller Equation

$$\frac{d_{se}}{b} = 2k_1k_2k_3k_4k_w\left(\frac{b}{h}\right)^{0.35}(Fr)^{0.43} \quad (8)$$

$K_w = 1.0\left(\frac{h}{b}\right)^{0.13}(Fr_1)^{0.25}$ For V/Vc>1 (9)

$K_w = 2.58\left(\frac{h}{b}\right)^{0.34}(Fr_1)^{0.65}$ For V/Vc<1 (10)

Where K_1, K_2, K_3, K_4 and K_w are correction factors accounting for pier nose shape, flow angle of attack, presence of bed forms, bed armoring and wide piers in shallow flows, respectively (Richardson and Davis, 2001).

6. Laursen (1960) Equation

$$\frac{y_2}{y_1} = \left(\frac{Q_2}{Q_1}\right)^{\frac{6}{7}}\left(\frac{W_1}{W_2}\right)^{K_1} \quad (11)$$

Where, y_2 is the average depth in the contracted section, y_1 is the average depth in the upstream main channel, Q_2 is the discharge through the contracted section, Q_1 is the discharge in the approach main channel, W_1 is the width of the main channel, W_2 is the width of the contracted section and the exponent K_1 is an empirical constant. Laursen (1956 and 1958) also developed an empirical formula to determine local scour around bridge piers that is given as follows.

$$D = 1.5B^{0.7}H^{0.3} \quad (12)$$

Where, D is scour depth measured from ambient bed elevation, in feet, B is width of the pier, in feet; and H is flow depth, in feet.

2.5.2 Hydrologic and Hydraulic Analysis

2.5.2.1 Hydrologic Analysis

Data Quality Test

Rainfall and flow data quality test was done prior to using for different analysis. Then, the data were checked for variance.

Design Discharge Estimation

Rational and SCS methods were used for this study. The Rational method is the best choice for estimating the design discharge (peak runoff) for areas up to 50 ha, while the SCS method is suitable for larger agricultural areas. The equation used by the Rational method is as follows (Chow et. Al.,1988; Haan et.al.,1994; Mays,2010).

$$Q = 0.00278\ CA \quad (13)$$

Where Q represents the design peak discharge (m^3sec-1); C is the runoff coefficient; I is rainfall intensity in mm/h for the design return period, over a duration equal to the "time of concentration" for the catchment, and A is the catchment area tributary to the design location in hectares.

The SCS method was developed by the US Soil Conservation Service. This method combines rainfall intensities with catchment parameters and uses a standard unit hydrograph to determine the distribution time of the runoff. The SCS method relies on the basic principles of the rainfall-runoff relationship, expressed in Eq. 14 (USDA,1972).

$$Q = \frac{(P-I_a)^2}{(P-I_a)+S} \quad (14)$$

Here, P is the maximum runoff potential (mm); Q is the actual runoff (mm); I_a is the initial abstraction (mm), and S is the maximum runoff potential difference. For this study, $I_a = 0.2S$ was used.

The runoff curve number (CN), soil type, land use, and antecedent soil moisture (infiltration rate) are important factors to consider with the SCS method. They significantly affect the runoff potential from a catchment. These values were taken from standard tables based on the catchment characteristics. The runoff (in volumetric units) calculated using the SCS method was then converted into design discharge by dividing the runoff volume by the time of concentration (Tc). To find T_c of the five river bridges catchment outlets, we used Kirpich's time of concentration formula (Kirpich,1940) given as:

$$Tc = \sum 0.948 \left\{ \left(\frac{{L_1}^3}{H_1} \right)^{0.385} + \left(\frac{{L_2}^3}{H_2} \right)^{0.385} + \cdots + \left(\frac{{L_n}^3}{H_n} \right)^{0.385} \right\} \quad (15)$$

Where Tc = time of concentration (hr.), L = length of overland flow (m) and H = elevation difference (m)

Return Period

In the present study, a 100-year return period for two bridges (Abware and Adis Amba) and a 50-year return period were applied for three culvert bridge structures (Aba Yimer-1, Sembo and Weleti). This ensures that the bridge can handle the flood event without significant damage or failure.

2.5.2.2 Hydraulic Analysis

For hydraulic and scour analysis, we surveyed river cross-sections and longitudinal profiles to gather key parameters such as flow area, wetted perimeter, hydraulic radius, and slope. We calculated roughness coefficients using Manning's equation. Additionally, we identified the mean grain size (D_{50}) of the bed material as a crucial input for scour calculations. The sampling protocol involved dividing the riverbed near each bridge into segments of similar material. We collected 2-3 sub-samples from each segment, mixed them, and tagged them for laboratory analysis. We took samples from various locations across the channel width to ensure horizontal representation while vertical variation was insignificant to determine the average grain size. We adjusted sampling depths based on the expected bed material. For the sandy Abware and Adis Amba rivers, we dug shallower pits (60–75 cm). For the anticipated gravel-bed rivers of

Aba Yimer-1, Weleti, and Sembo, we excavated deeper pits (75–100 cm), adjusting the exact depth based on our observations during the excavation.

The general conceptual framework of this study is depicted in Figure 5.

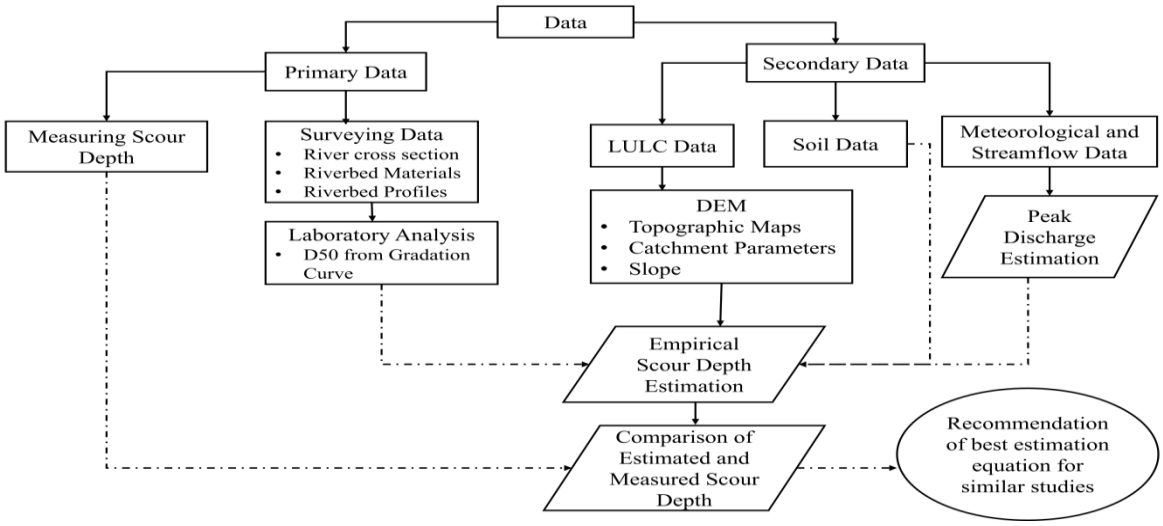

Figure 5. Conceptual framework of the present study

3. RESULTS AND DISCUSSION

3.1 Results of Hydrologic Analysis

The estimation of peak flood discharge was based on catchment area. The study used the Rational Method for areas smaller than 50 ha. For larger areas, it employed SCS Unit Hydrograph method. In this study, the Abware and Adis Amba bridges were analyzed with the Rational Method while the other bridges were assessed using the SCS method.

The hydrological parameters for Aba Yimer-1, shown in Table 3, include a time of concentration (T_c) of 0.14 hours, indicating a very quick runoff response. This is backed by a runoff coefficient (C) of 0.82, which is typical for a highly impervious catchment. A summary of the catchment parameters for each bridge site is available in Table 3.

Table 3: Catchment parameter and design peak discharge results for each bridge

Sl. No.	Bridge Name	Catchment area (ha)	CN-II	CN-III	C	T_c (hr)	Design discharge (m^3s^{-1})	Method
1	Aba Yimer-1	47.98	77.76	89.62	0.82	0.14	30.24	Rational
2	Weleti	1173.91	70.71	85.43	0.64	0.71	32.2	SCS
3	Abware	256.36	77.67	89.60	0.64	0.33	4.81	SCS
4	Adis Amba	255.72	81.47	91.88	0.77	0.31	7.62	SCS
5	Sembo	1031.54	80.10	89.98	0.75	0.45	8.1	SCS

3.2 Results of Hydraulic Analysis

3.2.1. Manning's roughness Coefficient

Considering the riverbed and bank materials in the study area, along with the roughness coefficient from the Ethiopian Road Authority (ERA) manual 2022, we estimated the roughness values (n). In this study, we used n = 0.04 for the cross sections of Aba Yimer, Weleti, and Sembo rivers while n = 0.03 was used for the cross sections of Abware and Adis Amba rivers.

3.2.2. River Cross-section and Riverbed Profile Parameters

Using the coordinates of lateral distance, ground elevation and river center data, the river cross sections and riverbed profiles were generated to determine the hydraulic parameters such as flow area, wetted perimeter, hydraulic radius, and the bed slope (Figure 6). The riverbed slope of the selected bridges depicted steepest slope in each riverbed profile along the river breadth (Figure 7). From the stage discharge curves (Figure 8), the approaching flow depth of each river for the return periods was determined as follows:

Aba Yimer-1: y_{50} = 0.61m for Q_{P50} = 30.24 m^3s^{-1}

Weleti River: y_{50} = 0.82 m for Q_{P50} = 32.2 m^3s^{-1}

Abware River: y_{100} = 0.55m for Q_{P100} = 4.81 m^3s^{-1}

Adis Amba River: y_{100} = 1.02 m for Q_{P100} = 7.62 m^3s^{-1}

Sembo River: y_{50} = 0.54 m for Q_{P50} = 8.10 m^3s^{-1}

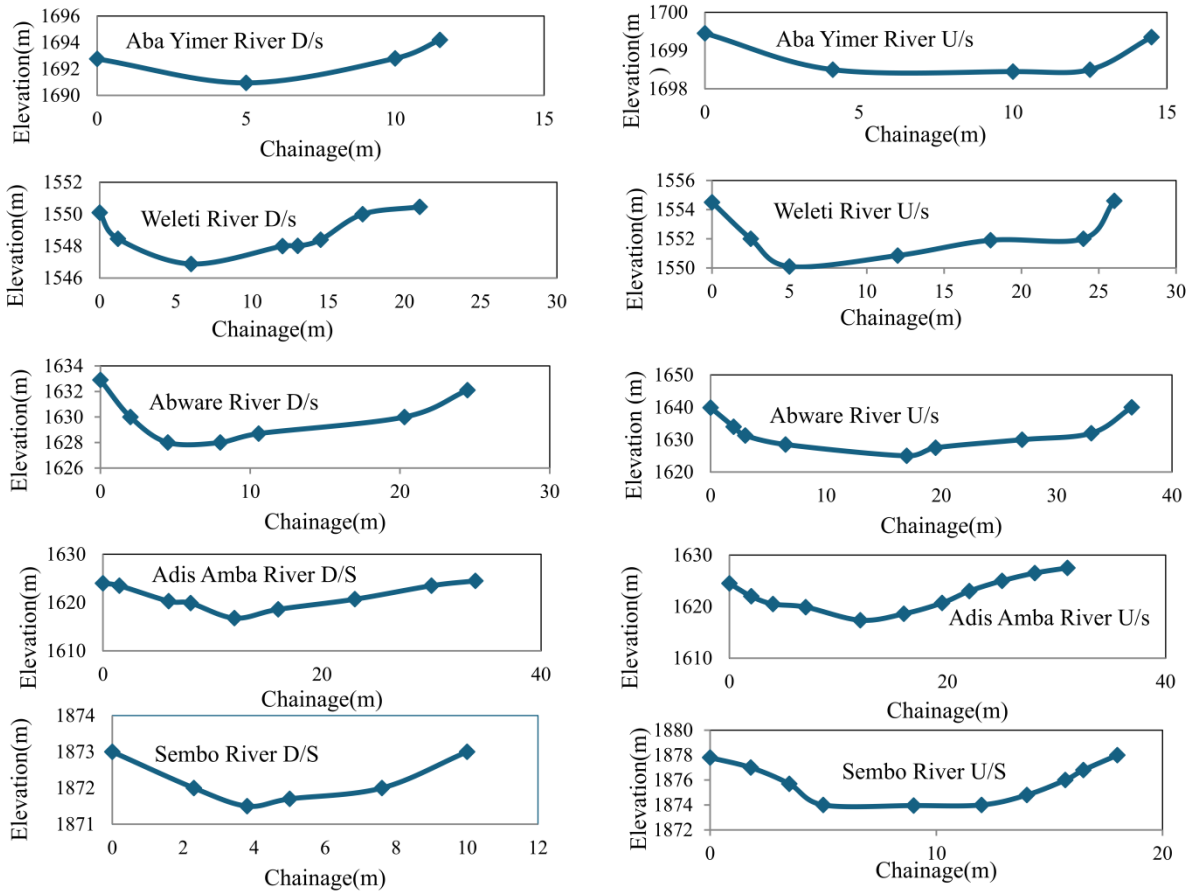

Figure 6. U/s and D/s River Cross Sections (from left bank to the right bank)

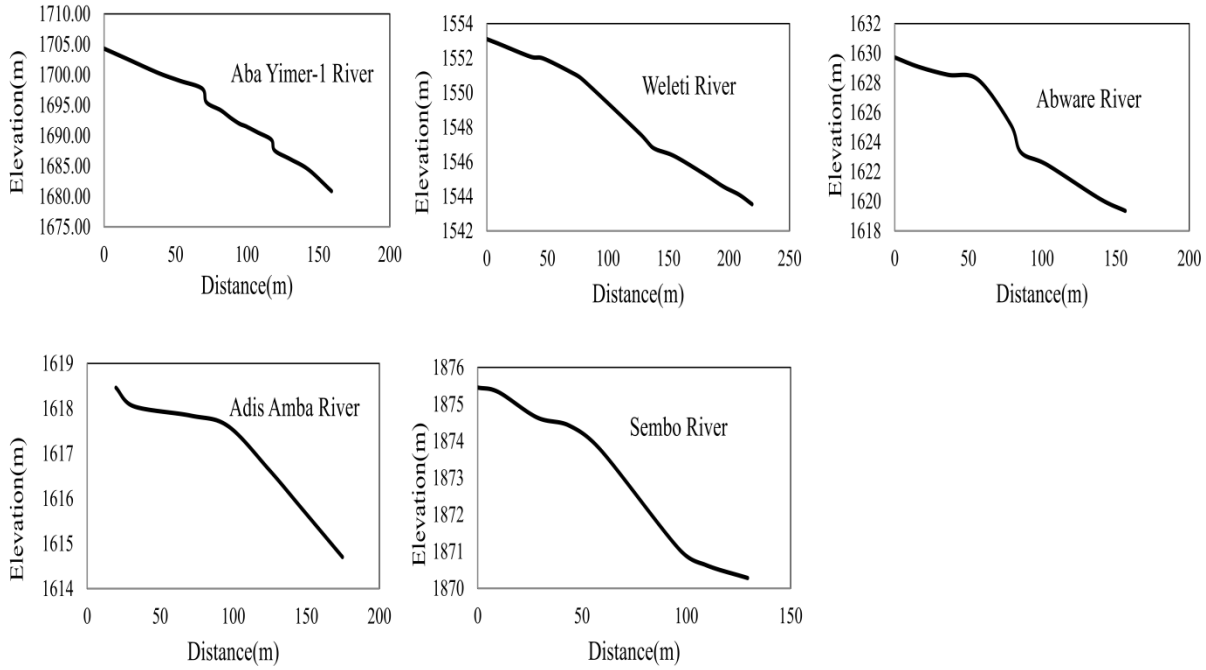

Figure 7. Riverbed profiles at each river

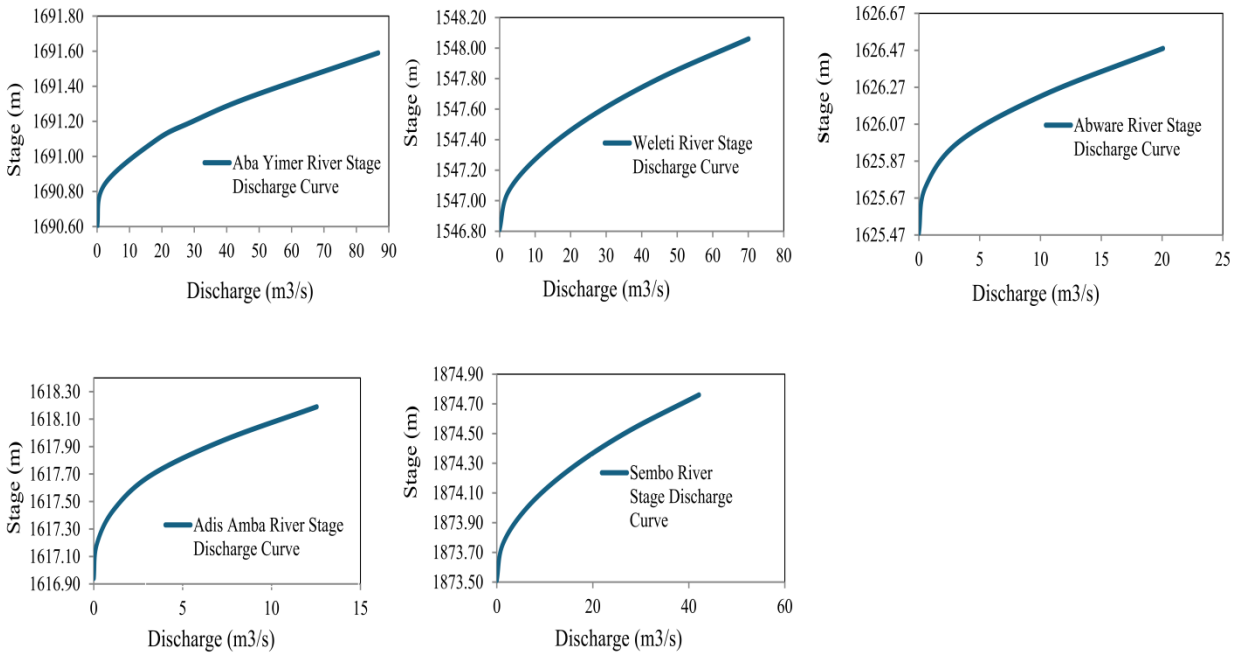

Figure 8. Stage Discharge Curve of the rivers

3.2.3. Laboratory Analysis of Average Grain Size

We developed a laboratory analysis of average grain size (gradation curve) based on the results from the percentage of finer and retained amounts at different sieves. We determined the average particle size, or D_{50} (mm), from the gradation curves of each riverbed material (Figure 9). The D_{50} size and bed material classification analysis was done in a laboratory and summarized in Table 4.

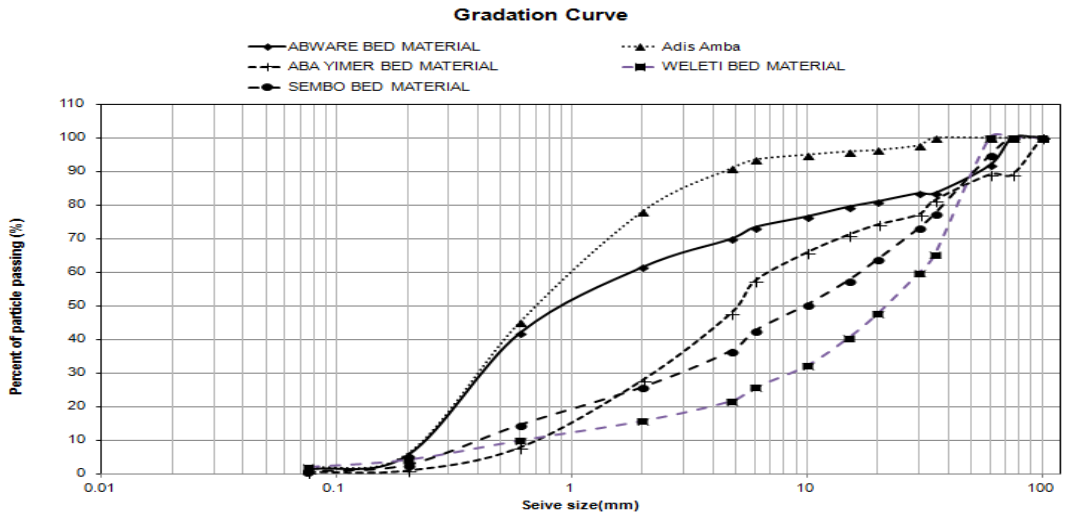

Figure 9. Gradation curves of the five rivers bed material

Table 4: D50 riverbed material classification

Sl. No.	Name of bridge	Median bed material diameter, D_{50} (mm)	Classification based on USCS
1	Aba Yimer	5	Gravel bed
2	Weleti	24	Gravel bed
3	Abware	0.91	Sand bed
4	Adis Amba	0.68	Sand bed
5	Sembo	9.1	Gravel bed

3.3 Scour Components and Bridge-Specific Observations

The total scour depth was assessed by considering three primary components: general scour, contraction scour, and local scour (Wang et al., 2019). In the present study, local scour was considered while other scour mechanisms were found negligible at the study locations. The key variables used in the scour analysis are summarized in Table 5. The correction factors K_1 (for pier nose shape) and K_2 (for flow attack angle) were obtained from ERA design manual, which provided standardized values for these coefficients based on various angles of attack (ranging from 0° to 30°) and different pier nose shapes (circular, rectangular, or sharp-nosed). These coefficients were essential for accurate local scour depth calculations as they accounted for the hydrodynamic effects of pier geometry and flow alignment. The recommended values of ERA manual were applied consistently across all bridge sites to maintain methodological uniformity in the scour predictions.

Table 5: Scour Variables Analysis

Sl. No	Name of the bridge	Shape of pier nose	Angle of attack (degrees)	K_1	Width normal to flow b (m)	Measured scour depth (m)	D_{50} (mm)	length L (m)	L/b	K_2
1	Aba Yimer	square	30	1.1	2.4	1.49	5	11.1	4.6	2
2	Weleti	square	0	1.1	0.6	1.12	24	32.56	54.3	1
3	Abware	square	0	1.1	2	4.89	0.91	9.7	4.9	1
4	Adis Amba	round	0	1	1.25	6.03	0.68	2.5	2.0	1
5	Sembo	square	0	1.1	3.5	2.15	9.1	9.7	2.8	1

All rivers in this study exhibited no aggradation but displayed significant downstream degradation. The degradation depth was calculated based on upstream river slope, design elevation, and current scour point elevation (Table 6). During high-flow conditions, the natural width of the rivers at the Aba Yimer-1, Weleti, Abware, and Adis Amba bridges exceeded the constructed waterway length designed for flood events. Except for Aba Yimer-1 Bridge, the

other three bridges featured concrete beds along their longitudinal sections, preventing flow constriction and minimizing scour risk. The Sembo Bridge experienced constriction during peak floods, but its concrete floor at the contracted section mitigated scour effects. Field observations confirmed no significant contraction scour at any of the bridges studied. Instead, local scour was identified as a dominant contributor to total scour depth across all five bridges.

Scour depths were computed for 50 and 100-year return periods using multiple empirical formulas. A detailed result was provided in Tables 6-12. Additionally, Table 13 presents the average bridge scour depth for 50-year return period, comparing predictions from six different methods.

Table 6: Gradual degradation depth for different bridges

Sl. No..	Name of bridge	Slope	U/s elevation (m)	Distance (m)	Design elevation at point of scouring (m)	Current elevation at point of scouring (m)	Degradation depth (m)
1	Aba Yimer-1	0.153	1692.1	5	1691.3	1690.59	0.7
2	Weleti	0.066	1547.93	5	1547.6	1546.81	0.8
3	Abware	0.021	1630.37	5	1630.3	1625.48	4.8
4	Adis Amba	0.039	1622.97	5	1622.8	1616.94	5.8
5	Sembo	0.029	1875.66	5	1875.5	1873.51	2.0

Table 7: Local scour for design return period using CSU equation

Sl. No.	Name of bridge	K_1	K_2	K_3	b (m)	y(m)	Q(m^3/s)	A(m^2)	V(m/s)	F_r	d_{se} (m)
1	Aba Yimer-1	1.1	2	1	2.4	0.61	30.24	5.58	5.42	2.22	15.089
2	Weleti	1.1	1	1	0.6	0.82	32.2	8.08	3.99	1.41	2.08
3	Abware	1.1	1	1	2	0.55	4.81	1.58	3.04	1.31	5.71
4	Adis Amba	1	1	1	1.25	1.02	7.62	2.32	3.28	1.04	2.32
		1	1	1	1.25	0.84	4.12	1.46	2.82	0.98	2.57
5	Sembo	1.1	1	1	3.5	0.54	8.1	2.8	2.89	1.26	8.18
		1.1	1	1	3.5	0.37	3.86	1.55	2.49	1.3	10.64

Table 8: Local scour for design return period using Breusers equation

Sl. No	Bridge Name	D_{50} (m)	Θs (m)	H (m)	B (m)	Ks	Kθ	Uc (m/s)	U (m/s)	Tanh (h/b)	d_{se} (m)
1	Aba Yimer-1	0.0022	3.23E-02	0.61	2.4	1.1	2	0.945	5.42	0.25	27.51
2	Weleti	0.024	4.70E-02	0.82	0.6	1.1	1	1.88	3.99	0.88	3.75
3	Abware	0.0009	2.77E-02	0.55	2	1.1	1	0.454	3.04	0.27	14.7
4	Adis Amba	0.0007	3.13E-02	1.02	1.25	1	1	0.485	3.28	0.67	21.11
5	Sembo	0.0091	4.14E-02	0.54	3.5	1.1	1	1.191	2.89	0.15	4.55

Table 9: Local scour for design return period using Jain & Fischer live-bed equation

Sl. No.	Name of bridge	h(m)	b(m)	d_{50} (m)	u(m/s)	uc (m/s)	F_r	F_{rc}	F_r-F_{rc}	d_{se}(m)
1	Aba Yimer	0.61	2.4	0.0022	5.42	0.67	2.22	0.27	1.94	2.86
2	Weleti	0.82	0.6	0.024	3.99	1.88	1.41	0.66	0.74	1.30
3	Abware	0.55	2	0.00091	3.04	0.45	1.31	0.20	1.11	2.16
4	Adis Amba	1.02	1.25	0.00068	3.28	0.48	1.04	0.15	0.89	2.19
5	Sembo	0.54	3.5	0.0091	2.89	1.19	1.26	0.52	0.74	2.55

Table 10: Local scour for design return period using Froehlich design equation

Sl. No	Bridge name	Pier Shape	F_r	Ø	b (m)	be (m)	h (m)	d50 (m)	d_{se} (m)
1	Aba Yimer	square	2.22	1.3	0.67	0.20	0.05	0.016	8.042
2	Weleti	square	1.41	1.3	0.05	0.05	0.07	0.079	0.803
3	Abware	square	1.31	1.3	0.59	0.17	0.05	0.003	7.141
4	Adis Amba	Round	1.04	1	0.10	0.10	0.09	0.002	1.414
5	Sembo	square	1.26	1.3	0.83	0.29	0.04	0.03	10.036

Table 11: Local scour for design return period using HEC-18/Mueller equation

Sl. No.	Name of bridge	K_1	K_2	K_3	K_w	b(m)	h(m)	V (m/s)	F_r	d_{se} (m)
1	Aba Yimer	1.1	2	1.1	0.42	2.4	0.61	5.42	2.22	11.01
2	Weleti	1.1	1	1.1	1.36	0.6	0.82	3.99	1.41	2.51
3	Abware	1.1	1	1.1	0.28	2	0.55	3.04	1.31	4.27
4	Adis Amba	1	1	1.1	0.82	1.25	1.02	3.28	1.04	2.4
	Sembo	1.1	1	1.1	0.15	3.5	0.54	2.89	1.26	5.14

Table 12: Local scour for current age of each bridge and design return period using Lauren's equation

Sl. No.	Name of bridge	B (m)	H (m)	D (m)	D (m)
1	Aba Yimer	0.67	0.05	0.46	5.55
2	Weleti	0.05	0.07	0.08	0.99
		0.59	0.05	0.41	4.95
3	Abware	0.59	0.03	0.36	4.33
		0.10	0.07	0.12	1.66
5	Sembo	0.83	0.04	0.52	6.25

Table 13: Average bridge scour depth for return period of 50 years

Sl,No.	Name of bridge	CSU	Froehlich	Brueisers	HEC-18	Lauren	Jain & Fischer
1	Aba Yimer-1	15.09	8.04	27.51	11.01	5.55	2.86
2	Weleti	2.08	0.80	3.75	2.51	0.99	1.30
3	Abware	5.71	7.14	14.70	4.27	4.95	2.16
4	Adis Amba	2.32	1.41	21.11	2.40	1.76	2.19
5	Sembo	8.18	10.04	4.55	5.14	6.25	2.55

3.4 Comparison of Measured and Estimated Scour Depths

The evaluation of scour depth prediction equations was conducted by comparing computed scour depths with field-measured values at various bridge sites (Figure 6). A composite comparison further validated the performance of these equations. The analysis revealed that the Jain & Fischer equation outperformed others, providing the closest estimates for both gravel-bed and sand-bed rivers. Specifically, it yielded the most accurate scour predictions for two gravel-bed and one sand-bed river. Following Jain & Fischer (1979), Laursen's equation demonstrated reasonable accuracy, particularly for two sand-bed and two gravel-bed rivers. Meanwhile, Froehlich's equation performed well with smaller pier widths. normal to the flow. Moreover, it could produce the best-fit scour estimates for certain bridges with comparable pier dimensions.

The study indicated that most equations were highly sensitive to pier width and sediment grain size (D_{50}). However, the CSU and Laursen's equations were less influenced by these factors. Additionally, hydraulic parameters such as Manning's roughness coefficient (n), cross-sectional area of the river, and flow velocity were found to significantly affect scour depth magnitude. This suggests the importance of precise input data in scour modeling as variations

in these parameters can lead to substantial discrepancies in scour predictions. Given these findings, Jain & Fischer's equation is recommended as the primary choice for local scour estimation in both gravel and sand-bed rivers. However, Laursen's and Froehlich's equations can serve as reliable alternatives, depending on site-specific conditions such as pier geometry and sediment characteristics. Engineers should exercise caution when selecting input parameters particularly pier width and grain size to ensure accurate scour depth predictions in bridge design. Though empirical scour equations provide useful estimates, their performance varies with hydraulic and structural conditions. A thorough understanding of parameter sensitivity is essential for optimizing scour depth calculations and ensuring the safety and stability of bridge foundations.

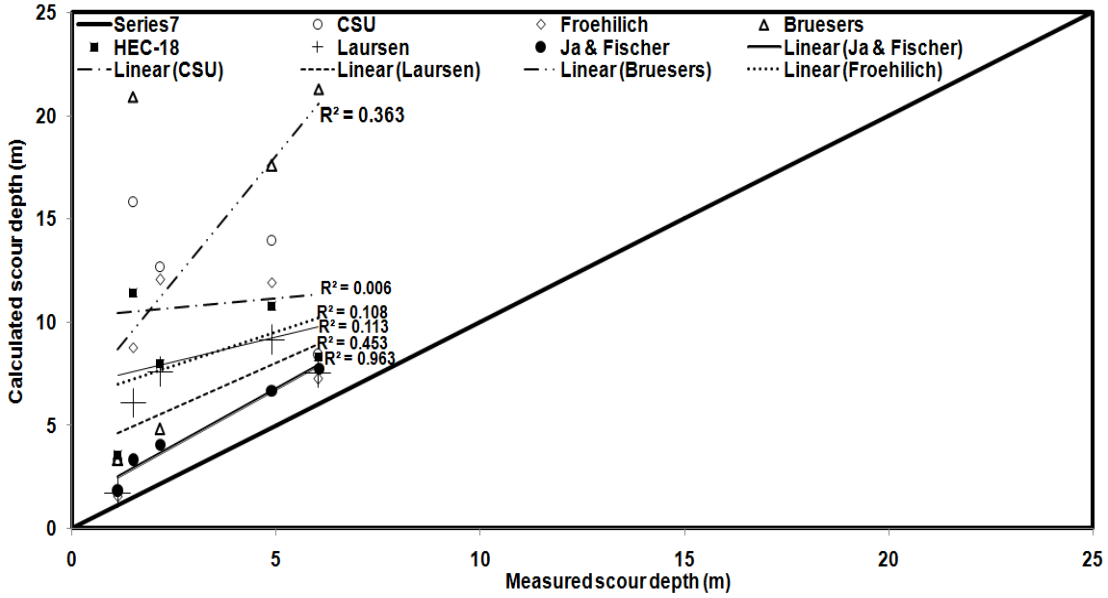

Figure 6. Performance comparison with regression equations

4. CONCLUSION

In this study, local scour depth estimation was considered using various empirical equations. Additionally, long-term degradation, contraction scour and local scour are estimated to calculate the total scour. Contraction scour hardly existed for all the selected bridge sites owing to sufficiently provided length of water way. Besides, there were no flow constrictions for all the selected bridges. Scour depth for selected bridges was measured and then the total scour was compared with the measured scour depths. From the comparative analysis, Jain & Fischer and Laursen & Froehlich equations estimated scour depth with better magnitudes in approaching the measured scour depths. Hence, bridge scour designers preferred to use Jain & Fischer equation to determine local scour as their leading choice for sand bed and gravel bed

rivers. The scour variables such as pier width, shape, and alignment were found sensitive to scour magnitude and any changes to the magnitudes of these parameters significantly changes the value of scour depth. Hence, deciding and measuring these parameters should be done carefully while designing the equilibrium scour depth.

Conflict of Interest

The authors declared that no conflict of interest.

REFERENCES

Annandale, G. W. (2000). Prediction of Scour at Bridge Pier Foundations Founded on Rock and Other Earth Materials. Transportation Research Record, 1696(1), 67-70. https://doi.org/10.3141/1696-45

Bruisers, H. N. C., Nicollet, G., & Shen, H. W. (1977). Local scour around cylindrical piers. Journal of hydraulic research, 15(3), 211-252.

Chow V., Maidment D., and Mays L. 1988, Applied Hydrology. New York: McGraw hill Internationl Edition

Ebrahimi M., Kahraman R., Riella M., Kripakaran P., Djordjevic S., Tabor G., Prodanovic D. and Arthur S. 2018, Experimental Investigation of Scour and Pressures on a Single Span Arch Bridge Under Inundation. 7th IAHR International Symposium on Hydraulic Structures.

Ebtehaj I., Sattar A. M. A., Bonakdari H, Zaji A.H. 2017, Prediction of scour depth around bridge piers using self-adaptive extreme learning machine, Journal of Hydroinformatics, 19 (2), 207–224

Ebtehaj, I. Bonakdari, H. Shamshirband, S. Mohammadi, K. 2016, A combined support vector machine-wavelet transform model for prediction of sediment transport in sewer, Flow Measurement and Instrumentation 47, 19–27

Ethiopian Roads Authority, ERA, 2013, Drainage design manual, Ethiopian road authority. Adis Aababa, Ethiopia

Froehlich, D. C. (1988). Local scour at bridge piers. Hydraulic Engineering Report No. HL-88-3, Department of Civil Engineering, University of Houston, Houston, TX.

Garg K. 2006, Water Resources Engineering, Vol-II, Irrigation engineering and hydraulics Structures, 35th Edition, Khanna Publishers, New Delhi

Ghani A. Nalluri C A. 1996, Development of pier scour equations. In: 10th Congress of Asian-Pacific Division of International Association for Hydraulic Research, Langkawi, Malaysia, 295-302

Ghazvinei T., Mohamed A., Ghazali H., HuatPezhman K., 2012, Scour hazard assessment and bridge abutment instability analysis, Electronic Journal of Geotechnical Engineering, 17, 2213-2224

Gilja G., Mari M., 2018, Calculation of local scour at bridges over large Croatian river, Geophysical Research abstracts, EGU, Vol. 21

Girma, N. T. (2018). Local scour at bridge piers: The case of failure of Kulfo River Bridge at Arba Minch, Southern Ethiopia. Ethiopian Journal of Water Science and Technology, 1 (1), 76–85.

Haan, C. T., Barfield, B. J., & Hayes, J. C. (1994). Design hydrology and sedimentology for small catchments. Academic Press.

Jain, S. C., & Fischer, E. (1979). Scour at bridge piers. Journal of Hydraulic Division, American Society of Civil Engineers (ASCE), 105(3), 229–241.
Kafi M. Alam J. 1995, Modification of local scour equations, Journal of Institution of Engineers (India), 76, 25-29
Kirpich, Z. P. (1940). Time of concentration of small agricultural watersheds. Civil Engineering, 10(6), 362–364.
Kothyari U., 2007, Indian practice on estimation of scour around bridge piers - A comment, Sadhana, 32 (3), 187-197
Landers, M. N., & Mueller, D. S. (1996). Evaluation of Selected Pier-Scour Equations Using Field Data. Transportation Research Record, 1523(1), 186-195. https://doi.org/10.1177/0361198196152300123
Laursen, E. M. (1960). Local scour at bridge crossings. Bulletin No. 28, Iowa Institute of Hydraulic Research, University of Iowa, Iowa City, IA.
Mays, L. W. (2010). Urban water supply handbook. McGraw-Hill.
Richardson, E. V., Simons, D. B., Karaki, S., Mahmood, K., & Stevens, M. A. (1975). Highways in the river environment: Hydraulic and environmental design considerations (Training and Design Manual, FHWA-NHI-76-N005). Federal Highway Administration, U.S. Department of Transportation.
Sarlak N and Tigrek S., 2011, Analysis of experimental data sets for local scour depth around bridge abutments using artificial neural networks, Water SA, 37 (4), 595-602
Sheppard A., Melville M., & and Demir M., 2014, Evaluation of Existing Equations for Local Scour at Bridge Piers. Journal of hydraulic engineering, 140 (1), 14-23
Shukri M. 2017, Experimental Study of Local Scour Depth around Cylindrical Bridge Pier, International Journal of Civil and Environmental Engineering 11(1), 31-36
Tamalew C., and Abdella K. 2016, Estimation of Discharge for Ungauged Catchments Using Rainfall-Runoff Model in Didessa Sub-Basin: The Case of Blue Nile River Basin, Ethiopia. International Journal of Innovations In Engineering Research and Technology, 3 (9), 62-72
Temesgen B., G/mariam B., Ayele G. and Solomon S. 2015, Investigating Highway Drainage Problems in the Sile River Bridge, South, Ethiopia. Journal of Multidisciplinary Engineering Science and Technology, 2 (4), 515-526
USDA-SCS. (1972). National engineering handbook: Section 4, Hydrology. U.S. Department of Agriculture, Soil Conservation Service.
Vonkeman V. and Basson G. 2018, Evaluation of empirical equations to predict bridge pier scour in a non-cohesive bed under clear-water conditions, Journal of the South African Institution of Civil Engineers, 61(2), 1-20
Wang Z.W. 2010, Experimental study on scour rate and river bed inertia, Journal of Hydraulic Research, 49 (3), 17-37
Wang, Z., Li, Z., & Zhang, L. (2019). Experimental study of local scour around side-by-side bridge piers under ice-covered flow conditions. Cold Regions Science and Technology, 165, 102847. https://doi.org/10.1016/j.coldregions.2019.102847
Yahaya A. S. and Ghani A. 1999 Comparing bridge pier scour equations using statistical techniques. In: Proceedings of the World Engineering Congress (WEC99), Kuala Lumpur, Malaysia, 63–66
Yahaya A. S., Ghani A. and Azazi Z.N. 2002, Modelling bridge pier scour equations using regression methods. Borneo Science Journal 2, 23–32
Yanmaz M. and Calamak A. 2016, Evaluation of Scour Risk at Foundations of River Bridges; Teknik Dergi, Technical Journal of Turkish Chamber of Civil Engineers, 27(3), 7533-7549

Zaid M., Yazdanfar Z., Chowdhury H., Alam F. 2019, A review on the methods used to reduce the scouring effect of bridge pier, Energy Procedia, 160, 45-50

Ethiopian Journal of Water Science and Technology (EJWST)

DOI: https://doi.org/10.59122/20519g6

Vol. 7 , 2024, Pages: 77~107 ISSN(Print): 2220-7643

Morphodynamic Alterations and Scour Processes around Bridge Openings: A Case Study of Selected Bridges on the Sodo-Konso Highway, Ethiopia

Aklilu Alemayehu Kassaye [a, *], Mesele Markos Forsido[a]

[a]Arba Minch University, Arba Minch Water Technology Institute, Arba Minch, Ethiopia; MMF (mesele.markos@amu.edu.et);

[*]Corresponding author: aklilu.alemayehu@amu.edu.et; ORCiD Id: 0000-0002-0202-7587;

Abstract

Numerous bridges in southern Ethiopia are greatly affected by morphodynamic changes in the alluvial channels caused by hydraulic responses to flow depth, velocity, shear stress and longitudinal slope. These bridges are vital for enabling traffic flows between communities in the region. In this study, morphodynamic alterations around bridge openings were conducted using the hydraulic flow parameters based on field and laboratory investigations conducted in selected bridge sites between the Sodo and Konso highway routes.The morphodynamic analysis of 1984 to 2021, 1,276 Landsat images of 5 selected scour susceptible bridge sites have been analyzed using RivMap toolbox in MATLAB after rapid assessment of the channel stability of 15 bridges based on the field observation. The 38 years of channel geomorphological changes showed that lateral widening of the alluvial valley was dominant at the selected bridge sites. The widening of the channel worsened the contraction, increased the potential for local scour, and raised flow velocity caused by the narrow bridge opening. Results from the HEC RAS (Hydrologic Engineering Center River Analysis System) showed that three of the studied bridges—Kulfo, Alge, and Wajifo had a low risk of scour, while the Sile and Sego bridges faced the most severe scour risks. In particular, Sego Bridge was highly vulnerable during floods with 50, 100, and 500-year return periods due to the extreme narrowing of the valley at the bridge location and ongoing lateral widening of the upstream floodplain channel over time. This suggests that Sego Bridge requires a new relief culvert or other countermeasures to safely manage extreme flooding. Thus, design and analysis of the bridge structures in the lower alluvial reaches of the rivers require a thorough investigation of the geomorphology and provision of adequate openings for the potential floodplain widening.

Keywords: *bridge scour, morphodynamic, HEC RAS, contraction scour, local scour*

Received: 05 August, 2024; Accepted 10 September, 2024 Published: December, 2024

1. INTRDUCTION

Spatial and temporal morphodynamics of the alluvial river channel lateral migration is a widely documented concept in many studies (Li et al., 2017; Boothroyd et al., 2020; Li et al., 2020). Rapid lateral widening highly threatens riparian land property and hydraulic structures near the reach (Boothroyd et al., 2020). Natural and human-induced factors for channel geomorphic changes were reported in several case studies (Beyene et al., 2023). Some of the recent works revealed reach scale thalweg migration (Li et al., 2017), catchment scale multi-temporal annually resolved satellite images of active channel masking (Boothroyd et al., 2020), GIS-based channel platform analysis (Mandarino et al., 2019),watercourse constriction based morphological patterns (Oliveto & Marino, 2019) and in-stream sand mining influence based on morphodynamic alterations (Lade et al., 2019).

Understanding the evolution of the channel platform is essential for effective engineering planning, as it provides insights into long-term morphological changes, sediment transport patterns, and areas prone to erosion or deposition. This knowledge supports the design of resilient infrastructure and the mitigation of risks associated with channel instability.

Bridges are infrastructures used to connect two shores of the rivers to enhance traffic flow. However, these structures affect the natural water flow, and their stability is also impacted by the scouring (Liao et al., 2018). Scour depth prediction is a significant bridge design phenomenon (Chavan & Kumar, 2018). Experimental and numerical studies to estimate scour depth based on water surface, flow velocity, and bed shear stress are used to simulate 3D scour processes (Omara et al., 2019).

Studies on Nonuniform sand beds, pier groups, flood-season scour patterns, scour hole evolution, pier modifications, compound channel abutment scour, clear water scour, complex flow field scour, and eddy simulations (Chavan & Kumar, 2018; Zhou et al., 2020; (Tabarestani & Zarrati, 2016; Khan et al., 2017; (Poggi & Kudryavtseva, 2019; Farooq & Ghumman, 2019; Ghazvinei et al., 2016; Guillermo et al., 2013; Ettema et al., 2017 ; Kirkil et al., 2009) , monitoring of temporal and spatial evolution of scour hole around bridge shows that the focus of the most cases was attempting to determine the scour depth at particular condition.

Numerous studies have been carried out on river reach morphodynamics (Church, 2006; Lade et al., 2019; Boothroyd et al., 2020). In other words, most of the bridge scour analysis-related works revealed that experimental pier and abutment scour depth determination to evaluate counter-measurement protection mechanisms (Kumcu et al., 2014; Xiong et al., 2017). The lateral migration of the channel through time induced a significant change in the flow direction (angle of attack), velocity, and bed shear stress (Omara et al., 2019). Actual field-based channel evolution geomorphologic analysis-related scour determination research work is very scanty. Scouring around bridge foundations was the most significant contributing factor to bridge failures. The scour failures tended to occur without prior warning and led to fatalities and economic loss (Wang et al., 2017).

Degradation or/and aggradation of the river bed and bank materials as well as contraction and local scour conditions were critical factors of the service life of the bridge. Reasonable and prudent hydraulic analysis of a bridge design required an assessment of the proposed bridge's vulnerability to potential scour. The hydraulic performance of the existing bridges depended on the estimation, monitoring, and countermeasures (Wang et al., 2017) related to counterbalance flow complications occurring due to the construction of the structure. Identifying and modeling of these effects would sophisticate the maintenance and operation of the bridge, including probable repair, reconstruction, and potential liability. Bridge failure could be caused by foundation, structural, and hydraulic failures, but the majority of bridge failures were due to hydraulic conditions. Pier scour was the major possible cause of hydraulic failures (Farooq & Ghumman, 2019) of a bridge, particularly in alluvial channels where the riverbed and banks were under continuous modification. Local scour could be a complicated phenomenon owing to three-dimensional flow separation on the upstream side of the bridge pier and sediment load transport (Tabarestani & Zarrati, 2016). Lots of research works have been done on this topic to derive the relationship between the maximum depths of scour, and understand the mechanism of local scour and its control. Therefore, a large amount of research work is available on the topic of bridge scour and its protection. However, only a few studies are available so far on the flow field around the bridge elements.

Because of the hazard and economic hardships posed by a rapid bridge collapse, special considerations should be given to select appropriate flood magnitudes for use in the analysis. The inherent complexities of stream stability, further complicated by highway stream crossings,

required a multilevel solution procedure. The evaluation of a highway stream crossing or encroachment should begin with a qualitative assessment of stream stability(FHWA, 2009). This might involve the application of geomorphic concepts to identify potential problems and alternative solutions. This analysis should be followed by quantitative analysis using basic hydrologic, hydraulic, and sediment transport engineering concepts. Such analysis could include an evaluation of flood history, channel hydraulic conditions, and basic sediment transport analysis such as evaluation of catchment area sediment yield, incipient motion analysis, and scour calculations. This analysis would be adequate for many locations if the problems and the relationships between different factors affecting stability were adequately explained. Otherwise, a more complex quantitative analysis based on detailed mathematical modeling and/or physical hydraulic models should be considered.

Problems associated with aggradation can be particularly hazardous, especially in areas with limited freeboard. In such cases, increased flood risks such as more frequent overtopping may pose threats to upstream properties and public safety. Therefore, when aggradation is anticipated, it is important to assess these potential consequences. In addition, aggradation in a stream may serve to moderate potential scour depths (FHWA, 2012).

The highway from Sodo to Konso is a part of socio-economically significant main federal transport route to the South Ethiopia. There are multiple bridges designed to cross perennial and non-perennial river valleys. In some of the rivers, more than one bridge structures were constructed (three adjacent bridges on the Sile River) within a short distance apart from the existing one due to the failure of the former crossing. As witnessed from the failure of the existing bridges, hydraulic failure seems to be dominant. It needs to be analyzed to identify and mitigate this effect for maintenance and possible adjustments of the conditions for the new design. This study will focus on investigating morphodynamic alterations around bridge openings and openings in the process of scouring under the influence of hydraulic flow parameters for the selected bridges. The specific aims of the present study are to (1) investigate the contraction scour potential; (2) identify the major hydraulic factors for the failure of bridges; and (3) evaluate the remedial alternatives for the scour problem.

In this study, the subsequent section is structured as materials and methods (rapid assessment of channel stability, morphodynamic analysis by using RIVMAP tools in google earth engine, and hydraulic and geotechnical laboratory test, and run HEC-RAS software to plot scour prism) results on alluvial channel migration pre-entire reach and commutative migration rate per annual, discusses the implications of contraction and local scouring of abutment and pier and proposes mitigation strategies with a final conclusion(key findings and recommendations for future research).

2. MATERIALS AND METHODOLOGY

2.1 Description of the study

The highway from Sodo to Konso is located in the South Ethiopia regional state as shown in Figure 1.

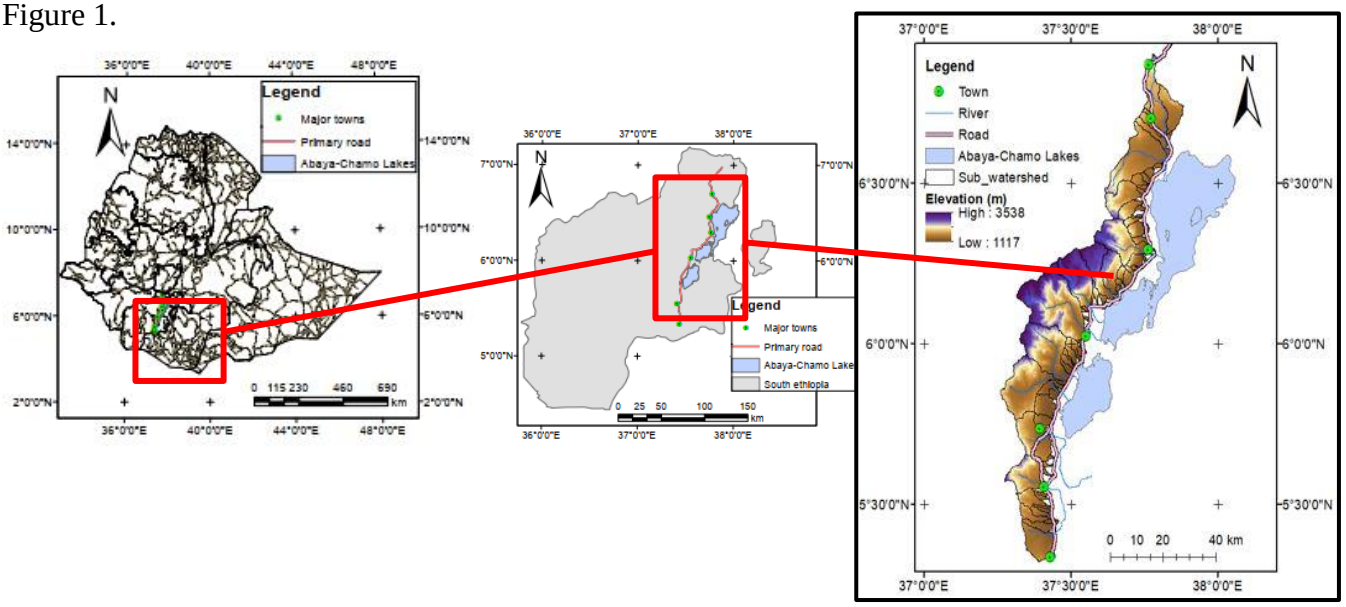

Figure 1. Location of the study area

2.2 The Nature of Rivers

Rivers crossing this highway route are located in the Rift Valley Lakes basin with perennial and ephemeral characteristics. Most of the bridges were constructed across the lower reaches of the ephemeral stream valleys and encountered continuous upstream land use changes and human

interactions which can result in long-term degradation or aggradation and lateral widening of the valley.

2.3 Reach Type and Morphology River

The bridge structures on the Sodo to Konso highway are mostly constructed in the alluvial reaches of the rivers, predominantly characterized by the erosion and deposition of the bed and banks. However, these conditions are seldom consistent due to year-to-year weather-dependent fluctuations. The long-term variations are credible due to the impacts of land use changes and human interventions. The bed and banks of these alluvial reaches are composed of sediment transported by the river through time. That means, the channel is not confined to the rock bed but flanked by the flood plain of small and/or undefined banks (Lagasse et al., 2001). In the dry season, clear water scour conditions are predominant, resulting in insignificant morphological changes due to the ephemeral nature of most streams. However, live bed and bank scour happens reasonably during high flow times. The alluvial reaches with these erosion-prone banks are significantly sensitive to the flow variations and/or complications happening due to the effects of the bridges constructed across the valleys.

2.4 Data collection

2.4.1 Primary data collection

Field observations were made to collect soil samples from the selected bridge sites, and field measurements with important parameters were taken in the first phase (November and December 2021), in the second phase (February and March 2022), and in the third phase (April and June 2022). Reconnaissance observation of the bridge site was a preliminary important aspect of the geomorphic study to assess whether the bridge is susceptible to scour failure or not. Primary evaluation of the selection of the bridges was based on the checklist prepared according to the HEC 20 manual. Field observations and measurements of the valley width, GPS elevations (above mean sea level), opening width, pier diameter, valley shape, bedforms, sediment characteristics, drift accumulation, flood marks, flow behavior, channel classification, obstructions, erosion activity, and riparian vegetation were evaluated according to the guidelines of rapid assessment of channel stability (Lagasse et al., 2001)**.** Bed soil samples were taken in wet and dry seasons

(November 2021 and February 2022) to handle the effect of the armoring layer on the sample homogeneity. Sample of the bed soils were dug from the upstream zone of flow contraction and downstream zone of flow expansion as well as the bed of the bridge site in which the flow is constricted. The sample depth varied form 0.5m in some pit sites to 1m in most pit sites at the Wajifo, Alge, and Kulfo bridges to account for relatively undisturbed subsurface bed layer. Hence the top coarser armor bed layer was assumed to be disturbed during high floods. In case of Sile and Sego bridge sites, the particle distribution through pit depth was uniform and the surface of thin sand armor layer was less than 0.3m for most pits.

2.4.2 Secondary data Collection

2.4.2.1 Satellite Image Data

Landsat 5, Landsat 7, and Landsat 8 satellite images of 30x30m resolution from the USGS archive were used for 38 years from 1984 to 2021 as shown in Table 1 below owing to its availability for a long time as compared to other higher resolution imagery to perform geomorphological analysis.

Table 1. Landsat image collections used for ROI

No	Satellite	Image collection	Date	No of images
1	Landsat 5	LANDSAT/LT05/C02/T1_L2	12/04/1984 to 30/12/2001	537
2	Landsat 7	LANDSAT/LE07/C02/T1_L2	01/01/2002 to 31/12/2012	384
3	Landsat 8	LANDSAT/LC08/C01/T1_TOA	01/01/2013 to 08/11/2021	355

2.4.2.2 Rainfall Data

Some rivers in this route have gauging stations and meteorological stations nearby. However, most of the bridges located at the ungagged catchments rainfall data were used from EMI as shown in Table 2 below.

Table 2. Rainfall data

No	Station Name	Year	Percentage missed (%)	Bridge site used
1	Mirab abaya	1976 – 2016	8.34	Alge and Wajifo
2	Arba Minch	1976 – 2016	7.85	Kulfo
3	Gato	1976 – 2016	2.83	Sile and Sego

2.5 Methodology

2.5.1 General Conceptual Framework

The general methodological framework of the study is shown in the Figure 2 below.

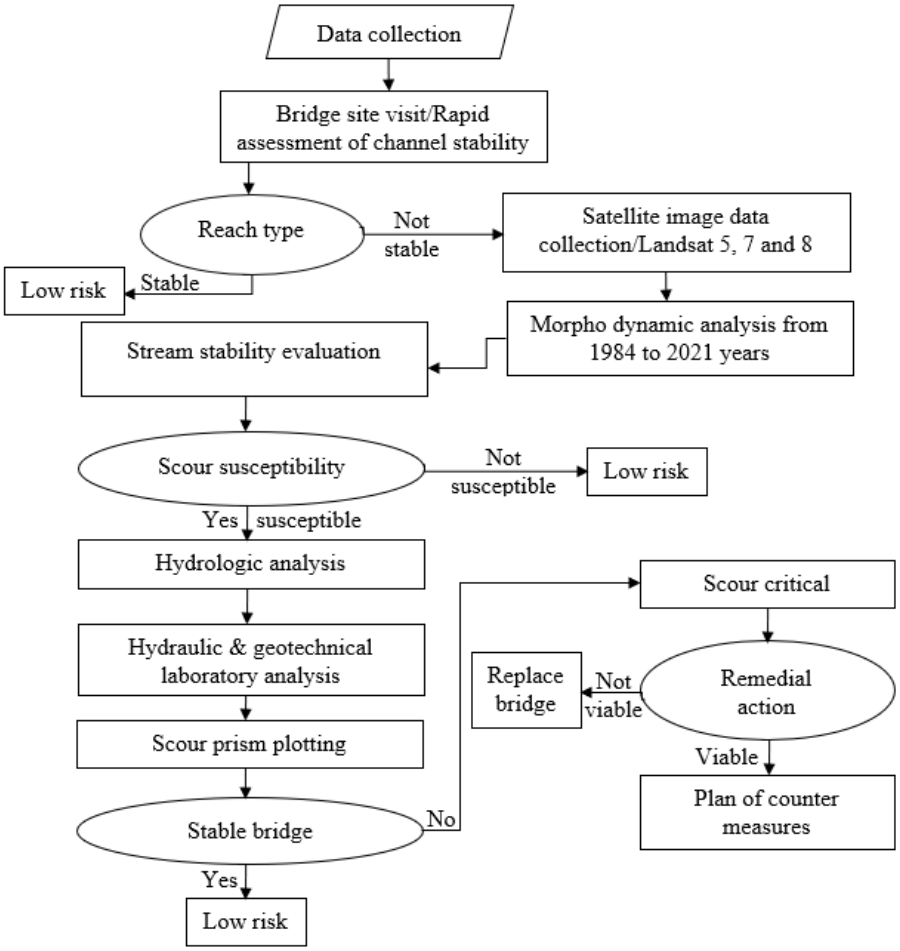

Figure 2. Conceptual framework of the study

2.5.2 Selection Based on Field Observation

There are more than 15 bridges over the stream valleys crossing the Sodo to Konso highway as listed in Table 3 below. Some of these valleys are more actively adjusting their beds and banks frequently during the bridge's useful life operation. The selection was conducted according to assessment of the channel stability (Lagasse et al., 2001). Evaluation criteria were used to determine whether a bridge is low risk or susceptible to scour, based on a standardized checklist.

Table 3. Scour susceptible bridge evaluation based on field observations

No	Bridge name	Pier width (m)	No. of span	Pier type	Valley width (m)	Scour evaluation	Remark
1	Hamessa		3	Round nose	46.4	Low risk	Rocky stable bed and banks
2	Wajifo		4	Circular	63.4	Scour susceptible	Upstream right bank as well as middle span bed degradation & improperly placed upstream small gabion check dam
3	Welo		1		20	Low risk	Small catchment
4	Keme		3	Circular	45	Low risk	Small catchment
5	Alge /Shafe		2	Circular	33	Scour susceptible	Aggradation (drift accumulation) in the left span and degradation in the right bank (abutment scour)
6	Baso		3	Circular	60	Low risk	Relatively stable bed & banks
7	Hare		2	Round nose	30.5	Low risk	Upstream right bank degradation (small extent)
8	Kulfo (upper)		3	Circular	48	Scour susceptible	Bed degradation in the middle span & right abutment
9	Kulfo (lower)		5	Circular	60	Low risk	Bed aggradation
10	Sile		2	Circular	40	Scour susceptible	Upstream meander, loose banks and existing bridges
11	Sego /Elgo		1		14	Scour susceptible	Degradation in the upstream banks/upstream braided stream and abutment scour
12	Wozeka		5	Round nose	100	Low risk	Bed aggradation
13	Gato		3	Circular	60	Low risk	Relatively stable stream

14	Bayde		4	Round nose	82	Low risk	Relatively stable stream
15	Kayle		4	Round nose	80	Low risk	Stable but there is human interference (bed sand mining)

2.5.3 Morphodynamic Analysis

Alluvial morphodynamic awareness is important for engineering decisions regarding the analysis of new and existing hydraulic structures. Unlike geomorphologists and geologists, engineers are concerned with changes in river morphology relatively for a short period of 10 to 20 to 50 upto 100 years(R.J.Grade, 2006). Based on the field observations and scour susceptibility, five bridges namely Wajifo, Alge, Kulfo, Sile, and Sego were selected for analysis. The banks and beds of these bridge sites were relatively unstable as compared to other bridge sites as shown in Figure 3: (a) Wajifo bridge site with improper upstream gabion check dam (b) Alge bridge with channel migration to the right bank (c) Kulfo bridge with bed scour at the middle span (d) and (e), Slie bridges new and existing respectively with bank and bed scour (f) Sego bridge with left bank scour and flow obstruction due to the existing bridge abutment.

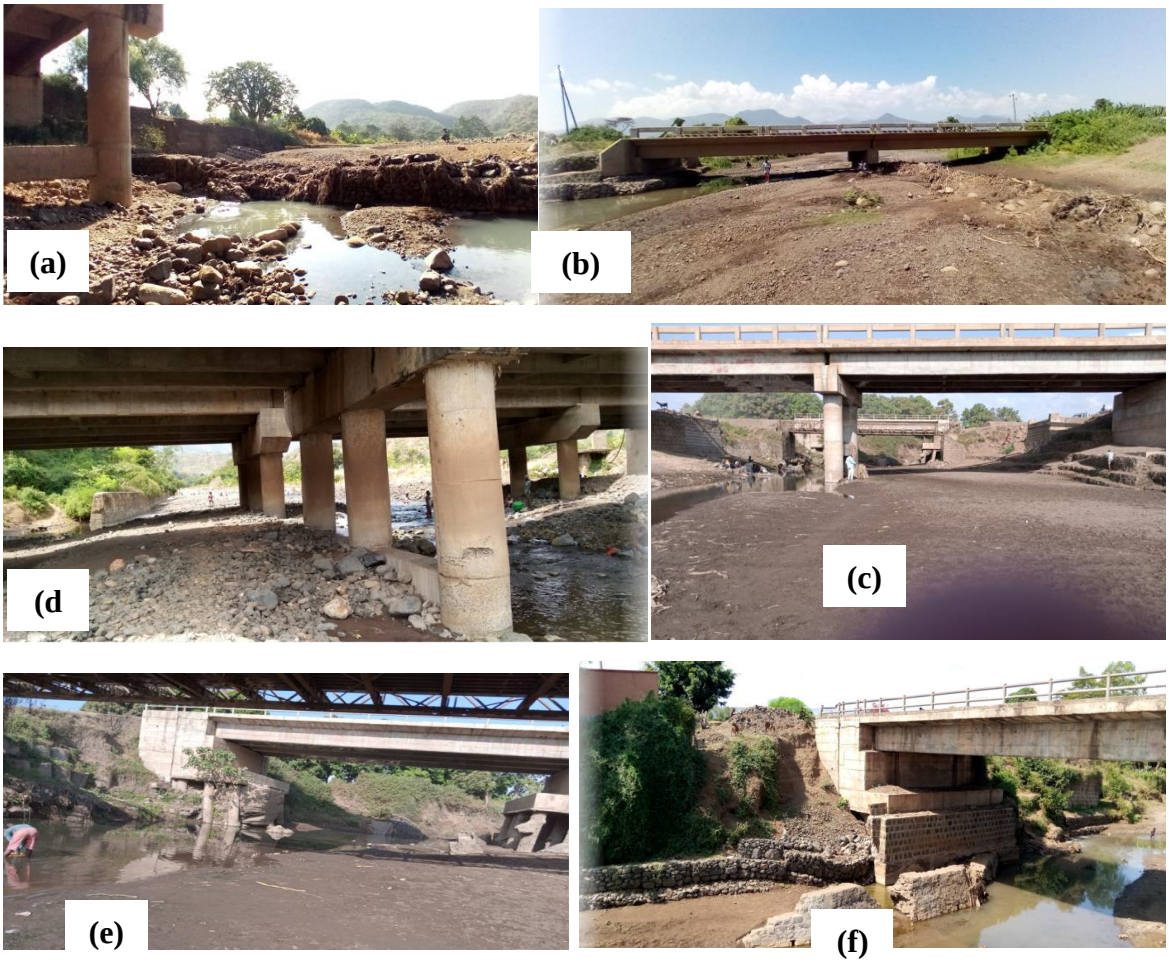

Figure 3. Scour susceptible bridges site photos

2.5.4 Landsat Image Analyses

The cloud-based computing platform Google Earth Engine (GEE) was used to analyze large geospatial datasets (Gorelick et al., 2017). In this study, GEE was used for active channels as a mask for Landsat images. The procedures were executed on this semi-automated platform for image collections from 1984 to 2021 on the annual basis of the ROI. Rectangular ROI for the river reach with a defined and visible flow channel near the bridge site was selected for each bridge. These areas were 20.25, 21.25, 23.54, 24, and 32.62 km2 for the Sego, Sile, Kulfo, Alge and Wajifo rivers, respectively. According to (Boothroyd et al., 2020)**,** the first yearly image collections were filtered, then cloud masking (Foga et al., 2017) was applied for shadows of clouds and annual images were composited using a median reducer to aggregate the cloud-masked images.

Annual composite images were used to manage incomplete images of ROI in path 169 & rows 055 to 056 and to overcome cloud-obscured scenes by cloud masking or SLC-off stripes in Landsat 7(Schwenk et al., 2017). Active channel classification was applied based on spectral indices MNDWI (Equation 3.1), NDVI (Equation 3.2) , and EVI (Equation 3.3) thresholds (Zou et al., 2018). The active channel mask output of the grayscale image for MNDWI ≥ -0.4, NDVI ≤ 0.2 thresholds (Boothroyd et al., 2020) , and EVI < 0.1 to remove mixed pixels of vegetation and water (Zou et al., 2018) were computed. Finally, the GeoTIFF image of the active channel was exported to Google Drive.

$$\text{MNDWI} = (\text{Green - SWIR})/(\text{Green} + \text{SWIR})$$

$$\text{NDVI} = (\text{NIR} - \text{Red})/(\text{NIR} + \text{Red})$$

$$\text{EVI} = 2.5^{*}\ [(\text{NIR} - \text{Red})/(\text{NIR} + 6 * \text{Red} - 7.5 * \text{Blue} + 1)]$$

Where: MNDWI – Modified normalized difference water index

NDVI – Normalized difference vegetation index

EVI – Enhanced vegetation index

NIR – Near infra-red

SWIR – Short wave infra-red

Band designation:

(a) B1, B2, B3, B4, and B5 are blue, green, red, NIR, and SWIR respectively for Landsat5 & Landsat7.

(b) B2, B3, B4, B5, and B6 are blue, green, red, NIR, and SWIR respectively for Landsat8

Figure 4 shows the GEE procedure applied to the ROI of Alge River reach comprising 7.5 km length and 3.2 km width (a) the raw Landsat images of each year were smashed together for temporal compositing after cloud masking (b) classification of active channel (c) NDVI (d) active channel with NDVI background.

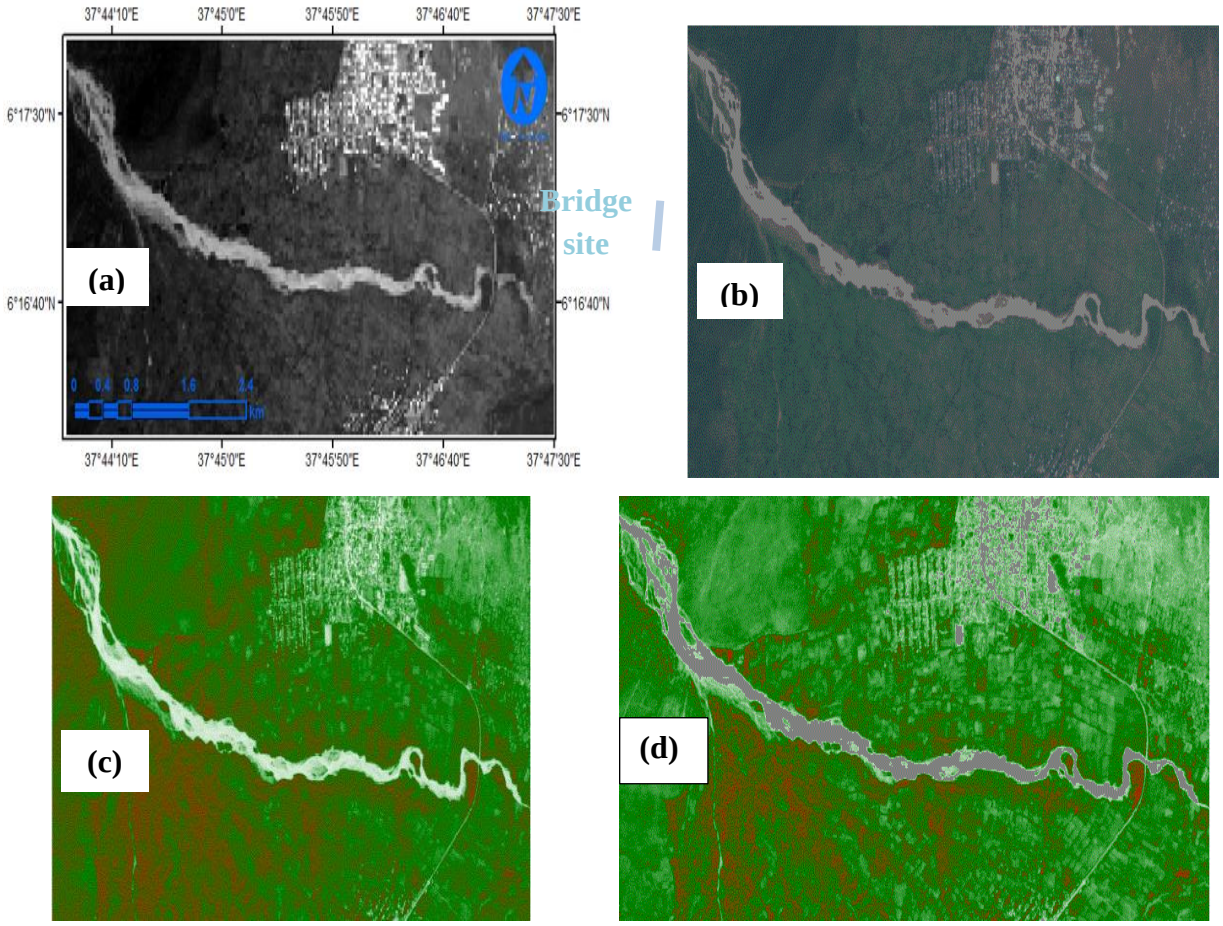

Figure 1. Alge River reaches active channel classification

2.5.5 HEC RAS model setup

In this study, HEC RAS 6.4.1 model was used to hydraulic analysis of river channels. It comprises hydraulic analysis components, data processing, reporting and storage facilities to analyze steady flow computations, unsteady flow simulation, sediment transport, and water quality analysis. Additionally, the model requires inputs such as river geometric data, floodplain elevation and length, channel cross section data, Manning's roughness coefficient, boundary conditions and flow data to provide rating curves, water surface profiles, EGL (Energy Grade Line), velocity, flow area, slope, elevation and stream flow visualization (USACE, 2016).

Hydro-meteorological data, spatial data, field measurements and design documents were used to fulfill the model data requirements. For the selected bridge sites, TIN was developed from 12.5x12.5m DEM from ALOS PALSAR, USGS with the help of HEC-GeoRAS to extract stream length, cross sectional data and over bank floodplain conditions. Cross sectional locations were selected based on the perpendicular crossing to the channel center line (Gary W. *et al*, 2021) in a manner that it should not cross each other.

Bridge cross sectional data were collected from field observation, measurements and/or design documents. In case of Kulfo and Wajifo, design documents were used to get dimensions of piers, abutments, span length, lower and upper chord elevations but for the Alge, Sile and Sego bridges these parameters were measured from field by using Tap meter and GPS. The important dimensions for scour analysis in HEC RAS input were shown in the Table 4 below.

Table 4. Selected bridge cross sections

No	Bridge name	Pier width (m)	Abutment type	Elevation (m)	
				High chord	Low chord
1	Wajifo	1.2	Sloping 1:10 (H: V)	1217	1215.05
2	Alge	0.73	Vertical	1199.24	1198.49
3	Kulfo	1.02	Vertical	1229.8	1228.52
4	Sile	1.21	Vertical	1110.72	1109.52
5	Sego	No pier	Vertical	1117.13	1116.13

3. RESULTS AND DISCUSSION

3.1 Active channel migration

The focused ROI for Sego, Sile, Kulfo, Alge and Wajifo rivers using RivMap toolbox centerline analysis (Schwenk et al., 2017) was applied to 38 years from 1984 to 2021centerlines from the annually resolved active channel masks (Figure 5) show that the morphdynamic change of each river reach.

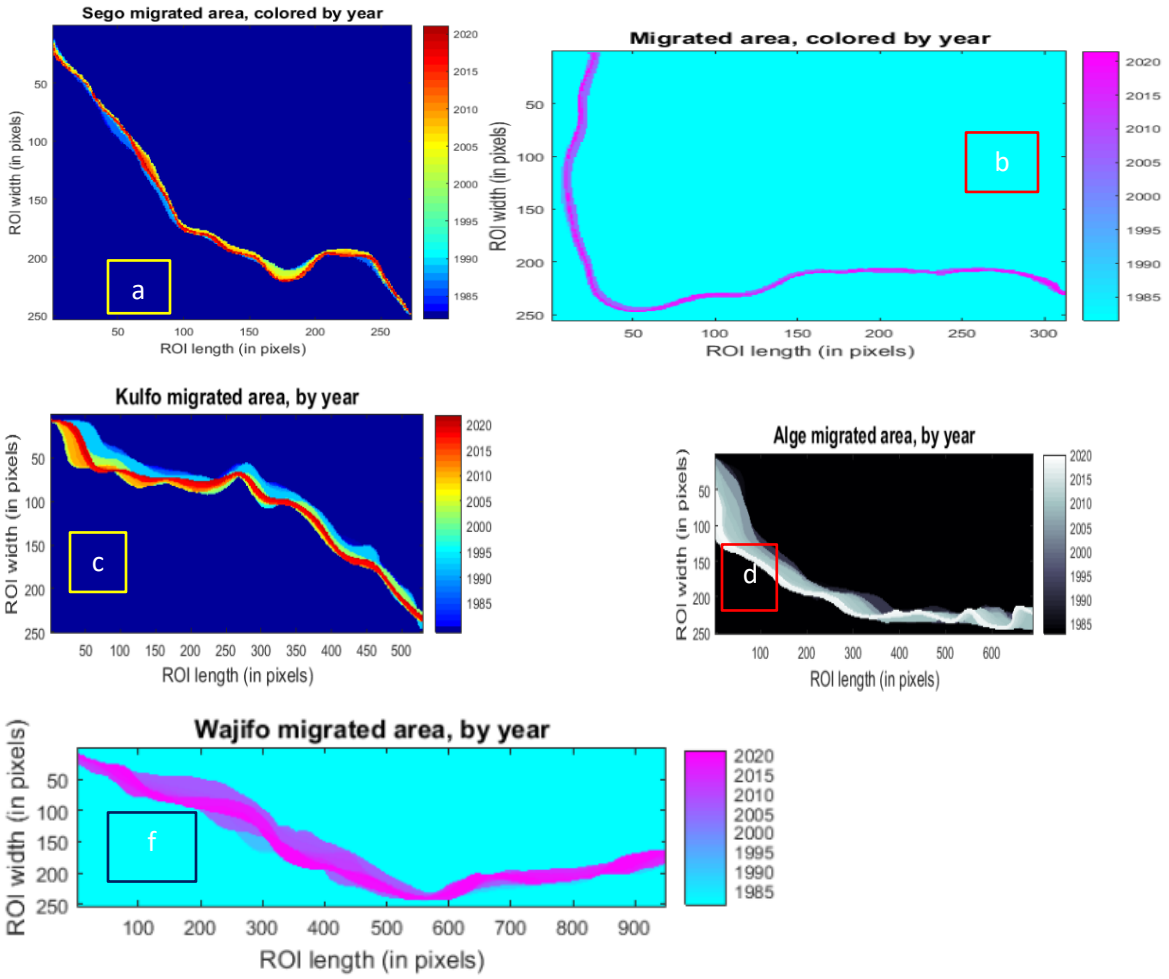

Figure 5. Center line migration rate (marked areas are bridge sites)

The cumulative center line migration area of 38 years was 0.0052, 0.0065, 0.04, 0.117, and 0.128 km^2 for Sego, Sile, Kulfo, Alge, and Wajifo bridge sites, respectively. This result shows that Alge and Wajifo bridge sites (reach near the bridge) encounter relatively unstable streams laterally. The channel migration rate, which is calculated from the ratio of the migrated area to the length of the center line, shows that the maximum migration rate of 20.45 m/year, which occurred in 2007 in Wajifo reach (Figure 6 (a) and 22.36 m/year occurred in 2011 in Alge reach (Figure 6 (c). The migration rate of Wajifo reach near the bridge site has become greater than the entire reach migration rate starting from the year 2013. As shown in Figure 6(b) and (d), the cumulative migrated area was also shown.

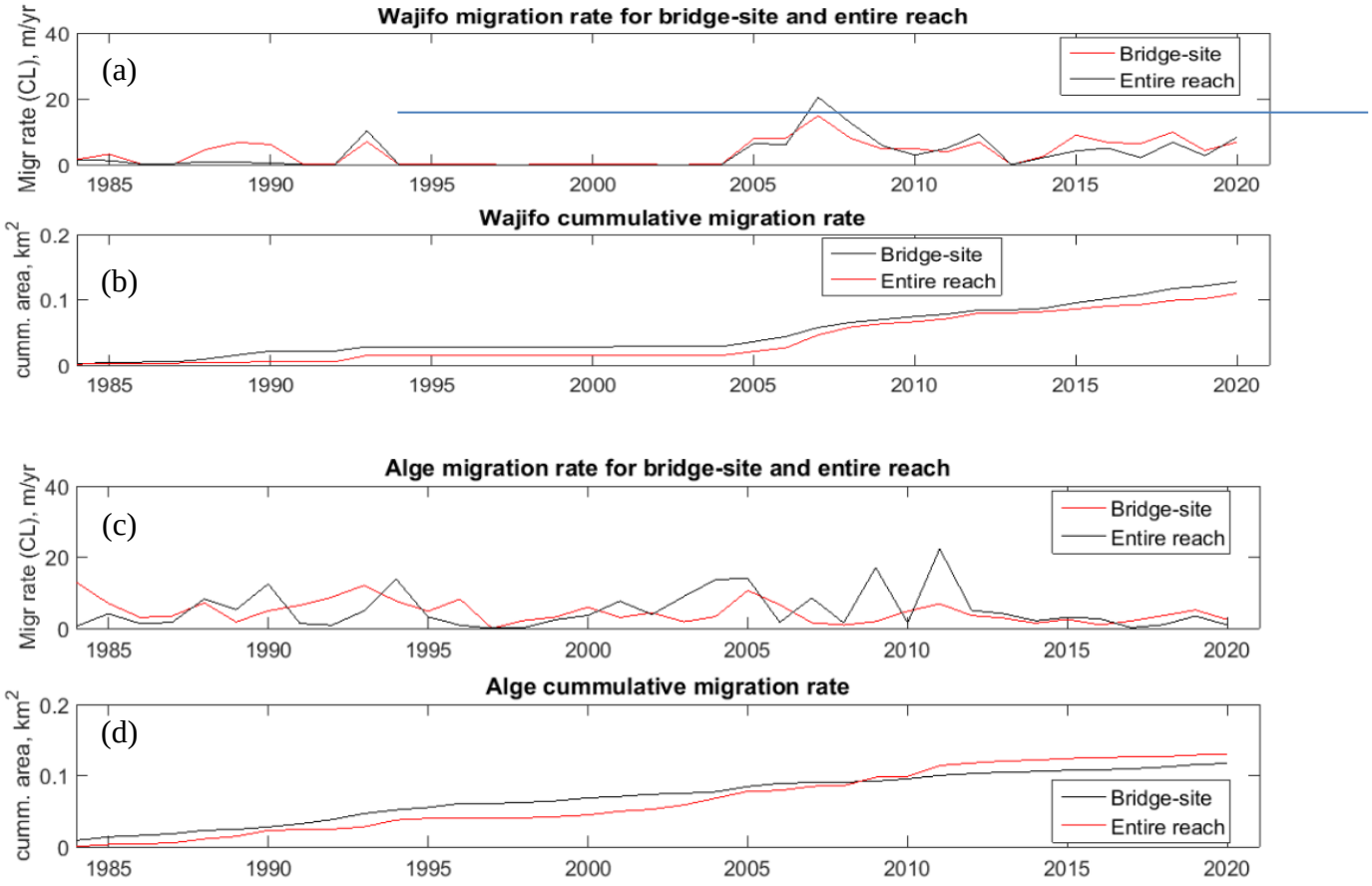

Figure 6. Wajifo and Alge migration rate including cumulative area

The maximum and average migration rates of the reach were plotted for the entire 38 years as shown in Figure 7 below. The result shows that Sego and Sile flow channels face relatively low center line lateral migration as compared to others. In the case of the Alge, Wajifo, and Kulfo rivers, the lateral shifting of the flow is relatively greater. The average migration rate near the Alge Bridge site is higher as compared to the rest of the selected sites.

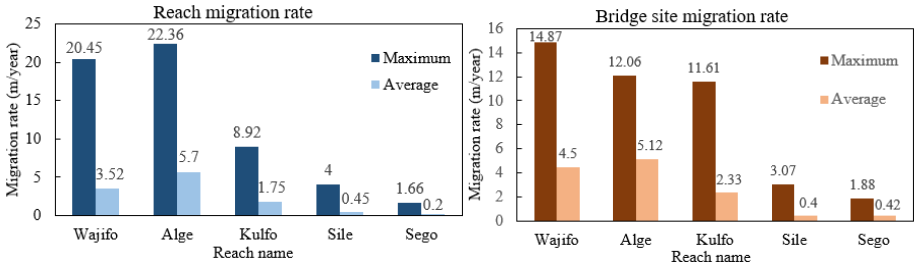

Figure 7. Maximum channel migration rates for river reach and near the bridge site

3.1.1 Contraction Scours at Selected Bridge Sites

Roughness coefficients were used in a range from 0.034 at Sile bridge site to 0.083 at Wajifo bridge site for the channel bed, as well as 0.10 Sego to 0.205 at Alge bridge site for the overbank floodplain.

The scour analysis has been conducted for a 50-year, 100-year, and 500-year flood event to evaluate the bridge foundation under a super-flood condition (USACE, 2016). The constriction of the valley due to the construction of the bridge aggravates the contraction scour potential with the incremental velocity induced by the rapidly varying flow at the crossing. Contraction scours in these reaches indicate how much bed material is already being transported from the upstream bridge zone of contraction. The result in Figure_8 below shows that the Sego Bridge faces relatively higher contraction scour depth for all flood events. This happened due to the extreme narrowing of the natural channel at the bridge site. Clear-water contraction scour occurs at the Sego bridge site, causing higher scour depth in the contracted section. This is due to the reason as documented(FHWA, 2012), the velocity, shear stress, and transport of sediment decrease in the upstream section of the bridge because of the rise in the backwater flux.

On this bridge site, the river banks near the bridge were narrowed by the gabion approach guide-banks projecting to the upstream channel and road embankments force the wide channel and over bank upstream flow to the main channel at the bridge (Figure 9). It is seen that the raising of the flow depth near the upstream face of the bridge is indirectly proportional to the bed slope of the channel, indicating narrowed natural flow (Figure_9 (a)). Kulfo and Wajifo bridges encounter smaller contraction scour depth due to the bridge spanning fully the entire floodplain for all events. In addition to this, Sile bridge contraction scour depth is relatively sensitive to the variation of the flow magnitude.

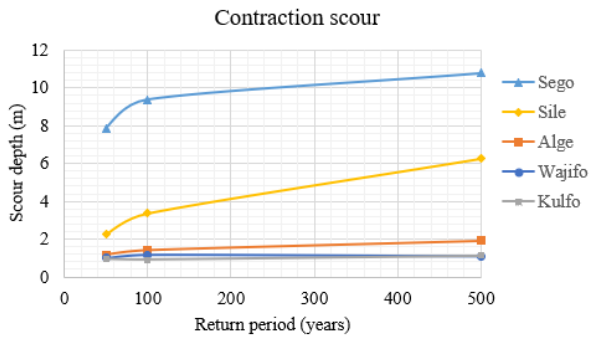

Figure 8. Contraction scour potential in the selected bridge sites

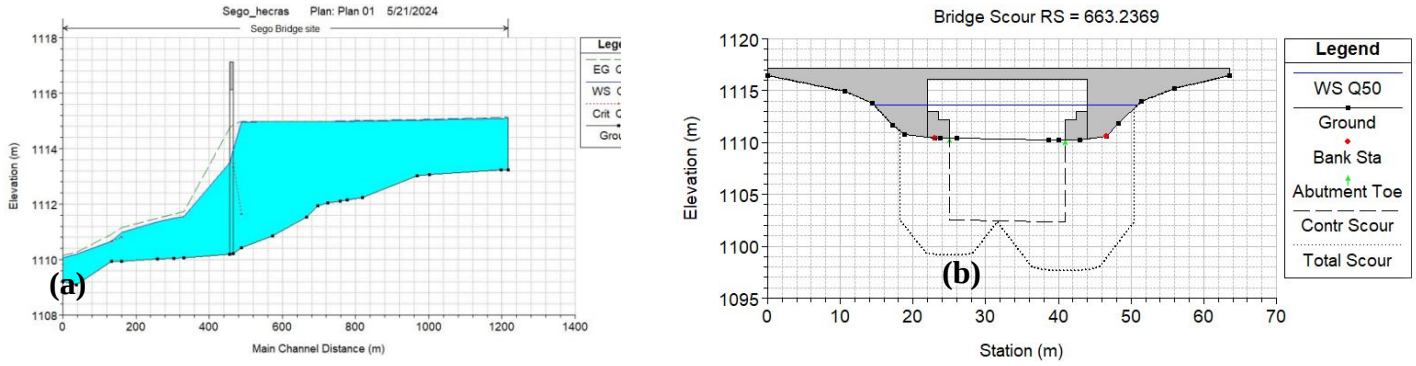

Figure 9. (a) Sego longitudinal flow profile (b) Scour prism

Regarding Sego Bridge, the channel width at the bridge site is about 20m, unlike the natural wide channel within the upstream distance to the bridge. This results in incremental contraction scour potential. The average approaching flow velocity at Sego, Alge, and Wajifo bridge sites are less than the scour critical velocities of the respective sites as shown in Figure_10 below, revealing clear-water scour. However, in Kulfo and Sile, the average approach velocity is greater than scour critical velocity resulting in live-bed contraction scour. It shows that there is appreciable bed material (sediment) movement in the approach section rather than on the bridge site of the Kulfo and Sile channels. (), the bed material transport in the uncontracted approach section is less than the carrying capacity of the flow in Alge, Sego, and Wajifo.

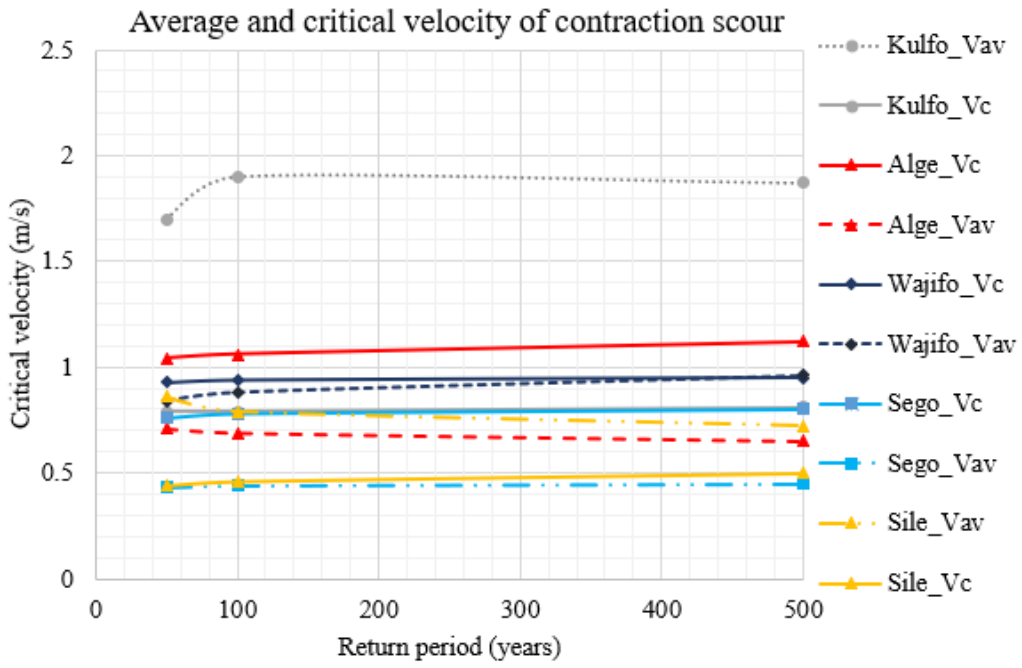

Figure 10. Plot of approach and scour critical velocity

3.1.2 Local scour conditions in the selected bridge sites

3.1.2.1 Pier scour potential

The local scour hole formed around the pier is the horseshoe type for all selected bridges having groups of circular cylinder shapes. During the pier scour analysis of the existing bridges, the CSU equation is recommended (USACE, 2016) and the Froehlich equation result from the HEC RAS model is mostly used to analyze new bridge scour analysis due to its higher scour depth, which is considered as a factor of safety. The result shown in Figure 11 below reveals that the pier scour depth of 50-, 100- and 500-year events of the selected bridges resulted from the Froehlich analysis are greater than the CSU equation analysis. Since all the bridges exist, CSU results are acceptable, and Froehlich equation outcomes are plotted only for comparison. Upper Kulfo bridge is experiencing higher pier scour depth (Figure 12 (a)) and Alge bridge has lower pier scour depth (Figure 12 (b)) in which bed aggradation is happening especially on the left bank of the structure.

Figure 11. Local pier scour depth plots for the selected bridge sites

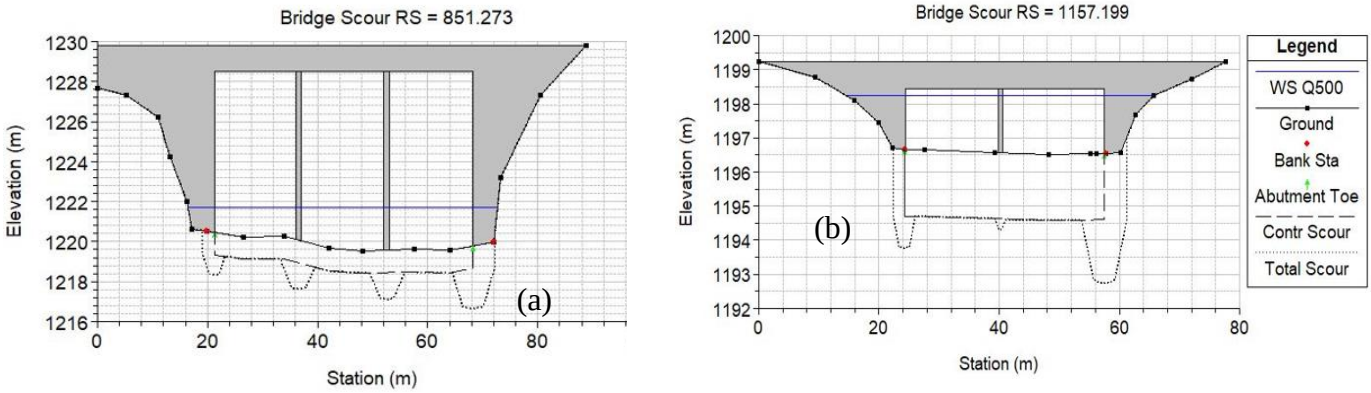

Figure 12. Scour plot for the 500-year event (a) Kulfo and (b) Alge

Concerning Wajifo bridge (Figure 13), pier scour is also dominant, especially within two middle spans due to the impact of a partially failed gabion check dam (Figure 3 (a)) resulting in flow complications upstream of the pier.

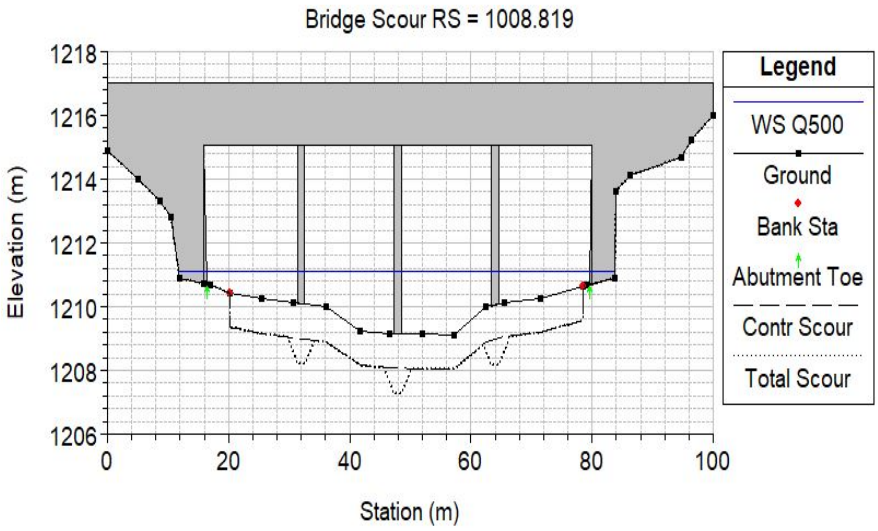

Figure 13. Wajifo scour plot for the 500-year event

3.1.2.2 Abutment scours

The local abutment scour results show that the Sile (Figure 15) bridges are facing higher scour depth because of large flood events and the Wajifo Bridge isn't affected by abutment scour (Figure 13) due to the large span bank to bank opening of 64m

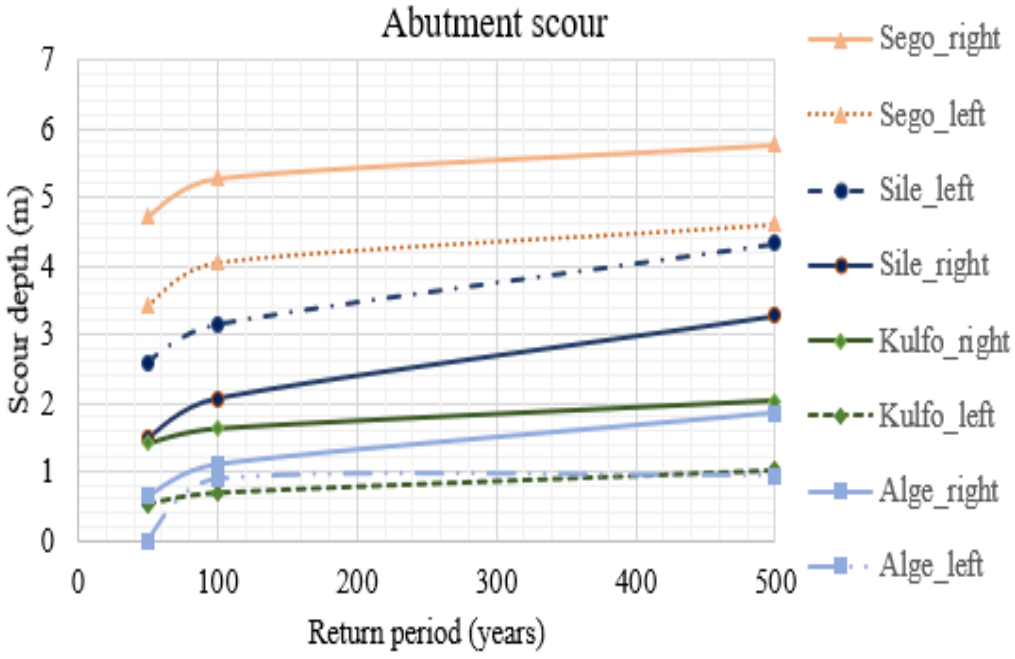

Figure 14. Local abutment scour plot for the selected bridge sites

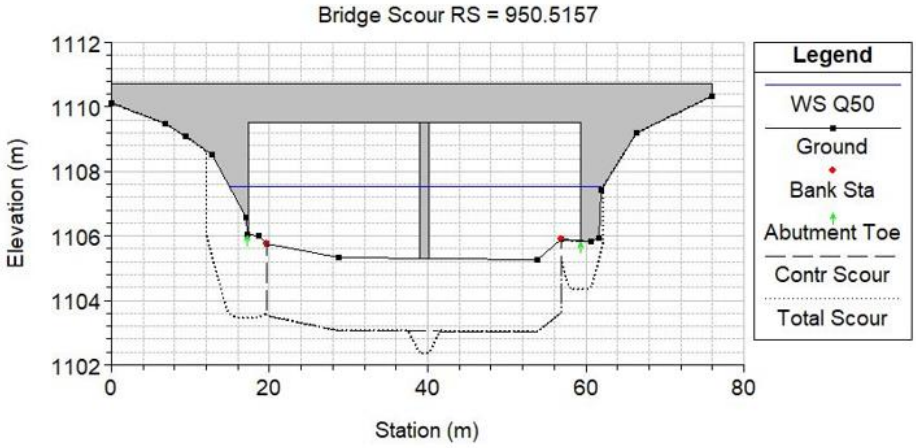

Figure 15. Scour plot result for Sile bridge site

In the case of Alge and Kulfo bridges, the right bank abutments are facing more scour holes (Figure 12). The flow on the Alge Bridge is confined to the right bank (span), hence the left one is clogged with drift accumulation and bed aggradation. Kulfo bed on the left side is used to divert flow to the field by modifying the natural bed and there is a small gap between the right abutment and the old artificially made right guide bank, resulting in vortex flow confined to the abutment.

3.1.3 Major hydraulic factors for the scour problem in the selected sites

The major hydraulic factors for the scour problems in the selected sites are related to both the bridge structural dimension (opening ratio) impact on the flow and the nature of the channel reach geomorphology. The bridge opening ratio (ratio of discharge passing through the bridge opening location before construction to the total flow confined within left up to right abutment after the bridge construction) influences most of the selected bridges. The opening ratio ranges from 0 to 1, representing extremely narrow flow constriction resulting in high afflux and contraction scour to the abutments constructed on the full width of the flood plain experiencing lower contraction scour depth. The minimum opening ratio shows that the natural flood plain is more narrowed (Figure 16). On Wajifo and Kulfo bridge sites, the original flood plain was not narrowed during the construction of the bridge, but in Sego the constriction is higher (minimum opening ratio), resulting in high afflux (Figure 9 (a)) and Sile (Figure 17 (a)) and Alge (Figure 17 (b)) also this factor impacts the flood plain. Even though the narrow opening of the bridge is economically viable, it induces high contraction scour.

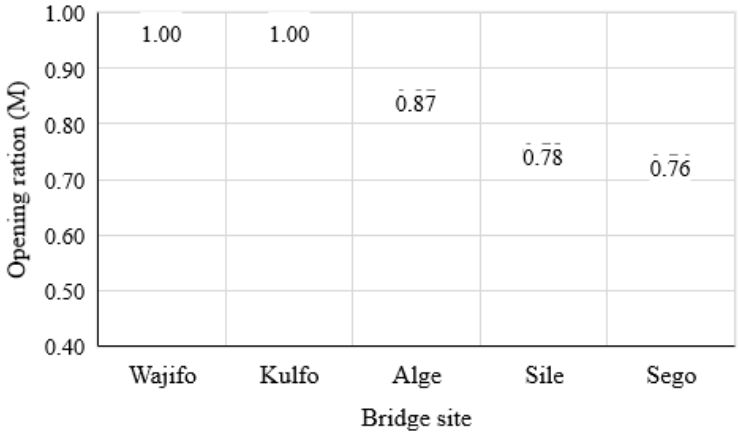

Figure 16. Bridge opening ratio for the selected sites

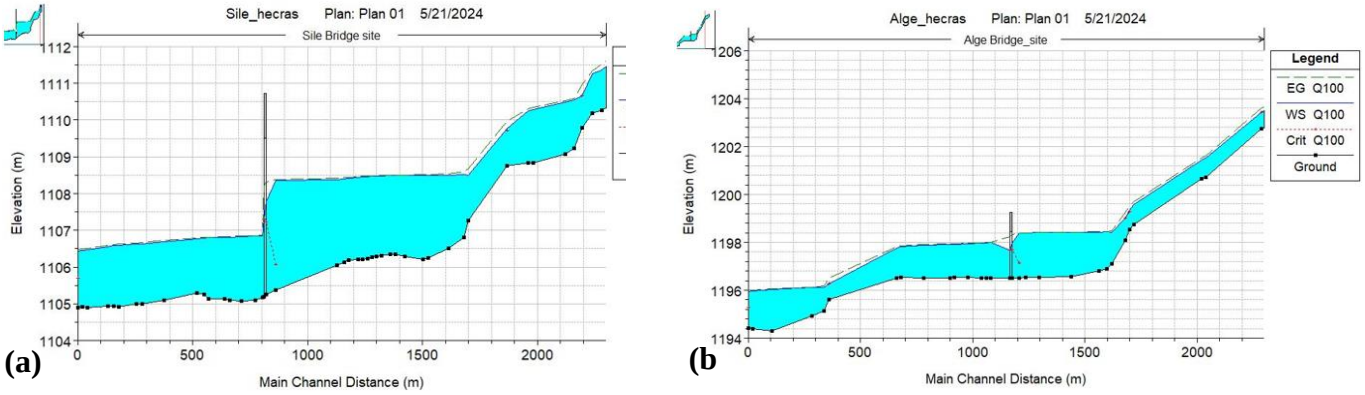

Figure 17. Flow depth variations due to the bridge opening ratio (a) Sile site (b) Alge site

Morphodynamics of the channel has also another impact on bridge scour evolution. Channel, reach migration rate (Figure 6 and 7) through time impose significant impacts to the scour process. All the selected bridges are located in the lower reaches of the channels with low and undefined banks confining the flow. Thus, it results in frequent lateral migration and widening of the channel through time. Lateral channel migration affects the channel, left and right over bank flow magnitudes, velocities, angle of attack, and flow depth.

3.1.4 Remedial alternatives for scour conditions

Prudent scour countermeasures for scouring critical bridges are based on both observed current scour susceptibility in bridge pier and/or abutment. The scour analysis evaluation results for the 100-year event indicate critical conditions that align with FHWA guidelines(FHWA, 2009).
The current field observation of the selected sites confirms the analysis results of the HEC RAS model. The current field status of the Kulfo, Wajifo, and Alge bridges shows that there are active local bed scour (Kulfo & Alge) and bank scour (Wajifo upstream right bank) conditions. However, the analysis results for high flood events revealed that there were low-risk bridges that could be mitigated by relatively minimal efforts. Wajifo Bridge was not affected by the abutment scour problem with all flood events, but local pier scour was developing in the middle span owing to the partial failure of the gabion check dam near the upstream face of the bridge. The bed gabion treatment was proposed in the original design of the bridge. Therefore, the maintenance of the bed according to the design would secure the vulnerability of the pier scour. However, the scour analysis result indicated low risk on the Alge bridge site. The right abutment scour was developing because of the flow confinement to the span and the drift accumulation of the wood and banana trees on the left span of the bridge blocking the flow.

In the case of New Sile bridge there was no current scour effect in the field, but for large flood events the scour effect was significant (scour critical). However, on the Sego bridge site, the current status showed that the banks near the bridge were protected by the gabion rock and masonry but the approaching upstream flood plain was facing active bank degradation and lateral widening. In addition to this, the long-term large flood event analysis indicated that the bridge's scouring was critical (Figure 18).

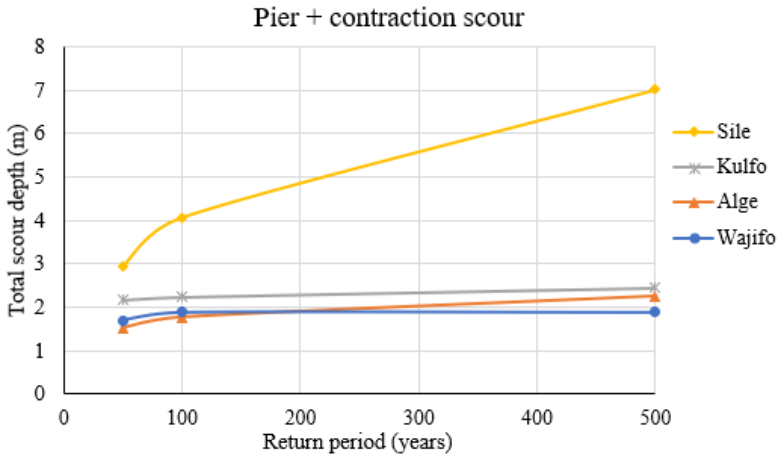

Figure 18. Total pier scour plot for selected bridge sites

As in Figure 18, Sile Bridge faced appreciable pier scour depth during large flood events, but for the rest of the sites the total pier scour depth varied between 1.51m for the Alge site during the 50-year return period and 2.45m for the Kulfo site during the 500-year return period.

The result of the total abutment scour depth (Figure 19) showed that both abutments of the Sego Bridge were highly scouring susceptible as compared to others. In the site of Sile, the left abutment was more susceptible to the migration tendency of the channel to the left bank in the downstream vicinity of the bridge. The right abutment of Alge Bridge was susceptible as the flow channel was confined to the right bank throughout time. The total scour depth obtained in this analysis could be interpreted as overestimated values rather than the actual values (Cooperative et al., 2006; Hong & Abid, 2015) due to the effect of scaling in analysis equations. The relative importance of the highway route was based on the ADT Significant factors influencing the frequency of inspection strategies in a plan of action(FHWA, 2009). In this connection, the relevance of the Sodo to the Konso-Jinka federal highway was not compromised. Therefore, the Sile and Sego bridges had critical scour, demanding timely, frequent scour inspection and monitoring.

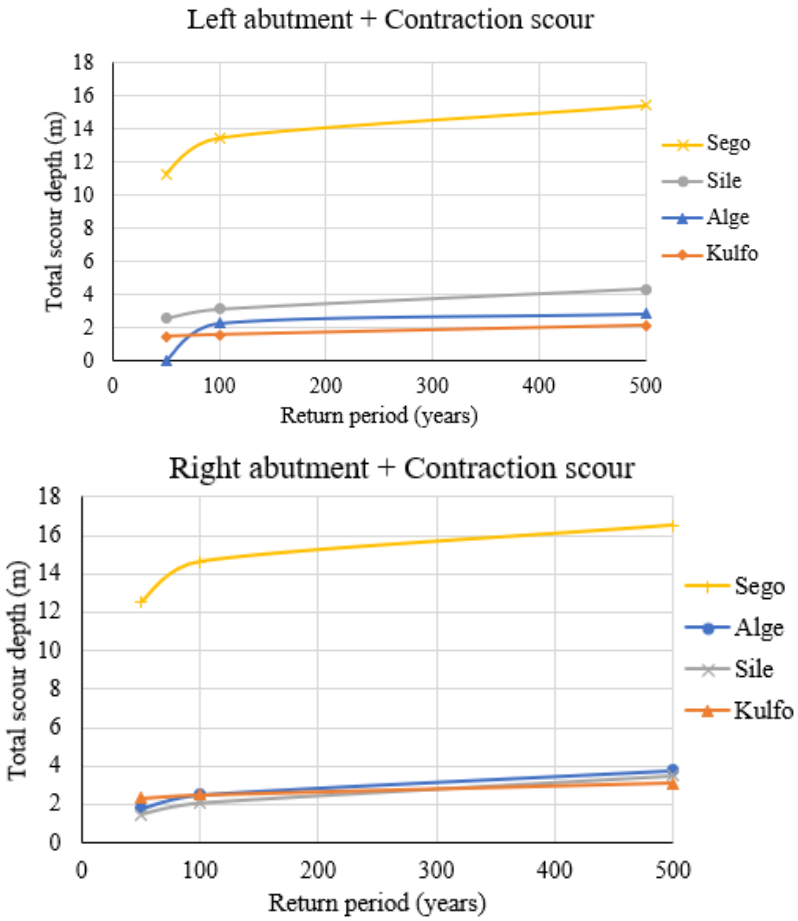

Figure 19. Total abutments scour at the selected sites

Retrofitting the scour countermeasures to stabilize existing scour susceptible bridges was good engineering practice in terms of economy and targeting the desired limitation on the useful life of the structure due to scour problems (FHWA, 2009).

3.1.4.1 Countermeasures proposed for contraction scour

According to the analysis, Sego Bridge was adversely affected by the contraction scour. In this case, a relief bridge or culvert near the left bank was alternatively needed to alleviate the contraction of the flow (Figure 20). Gabion check dam across the bed of the channel would prevent degradation of the bed.

Figure 20. Proposed relief bridge or culvert site at Sego

Sile Bridge was also suspected to have a high contraction scour potential next to the Sego site. Hence, the rock gabion check dam across the bed of the channel could reduce this effect in the Sile site.

3.1.4.2 Countermeasures for local scour problem

Effective countermeasures for local scour at bridge piers are essential to ensure the long-term stability and safety of bridge structures, particularly in alluvial rivers where sediment transport and channel dynamics are active. These countermeasures aim to either prevent excessive flow concentration around the pier or protect the foundation from erosion. Commonly adopted solutions include the installation of riprap or armor layers**,** guide vanes**,** collars, and scour-resistant footing designs, such as deep foundations or pile extensions below the maximum predicted scour depth. Additionally, geotextile mats**,** gabions, and encased rock aprons can be used to shield the bed from shear stress and flow turbulence. The selection of an appropriate countermeasure should be based on a detailed hydraulic analysis, site-specific flow conditions, sediment characteristics, and long-term channel stability assessments. Incorporating such protective measures not only mitigates scour risk but also extends the service life of the bridge and reduces maintenance and repair costs. Therefore, at the Sego bridge site**,** abutment scour is notably severe and can be effectively mitigated through the application of armoring techniques (Coleman, 2000), with rock gabion mesh identified as a particularly cost-effective solution. Moreover, to enhance flow alignment and

reduce hydraulic stress near the bridges, the installation of guide banks is recommended at the Sego, Sile, Alge, and Wajifo bridge locations

4. CONCLUSION

Bridge scour analysis was conducted at 5 selected bridge sites in the HEC RAS hydrodynamic model in addition to the 38-year morphodynamic analysis of the reach geomorphology from landsat images to identify scour critical bridges for high flood events. The scour analysis results were interpreted comparatively with the observed site conditions. The main findings of the comparative analysis indicated that the reach spatial and temporal morphodynamic change of the bridge sites showed lateral widening of the floodplain. The river channels were becoming wider near upstream and downstream of the bridge through time. In addition to this, there were active sediment bars and channel bank modifications, especially near the upstream floodplain of the Wajifo, Alge, and Sego bridge sites. Scour analysis for high flood events showed that the contraction scour potential was dominant at the Sego, Sile, and Alge bridges. This was mainly due to the narrow opening of the bridge in contradiction to the upstream channel widening from time to time. Local scouring of piers and abutments had effect on the safety of these bridges. Sego and Sile bridges were highly suspicious of the local scour for high flood events. These two bridges needed timely, frequent monitoring systems and remedial countermeasures. On the other hand, the Wajifo, Alge, and Kulfo bridges were less suspicious of the effect. Thus, a detailed geomorphological understanding of the channel reach was an important aspect to understand the evolution of the floodplain and provision of the bridge opening ratio in addition to the geotechnical, hydraulic, and structural analysis.

Author contributions:

Aklilu Alemayehu Kassaye: contributed to project administration, methodology, investigation, conceptualization, formal analysis, validation, supervision, resource management, and both original drafting and reviewing/editing of the manuscript.

Mesele Markos Forsido: contributed to the project by writing the original draft, validating the results, developing software, designing the methodology, performing formal analysis, curating data, and conceptualizing the study.

Conflict of interest: The authors declare no conflict of interest.

Funding source: Arba Minch University, Water Resource Research Center

Declaration

We here submitted the manuscript entitled "Morphodynamic Alterations and Scour Processes around Bridge Openings: A Case Study of Selected Bridges on the Sodo-Konso Highway, Ethiopia" to be considered for publication. We declare that this is our original research work.

REFERENCES

Beyene, A. M., Abate, M., Sinshaw, B. G., Belete, A. M., & Chekole, B. Z. (2023). Anthropogenic amplification of geomorphic processes on fluvial channel morphology, case study in Gilgel Abay river mouth; lake Tana Sub Basin, Ethiopia. *Heliyon*, *9*(4), e14390. https://doi.org/10.1016/j.heliyon.2023.e14390

Boothroyd, R. J., Williams, R. D., Barrett, B., Hoey, T. B., Tolentino, P. L. M., Perez, J. E., Guardian, E., David, C. P., & Yang, X. (2020). Detecting and quantifying morphological change in tropical rivers using Google Earth Engine and image analysis techniques. *River Flow 2020 - Proceedings of the 10th Conference on Fluvial Hydraulics*, *November*, 1013–1021. https://doi.org/10.1201/b22619-142

Cao, Z., Pender, G., & Meng, J. (2006). *Explicit Formulation of the Shields Diagram for Incipient*. *October*, 1097–1099.

Church, M. (2006). *Bed Material Transport and the Morphology of Alluvial River Channels*. 325–356. https://doi.org/10.1146/annurev.earth.33.092203.122721

Coleman, B. W. M. and S. E. (2000). *Bridge Scour*. Water Resources Publications, LLC.

Cooperative, N., Wagner, C. R., Mueller, D. S., Parola, A. C., Hagerty, D. J., Benedict, S. T., & Survey, U. S. G. (2006). *Scour at Contracted Bridges Prepared for : Submitted by : 83*(March).

Ettema, R., Asce, F., Constantinescu, G., Asce, M., Melville, B. W., & Asce, M. (2017). *Flow-Field Complexity and Design Estimation of Pier-Scour Depth : Sixty Years since Laursen and Toch*. *143*(9), 1–14. https://doi.org/10.1061/(ASCE)HY.1943-7900.0001330.

Farooq, R., & Ghumman, A. R. (2019). *Impact Assessment of Pier Shape and Modifications on*

Scouring around Bridge Pier. 14–20.

FHWA. (2009). *HEC 23 Volume 1 Bridge Scour and Stream Instability Countermeasures: Experience, Selection, and Design Guidance-Third Edition*. *1*(23).

FHWA. (2012). *Evaluating Scour at Bridges Fifth Edition*. *18*.

Foga, S., Scaramuzza, P. L., Guo, S., Zhu, Z., Dilley, R. D., Beckmann, T., Schmidt, G. L., Dwyer, J. L., Joseph Hughes, M., & Laue, B. (2017). Cloud detection algorithm comparison and validation for operational Landsat data products. *Remote Sensing of Environment*, *194*, 379–390. https://doi.org/10.1016/j.rse.2017.03.026

Ghazvinei, P. T., Darvishi, H. H., Ariffin, J., Jahromi, S. H. M., Aghamohammadi, N., & Amini, A. (2016). *MTP Validation Analysis of Scour Formulae in an Integral Abutment Bridge*. *00*(0000), 1–13. https://doi.org/10.1007/s12205-016-0181-6

Gorelick, N., Hancher, M., Dixon, M., Ilyushchenko, S., Thau, D., & Moore, R. (2017). Google Earth Engine: Planetary-scale geospatial analysis for everyone. *Remote Sensing of Environment*, *202*(2016), 18–27. https://doi.org/10.1016/j.rse.2017.06.031

Guillermo, L., Teixeira, L., & Ortega-s, M. (2013). *ESTIMATING FINAL SCOUR DEPTH UNDER CLEAR WATER FLOOD*. https://doi.org/10.1061/(ASCE)HY.1943-7900.0000804

Hong, S. H., & Abid, I. (2015). *Physical Model Study of Bridge Contraction Scour*. *00*(0000), 1–8. https://doi.org/10.1007/s12205-015-0417-x

Kirkil, G., Asce, M., Constantinescu, G., Asce, M., Ettema, R., & Asce, M. (2009). *Detached Eddy Simulation Investigation of Turbulence at a Circular Pier with Scour Hole*. *November*, 888–901.

Kumcu, S. Y., Kokpinar, M. A., & Gogus, M. (2014). *Scour Protection around Vertical-Wall Bridge Abutments with Collars*. *18*(12), 1884–1895. https://doi.org/10.1007/s12205-014-0245-4

Lade, A. D., Deshpande, V., Kumar, B., & Oliveto, G. (2019). On the morphodynamic alterations around bridge piers under the influence of instream mining. *Water (Switzerland)*, *11*(8). https://doi.org/10.3390/w11081676

Lagasse, P. F., Schall, J. D., & Richardson, E. V. (2001). Stream Stability at Highway Structures. *Hydraulic Engineering*, *20*, 260. http://isddc.dot.gov/OLPFiles/FHWA/010591.pdf

Li, J., Xia, J., Zhou, M., Deng, S., & Zhang, X. (2017). Variation in reach-scale thalweg-migration intensity in a braided reach of the lower Yellow River in 1986–2015. *Earth Surface Processes and Landforms*, *42*(13), 1952–1962. https://doi.org/10.1002/esp.4154

Li, J., Zhang, Y., & Ji, Q. (2020). Article lateral migration in a wandering reach of the middle yellow river in response to different boundary conditions. *Applied Sciences (Switzerland)*, *10*(15), 16–19. https://doi.org/10.3390/APP10155229

Liao, K. W., Muto, Y., & Lin, J. Y. (2018). Scour depth evaluation of a bridge with a complex pier foundation. *KSCE Journal of Civil Engineering*, *22*(7), 2241–2255. https://doi.org/10.1007/s12205-017-1769-1

Mandarino, A., Maerker, M., & Firpo, M. (2019). Channel planform changes along the Scrivia River floodplain reach in northwest Italy from 1878 to 2016. *Quaternary Research (United States)*, *91*(2), 548–569. https://doi.org/10.1017/qua.2018.67

Oliveto, G., & Marino, M. C. (2019). Morphological patterns at river contractions. *Water (Switzerland)*, *11*(8). https://doi.org/10.3390/w11081683

Omara, H., Elsayed, S. M., Abdeelaal, G. M., Abd-Elhamid, H. F., & Tawfik, A. (2019). Hydromorphological Numerical Model of the Local Scour Process Around Bridge Piers. *Arabian Journal for Science and Engineering*, *44*(5), 4183–4199. https://doi.org/10.1007/s13369-018-3359-z

Poggi, D., & Kudryavtseva, N. O. (2019). *Non-Intrusive Underwater Measurement of Local Scour Around a Bridge Pier*. https://doi.org/10.3390/w11102063

R.J.Grade. (2006). *River Morphology* (First). New Age International (P) Limited Publishers.

Schwenk, J., Khandelwal, A., Fratkin, M., Kumar, V., & Foufoula-Georgiou, E. (2017). High spatiotemporal resolution of river planform dynamics from landsat: The rivMAP toolbox and results from the Ucayali river. *Earth and Space Science*, *4*(2), 46–75. https://doi.org/10.1002/2016EA000196

Tabarestani, M. K., & Zarrati, A. R. (2016). *Local Scour Calculation Around Bridge Pier During Flood Event*. *00*(0000), 1–11. https://doi.org/10.1007/s12205-016-0986-3

USACE. (2016). *HEC-RAS River Analysis System*. www.hec.usace.army.mil

Wang, C., Yu, X., & Liang, F. (2017). monitoring and countermeasures. *Natural Hazards*. https://doi.org/10.1007/s11069-017-2842-2

Xiong, W., Cai, C. S., Kong, B., Tang, P., & Ye, J. (2017). *Identification of Bridge Scour Depth by Tracing Dynamic Behaviors of Superstructures*. *00*(0000), 1–12. https://doi.org/10.1007/s12205-017-1409-9

Zhou, K., Duan, J. G., & Bombardelli, F. A. (2020). Experimental and Theoretical Study of Local Scour around Three-Pier Group. *Journal of Hydraulic Engineering*, *146*(10), 1–10. https://doi.org/10.1061/(asce)hy.1943-7900.0001794

Zou, Z., Xiao, X., Dong, J., Qin, Y., Doughty, R. B., Menarguez, M. A., Zhang, G., & Wang, J. (2018). Divergent trends of open-surface water body area in the contiguous United States from 1984 to 2016. *Proceedings of the National Academy of Sciences of the United States of America*, *115*(15), 3810–3815. https://doi.org/10.1073/pnas.1719275115